THE UNIVERSITY OF QUEENSLAND

AUSTRALIA

Flow Instabilities at a Superfluid Boundary

Simeon Simjanovski
Honours Student

Under the supervision of
Dr. Tyler W. Neely

A thesis submitted to the University of Queensland
in partial fulfilment of the degree of Bachelor of Advanced Science with Honours
School of School of Mathematics and Physics
June 2021

Typeset in LaTeX 2_ε.

The work presented in this Thesis is, to the best of my knowledge and belief original, except as acknowledged in the text, and has not been submitted either in whole or in part, for a degree at this or any other university.

Simeon Simjanovski

Abstract

Superfluids and superfluid turbulence are complex phenomena resulting from macroscopic quantum effects. One application of Bose-Einstein condensation (BEC) research is the study of superfluid behaviour including turbulence and transitions to turbulence. Classically, these transitions are governed by instabilities and driven by viscosity. Recent computational work predicts the possibility for BEC superfluid systems to support an analogue to a specific class of classical instabilities, the Kelvin-Helmholtz (KH) instabilities. In a classical system, KH instabilities are characterised by a rolling up of the shear layer between two fluids, flowing at different velocities. In a BEC superfluid, the analogue for this interface is a line of quantised vortices, and the roll up of this interface manifesting as a clustering of these vortices over time. This thesis describes the realisation of the prior computational work into an experimental setting, where quasi-2D, single component BEC superfluids were used to investigate KH instabilities in a ring geometry.

Using a combination of atom cooling and trapping protocols, along with a digital micromirror device allowed for the trapping of a BEC superfluid into a ring geometry which could then be further subdivided into two concentric rings. These rings were then stirred to generate a persistent current and, through the removal of the barrier between the rings, a line of like-signed vortices was generated. This stirring process was optimised via the use of a Gaussian process regression machine learning algorithm in order to efficiently and consistently control vortex numbers at the superfluid boundary. Time-of-flight and Faraday imaging techniques were then used to acquire relevant data. The KH instability was subsequently observed in the superfluid system, indicated by a highly unstable shear layer which exhibited decay within the first 30 ms of free evolution. Via a vortex detection algorithm, the positions of the vortices could be found for each image taken and by taking multiple images over varying times, the dynamics of the vortices could be analysed statistically.

The cluster dynamics analysis was attempted for 20 and 30 vortices in a ring. These conditions were equivalent to using different starting shear velocities. The results in the both cases presented a decrease in the number of clusters present over time, while the average number of vortices per cluster increased which was indicative of progressive clustering characteristic decaying turbulence in classical 2D fluids. The time scales for this clustering effect were observed to be comparable to classical turbulence decay rates. In addition to observing the KH instability, the experiment demonstrated the generation of quantum turbulence emerging from the instability and was able to establish similarities in decaying turbulence between 2D quantum and classical liquids through flow field simulations derived from vortex positions.

To our knowledge, this project was the first instance of the experimental observation of KH instabilities in dilute gas BECs, and the first observation of the microscopic dynamics of the KH instability in superfluids.

Acknowledgements

This project was only possible thanks to a number of people through their input and assistance, whether directly or indirectly. I owe the success of the project and all I've learned throughout my honours year to each and every one of these people.

I would like to thank my supervisor, Dr. Tyler Neely, for all your guidance and support, both throughout this year and on all past projects I undertook under his mentorship. You were always eager to help me with all my problems and ensured that my work was performed to my absolute best ability. Under your guidance I have learned a deeper passion for experimental physics and without you, I would never have achieved anything close to this work. Your encouragement not only kept me going over this year but helped me grow as a scientist and build connections to many others to who I also owe thanks to. Thank you for the countless opportunities you presented to me and for developing my passion for research.

I would thank Mr. Guillaume Gauthier, Mr. Kwan Lee and Ms. Lauren McQueen for all their help throughout the project and their friendship. Whether it was through discussions or direct help on programming or feedback on my work you all helped me out greatly. Your assistance on the project is greatly appreciated, as were all your welcoming attitudes to make me feel like I am one of you.

Furthermore, I would also thank Professor Matthew Davis, Professor Halina Rubinsztein-Dunlop and Dr. Matthew Reeves for your encouragement and discussions. Your excitement about my work only further sparked my own excitement and motivated me to continue working hard. A special thanks to Dr. Matthew Reeves for your direct input into some of the most significant results of this work. There are countless others who I owe thanks to at the University of Queensland, both within the research group and beyond. Whether your contribution was a simple discussion or direct feedback, know that I greatly appreciate all your support.

Finally, I would like to thank those close to me who might not be physicists but their support was more than welcome. I thank my parents who supported me and have always pushed me to realise my goals. Without you I would never have reached this stage in my life. I also want to thank my two younger brothers, Dimitrij and Maksim, for both their welcome and unwelcome distractions throughout the year. Their cheerfulness and friendship was more than appreciated through this stressful year. Of course, I want to thank Jade for being by side throughout my entire undergraduate degree leading to this thesis and for your

unfaltering ability to keep me motivated.

Thank you to all my mentors, family and friends. Whether I've mentioned you explicitly above or not, I acknowledge everyone that helped make this thesis possible.

Contents

List of Figures

List of Tables

List of Abbreviations & Symbols

Abbreviation	Meaning
BEC	Bose-Einstein Condensate
SLM	Spatial Light Modulator
KH	Kelvin-Helmholtz
GPE	Gross-Pitaevkii Equation
RT	Rayleigh-Taylor
Rb	Rubidium
DMD	Digital Micromirror Device
NA	Numerical Aperture
TOF	Time-of-Flight
DBSCAN	Density-Based Spatial Clustering of Applications with Noise
GP	Gaussian Process
M-LOOP	Machine-Learning Online Optimization Package

Symbol	Meaning
Ψ	Macroscopic wavefunction
V	External potential
g	Interaction parameter
a	Scattering length
n	Atom number density
μ	Chemical potential
ϕ	Quantum phase/degeneracy parameter
$\mathbf{v}$	Fluid velocity field
$\mathbf{j}$	Probability current
ω	Vorticity
$\mathbb{R}$	Real number set
$\mathbb{R}^n$	Set of real n-vectors
$\mathbb{R}_+$	Non-negative real number set
$\mathbb{Z}$	Integer number set
$\mathbb{N}$	Natural Numbers
Γ	Circulation
Θ	Heaviside step function
ξ	Healing length
ε	DBSCAN radius

1 Introduction

Superfluids differ greatly from their classical fluid counterparts in properties and behaviour, making them an intriguing phenomenon to study. Superfluid flow is characterised via a lack of viscosity emerging for a material system beyond a phase transition as a result of cooling below a critical temperature [5, 12]. The lack of viscosity means that a superfluid shows very different behaviour from classical fluidity, where viscosity greatly influences the properties of a system [12]. Yet despite these differences, there exists similarity between superfluid and classical fluid behaviour in certain situations. It is in this region of overlap that one may study complex classical-like behaviour in superfluid systems such as turbulence [5].

There is considerable motivation for undertaking such an investigation. Namely, stronger connections between superfluids and their classical counterparts can be formed. It becomes possible to derive analogs between the quantum and classical turbulent phenomena through which the mechanisms by which superfluid turbulence arises can be understood. The development of understanding superfluid turbulence is important since the lack of viscosity in a superfluid introduces the question of how superfluid systems undergo transitions to turbulence. Classically, transitions to turbulence are driven by viscosity and thus superfluid turbulence must be driven by alternative processes [5, 12]. In studying these superfluid processes, the analog between superfluidity and classical fluidity may be further developed and by extension the understanding of classical turbulence may be improved. Indeed, there is growing evidence and support for the idea that larger scale superfluid turbulence is similar to classical turbulence [13]. In order to truly develop and understand these aforementioned connections, rigorous experimental work must be employed on superfluid transitions to turbulence.

Bose-Einstein condensate (BEC) research has already begun investigating superfluidity. BEC superfluid systems themselves offer a high level of versatility and control over experimental

parameters, such as atom density and atom interaction strength which are vital for investigations into superfluidity [5, 7, 12, 14–16]. Additionally, recently developed methods such as spatial light modulators (SLMs) allow for almost arbitrary manipulation of the BEC superfluid shape and flow velocity [5, 7, 14–16] allowing for a vast range of flow configurations to be investigated experimentally. This high level of experimental control means that BEC superfluid experiments are highly replicable and offer the ideal medium for superfluid turbulence studies [5, 7, 14–16].

Some phenomena of interest related to superfluid turbulence are the dynamical phenomena driving transitions to turbulence. The simplest of all such mechanisms is that of the Kelvin-Helmholtz (KH) instability which describes a "rolling-up" effect of the interface between two parallel flowing streams [5]. Recent computational work by Baggaley & Parker [5] has predicted an analog of KH instabilities in 2D single component[1] BEC superfluid systems where the interface between two streams was no longer a continuum but a line of quantised vortices. Their work showed that this line of vortices was unstable and would cluster at varying length-scales to mirror the rolling up of a classical boundary [5]. Baggaley & Parker also suggested the possibility for expansion into experimental work by studying the KH instability in a ring geometry. This project adapted the prior work by Baggaley & Parker into the experimental investigation of KH instabilities in a quasi-2D, ring-trapped, single component BEC superfluid. The motivation was to attempt the experimental observation of KH instabilities in a pure BEC superfluid such that experimentally derived results could be used to draw connections between classical and superfluid turbulence. In the experiment, KH instabilities were observed as predicted by Baggaley & Parker. The dynamics of the resulting vortices were analysed to better understand superfluid transitions to turbulence. The outcomes of the project are presented in this paper.

The structure of this thesis is such that both experts and non-experts may appreciate the work and results. A detailed background into BECs and superfluidity is thus presented in Section 2 to lay the groundwork for understanding and discussing BEC superfluid dynamics. There is additional background on instabilities in Section 3, where the major focus is on KH instabilities. Following the background, there is an explanation of the experimental techniques used in this project in Section 4. Finally, the results of the project are presented in Section 5, where a detailed discussion on the accuracy, significance and outlook for the major results is also given.

[1] "Single-component" referring to the use of the same species and states of atoms/bosons as opposed to "multi-component" where multiple species of different atoms/bosons or different states of the same atoms/-bosons are used [7].

2
Bose-Einstein Condensates

This chapter focuses on the relevant background required to understand BECs, as well as their connection to superfluids. A formal definition of BECs is given in the context of Bose gases. The approximation of the many-body wavefunction of a BEC system as a macroscopic wavefunction is described and the Gross-Pitaevskii equation (GPE) which defines the evolution of the macroscopic wavefunction for a BEC system is also considered. There is then an extension of the theory to superfluidity via the Madelung transformation of the macroscopic wavefunction. This transformation essentially allows the previously discussed theory to be viewed in a format more readily compatible with familiar fluid dynamics theory. In making this connection to BEC superfluids, some similar behaviour to classical fluid dynamics will be observed, as well as some behaviour unique to superfluids. As a result of all prior the discussion, it will be shown that BEC superfluids can support poles of quantised circulation which are referred to as vortices. Understanding the formation and dynamics of these vortices is critical for understanding their role in observing and measuring KH instabilities.

2.1 Formal defintion of BECs

Formally, one defines a BEC as a Bose gas[1] which has undergone a phase transition under a critical temperature [7, 18]. The resulting phase is characterised by the occupation of the macroscopic ground state of the system by all the bosons in the ensemble, at absolute zero temperature [7, 18, 19]. In physically realisable systems relevant to BEC experiments, not all the bosons achieve this condensation but a large proportion of the ensemble do satisfy the condition [19]. Theoretically, the dynamics of the resulting condensate is completely solvable via the many-body Schroedinger equation, via a many-body wavefunction [7, 19]. The many-body wavefunction completely captures the required information about

[1] Collection of particles, obeying Bose-Einstein statistics [7, 17]

the BEC system via its probability density [7, 13, 19]. Unfortunately, making use of this many-body theory is impractical despite its relative conceptual simplicity. Computationally, use of many-body wavefunctions with experimentally consistent atom numbers is expensive, and generally many-body theory is mathematically complicated to a degree that would not be useful in generating predictions about these BEC systems [7, 13]. Instead, a pragmatic approach is required, where the many-body problem is reduced to a single-body problem via approximation.

The mechanics of the ensemble of bosons can be approximated in a semi-classical environment via the macroscopic wavefunction, $\Psi(\mathbf{r}, t)$, where $\mathbf{r}$ is an arbitrary spatial position vector and t is time. This macroscopic wavefunction describes the local boson number density in a BEC [19]. At this point, to avoid confusion, there will be no longer distinction between bosons and atoms due to the fact that in experiment the atoms used to create the BEC are bosons (^{87}Rb atoms). Thus, the probability density of the macroscopic wavefunction is said to be the local atom number density; $|\Psi(\mathbf{r}, t)|^2 = n(\mathbf{r}, t)$.

Strictly speaking, $\Psi(\mathbf{r}, t)$ is a mean-field approximation to the many-body wavefunction that accurately describes the system given some approximations, effectively simplifying the BEC wavefunction to an N-particle single wavefunction [19]. The macroscopic approximation is valid given that the majority of the atoms are in the ground state (a condition already satisfied by the definition of BECs) and given that the interaction between atoms is weak [7, 19].

Yet, as an approximation the macroscopic wavefunction will still fail to account for features present in the full many-body theory. For example, $\Psi(\mathbf{r}, t)$ cannot describe the dynamics of atoms which fail to condense into the ground state [7]. Even some quantum effects such as tunnelling do not manifest under $\Psi(\mathbf{r}, t)$ since the macroscopic approximation is semi-classical [7]. Fortunately, the features relevant to the work presented here are still present in $\Psi(\mathbf{r}, t)$; namely quantum vortices which are discussed in Section 2.3. To study these relevant features, the dynamics of the system must be considered. It can be shown that $\Psi(\mathbf{r}, t)$ evolves according to the Gross-Pitaevskii equation [7, 13, 19]:

$$i\hbar\frac{\partial\Psi(\mathbf{r},t)}{\partial t} = \left[-\frac{\hbar^2}{2m}\nabla^2_{\mathbf{r}} + V(\mathbf{r},t) + g\left|\Psi(\mathbf{r},t)\right|^2\right]\Psi(\mathbf{r},t), \tag{2.1}$$

where m is the mass of the atoms in the system[2], $\nabla^2_{\mathbf{r}}$ is the Laplacian (yet to be defined in a specific coordinate system), $V(\mathbf{r}, t)$ is the external potential acting on the system and g is the interaction strength parameter which introduces non-linearity to the dynamics of the system. Generally the interaction parameter is defined in terms of the mass m and scattering length[3] a by [20]:

$$g = \frac{4\pi\hbar^2 a}{m}.$$

[2]More generally there would be a summation over varying masses in the kinetic energy term in Eq. (2.1) [19]. Here only single-component BECs are considered and so this mass is the same for all constituent particles and the summation is omitted.

[3]Alternatively a is defined to be the scattering cross-section for a process interacting via spherical waves[7].

With this interaction parameter, it is possible to quantify whether interactions are considered weak in a BEC via the relation between scattering length and atom number density $n = |\Psi|^2$ as defined previously [20]:

$$na^3 \ll 1. \tag{2.2}$$

In the context of the typical experimental BEC, the scattering length in on the order of nanometers, so $a^3 \sim 10^{-26}$ cubic centimeters, while atom number density tends to be on the order of at most 10^{15} atoms per cubic centimeter [20] and so the condition requiring weak interaction is certainly satisfied. This means that using the macroscopic wavefunction to theoretically predict experimental outcomes is valid.

If $g = 0$, i.e. the non-interacting case, the GPE reduces to the familiar Schroedinger equation with the bulk of the atoms behaving as a single particle or matter wave [7]. On the other hand, if $g > 0$ the interactions are repulsive whereas for $g < 0$ the interactions are attractive [7, 13, 19]. This project operates exclusively in the regime of repulsive interactions. From Eq. (2.1) it is clear that weak interactions between the atoms in a BEC result in non-linear effects manifesting in the system dynamics [7].

These dynamics are generally studied via imaginary time-evolution, making the replacement $t \to -it$ in $\Psi(\mathbf{r}, t)$ before considering evolution [21]. Imaginary time-evolution is useful in quantum systems to find ground state wavefunctions [21]. This is possible via the application of a ground state ansatz which is then evolved in imaginary time to find the ground state wavefunction [7, 21]. A common ansatz choice is a wavefunction found under the Thomas-Fermi approximation; where in the ground state the kinetic energy of the system is said to be negligible relative to the interaction energy [7, 22]. This approximation is most useful if one applies separation of variables to Eq. (2.1) in order to acquire the time-independent GPE. Specifically, separation of variables proposes solutions of the form $\Psi(\mathbf{r}, t) = e^{-\frac{i\mu t}{\hbar}}\psi(\mathbf{r})$ where μ is the chemical potential[4] [7, 19]. Additionally assuming a time-independent potential $V(\mathbf{r}, t) \to V(\mathbf{r})$, it is possible to write the time-independent GPE as follows [7, 19]:

$$\mu\psi(\mathbf{r}) = \left[-\frac{\hbar^2}{2m}\nabla^2_{\mathbf{r}} + V(\mathbf{r}) + g|\psi(\mathbf{r})|^2\right]\psi(\mathbf{r}). \tag{2.3}$$

Under the Thomas-Fermi approximation, the first term (kinetic energy) in the brackets of Eq. (2.2) can be neglected, then solving for $|\psi(\mathbf{r})|^2$ yields [7, 19, 22]:

$$\mu = V(r) + g|\psi(\mathbf{r})|^2, \tag{2.4}$$

$$|\psi(\mathbf{r})|^2 = \frac{\mu - V(\mathbf{r})}{g}. \tag{2.5}$$

Of course, this probability density of the spatial macroscopic wavefunction is only sensible given it permits only positive values (between 0 and 1 assuming correct normalisation), and

[4]Defined in a familiar way in statistical mechanics as the rate of change of system energy with respect to atom/particle number, $\frac{\partial E}{\partial N}$ [7]

thus the Thomas-Fermi approximation can be reduced to the condition [7, 19]:

$$|\psi(\mathbf{r})|^2 = \begin{cases} \frac{\mu - V(\mathbf{r})}{g}, & \text{for } \mu \geq V(\mathbf{r}) \\ 0, & \text{otherwise.} \end{cases} \tag{2.6}$$

Eq. (2.6) illustrates the ground state dependence on the external potential but also illustrates implicitly how the atom number density of the BEC system will generally follow the potential [7]. This last observation is clear when one recalls that the probability density of the macroscopic wavefunction describes the local atom number density. Thus, the shape of the BEC can be altered by dynamically varying the ground state via the external potential, which is exclusively used in the experiment (see Section 4.2) [23]. With the Thomas-Fermi approximation and its implications understood, the fundamental background of BEC theory relevant to the work of this project is concluded. However there is still a need to connect this presented theory to superfluidity.

2.2 Connecting BECs to Superfluids

The GPE itself was first derived in the context of superfluidity (specifically superfluid Helium) [7, 18] and thus extension of BEC theory to BEC superfluidity is almost trivial. Indeed, the GPE may be rewritten in the so-called "hydrodynamic form" [7, 19] via a transformation of the macroscopic wavefunction. The specific transformation used is referred to as the Madelung transformation and its action on $\Psi(\mathbf{r}, t)$ is to rewrite the wavefunction in polar form depending only on local atom number density $n(\mathbf{r}, t)$ and local quantum phase $\phi(\mathbf{r}, t)$:

$$\Psi(\mathbf{r}, t) \to \sqrt{n(\mathbf{r}, t)} e^{i\phi(\mathbf{r}, t)}. \tag{2.7}$$

An alternative description of the Madelung transformation is that, in the mean-field, it equates the macroscopic wavefunction to the complex order parameter which phenomenologically describes Bose-Einstein condensation as a phase transition under Landau theory [20, 24]. Under this transformation it is immediately clear that the probability density of the macroscopic wavefunction gives the local atom number density [7]. The phase of a complex order parameter in Landau theory is also referred to as the degeneracy parameter [24]. This is due to the fact that thermodynamic potentials[5] do not depend on the phase and so it is possible for a superfluid to have varying degeneracy parameters while having the same thermodynamic potential (hence *degeneracy*) [24]. Therefore, one usually defines the phase of the macroscopic wavefunction/order parameter modulo 2π so that degeneracy in a thermodynamic setting is lifted and the single-valuedness of the wavefunction is preserved [20, 24]. In the case of Eq. (2.7) however, single-valuedness can be preserved via restricting the change in phase around any closed loop to be an integer multiple of 2π. Overall, via Landau theory and the Madelung transformation, the connection between BECs and superfluidity is made more obvious.

[5]There are 4 quantities referred to as the thermodynamic potentials; internal energy, Helmholtz free energy, Gibbs free energy and enthalpy [25]

By substituting the Madelung transformation into the GPE, Eq. (2.1), one may consider the resulting real and imaginary components separately. The resulting equations [7, 20]:

$$\frac{\partial n(\mathbf{r},t)}{\partial t} = -\nabla\cdot\left(n(\mathbf{r},t)\frac{\hbar}{m}\nabla\phi(\mathbf{r},t)\right), \tag{2.8}$$

$$\hbar\frac{\partial\phi(\mathbf{r},t)}{\partial t} = -\left(\frac{1}{2}m\big[\hbar\nabla\phi(\mathbf{r},t)\big]^2 + V(\mathbf{r},t) + gn(\mathbf{r},t) - \frac{\hbar^2}{2m\sqrt{n(\mathbf{r},t)}}\nabla_{\mathbf{r}}^2\left(\sqrt{n(\mathbf{r},t)}\right)\right), \tag{2.9}$$

resemble the classical hydrodynamics equations, Eq. (2.8) arises from the imaginary component of the GPE and is the familiar equation of mass continuity which ensures local mass conservation in the fluid (i.e. compressibility) [26, 27]. Eq. (2.9) arises from the real component of the GPE and is analogous to the Bernoulli equation or energy conservation for an inviscid fluid [7, 20, 27]. Thus, there are already indications that a BEC is a superfluid system inherently, since the BEC hydrodynamics equations lack viscosity drag terms. Below, proof that a BEC is a superfluid system will be made mathematically rigorous via computation of the vorticity of a BEC.

Eqns. (2.8) & (2.9) also give merit to the concept of overlap between classical and superfluid dynamics by the emergence of almost identical hydrodynamics equations [7]. Of course, as expected there are some discrepancies. One example is the final term in the brackets of Eq. (2.9). This term is referred to as the quantum pressure term and has no classical analog [7, 27]. The quantum pressure term arises from compressibility of quantum fluids but it is only relevant at the edges of the BEC and becomes negligible for large condensate fractions [7, 20, 26, 27]. Ignoring the dissimilar factor of quantum pressure, a connection from these BEC hydrodynamics equations to classical hydrodynamics is especially clear if one defines a phase-velocity relationship as [7]:

$$\mathbf{v}(\mathbf{r},t) = \frac{\hbar}{m}\nabla\phi(\mathbf{r},t), \tag{2.10}$$

which can be derived in a variety of ways. The simplest is via arguing by comparison. Specifically, comparing Eq. (2.8) and the classical mass continuity equation, it is immediately obvious that a substitution of the form of Eq. (2.10) would exactly equate the two cases [26, 27]. Alternatively, given the macroscopic wavefunction in the polar form of the Madelung transformation, it is possible to evaluate the general formula for a wavefunction probability current $= n(\mathbf{r},t)\mathbf{v}(\mathbf{r},t)$ [20]:

$$\mathbf{j}(\mathbf{r},t) = i\frac{\hbar}{2m}\left[\Psi(\mathbf{r},t)\nabla\Psi^*(\mathbf{r},t) - \Psi^*(\mathbf{r},t)\nabla\Psi(\mathbf{r},t)\right]. \tag{2.11}$$

Then substitution of Eq. (2.7) into Eq. (2.11) gives Eq. (2.10). However one chooses to derive the phase-velocity relationship. With some minor algebra and substitution one acquires [20]:

$$\frac{\partial n(\mathbf{r},t)}{\partial t} = -\nabla\cdot\left(n(\mathbf{r},t)\mathbf{v}(\mathbf{r},t)\right), \tag{2.12}$$

$$m\frac{\partial\mathbf{v}(\mathbf{r},t)}{\partial t} = -\nabla\left(\frac{1}{2}m\big[\mathbf{v}(\mathbf{r},t)\big]^2 + V(\mathbf{r},t) + gn(\mathbf{r},t) - \frac{\hbar^2}{2m\sqrt{n(\mathbf{r},t)}}\nabla_{\mathbf{r}}^2\left(\sqrt{n(\mathbf{r},t)}\right)\right), \tag{2.13}$$

thereby connecting Eq. (2.12) to mass continuity and Eq. (2.13) to the Bernoulli equation. Continuing the analogy to classical fluids, one might consider vorticity $\omega = \nabla \times \mathbf{v}$ of a BEC superfluid. In fact, it is immediately obvious that by the phase-velocity relationship, vorticity must vanish everywhere due to vector calculus identities [7]:

$$\omega(\mathbf{r}, t) = \nabla \times \mathbf{v}(\mathbf{r}, t) = \frac{\hbar}{m} \nabla \times \nabla \phi(\mathbf{r}, t) = 0, \qquad \forall (\mathbf{r}, t) \in \mathbb{R}^3 \times \mathbb{R}_+. \tag{2.14}$$

Thus, the BEC must behave as an inviscid, irrotational fluid, or superfluid, by definition [20].

The discussion has currently presented BEC hydrodynamics equations which lead to the understanding of a BEC system as a superfluid under the Madelung transformation. Through simple arguments and algebra it was possible to introduce a connection between classical fluidity and BEC superfluidity while simultaneously showing some differences between the two. Overall, it is clear that using the Madelung transformation is sufficient to show that BEC systems exhibit superfluidity with behaviours and dynamics dictated by a set of quantum hydrodynamics equations which have strong classical analogs. This makes the quantum hydrodynamics equations interesting objects to consider, but for the investigation undertaken within the project, it is actually the phase-velocity relationship in Eq. (2.10) and the vorticity of the BEC superfluid in Eq. (2.14) that are more relevant. Using these relations, it is possible to derive the conditions for vortices to be supported in the BEC superfluid.

2.3 Quantum Vortices

It is important to understand vortices in a BEC superfluid due to their close relation to KH instabilities as is discussed in Section 3. The fact that BEC superfluids are irrotational leads to the definition of these vortices. Specifically, it is known that the curl of the gradient of a scalar field must be zero as imposed in Eq. (2.14) [7]. Thus, by analogy to a classical fluid, the BEC superfluid must be irrotational. In classical fluids, it is common to consider irrotational systems for simplicity. Due to restrictions placed on quantum systems such as the single-valuedness of the wavefunction, irrotation of the velocity field results in some interesting implications (as will become clear below). Firstly, irrotation suggests that the circulation around any simply-connected region[6] vanishes, which is easily seen by computing circulation Γ_{SC} around an arbitrary closed curve $\mathcal{C}$ encompassing a simple-connected $\mathcal{S}$ region via Stokes theorem:

$$\Gamma_{\text{SC}} = \oint_{\mathcal{C}} \mathbf{v}(\mathbf{r}, t) \cdot \mathrm{d}\mathbf{l} = \int_{\mathcal{S}} \nabla \times \mathbf{v}(\mathbf{r}, t) \cdot \mathrm{d}\mathbf{S} = \int_{\mathcal{S}} \omega(\mathbf{r}, t) \cdot \mathrm{d}\mathbf{S} = 0.$$

Yet there is a reason that the discussion has been restricted to simply-connected regions so far; Eq. (2.10) is only valid if $\nabla \phi(\mathbf{r}, t)$ is well defined, such as in simply-connected regions where there are no discontinuities in phase or atom number density [27]. At points where

[6]Simply-connected is informally defined as a domain where any closed curve within can be shrunk continuously to a single point within the original domain [28]. What this really means is that the space does not contain any "holes".

the wavefunction vanishes, i.e. no atom density points, the phase is not well-defined and so it is possible to support circulation in a BEC if the region bound by the circulation contour contains a pole. Computing circulation Γ around such a multiple-connected region $\mathcal{D}$ using a contour $\mathcal{R}$ yields [7, 20, 27]:

$$\Gamma = \oint_{\mathcal{R}} \mathbf{v}(\mathbf{r},t)\cdot \mathrm{d}\mathbf{l} = \frac{\hbar}{m}\oint_{\mathcal{R}} \nabla\phi(\mathbf{r},t)\cdot \mathrm{d}\mathbf{l} = \frac{\hbar}{m}\Delta\phi(\mathbf{r},t)\Big|_{\mathcal{R}}, \tag{2.15}$$

where the last equality is made via the fundamantal theorem of calculus for line integrals and $\Delta\phi(\mathbf{r},t)|_{\mathcal{R}}$ is the change of phase around the closed contour $\mathcal{R}$. Recalling however, that single-valuedness is imposed on the macroscopic wavefunction, it is required that $\Delta\phi(\mathbf{r},t)|_{\mathcal{R}} = 2\pi j$ for some integer j [7, 27]. Thus, the circulation around any region containing a pole in the macroscopic wavefunction of the BEC superfluid is quantised to:

$$\Gamma = \frac{2\pi\hbar}{m} j, \qquad j \in \mathbb{Z}. \tag{2.16}$$

Thus, in a BEC superfluid there can persist poles in the atom number density profile with quantised circulation. These poles are defined as quantum vortices [7, 20, 27]. The number j in the quantised vortex circulation is referred to as the winding number or charge of the vortex [7]. Using Eq. (2.15) and (2.16) together, allows for one to work backwards in order to find the vorticity of a quantum vortex [7]:

$$\frac{2\pi\hbar}{m} j = \oint_{\mathcal{R}} \mathbf{v}(\mathbf{r},t)\cdot \mathrm{d}\mathbf{l} = \int_{\mathcal{D}} \nabla\times\mathbf{v}(\mathbf{r},t)\cdot \mathrm{d}\mathbf{S} = \int_{\mathcal{D}} \omega(\mathbf{r},t)\cdot \mathrm{d}\mathbf{S}. \tag{2.17}$$

For sake of generality it can be assumed that the pole in region $\mathcal{D}$ is located at position $\mathbf{R}$ at time T. Restricting the BEC superfluid to 2D would simplify solving for the vorticity since the curl of the velocity field must be oriented perpendicular to the 2D plane of the system, say along axis $\hat{z}$ [7, 27]. This 2D assumption is quite valid and relevant since in the experiment the BEC superfluid is confined in a quasi-2D ring geometry as described in Section 4. Nonetheless, under these conditions two delta-functions for position and time will suffice to solve the integral in the desired manner. This is because the only point that can have non-zero vorticity is at the vortex core/pole where $\nabla\phi(\mathbf{r},t)$ is ill-defined. So the resulting vorticity profile is localised to the core of the vortex by [7]:

$$\omega(\mathbf{r},t) = \frac{2\pi\hbar}{m} j\delta^{(3)}(\mathbf{r}-\mathbf{R})\delta(t-T). \tag{2.18}$$

Such a system of vortices are referred to as point-vortices as all the charge and vorticity is localised to their cores [7, 29]. In this case, vortices in a BEC superfluid should have dynamics governed by the point vortex model [7, 29, 30] where the velocity of some vortex labelled l is $\mathbf{v}_l$ and is related to the gradient in the phase induced at its position $\mathbf{r}_l$ by all other vortices in the system [7]:

$$\mathbf{v}_l = \frac{\hbar}{m}\sum_{k\neq l} \nabla\phi_k\big|_{\mathbf{r}=\mathbf{r}_l}. \tag{2.19}$$

The fact that the dynamics of any vortex in a BEC superfluid is influenced by velocity flow induced by all other vortices can lead to highly complex behaviour [7]. Such complex vortex dynamics is precisely why vortices are closely related to superfluid turbulence, and by extension superfluid instabilities as is discussed in Section 3.

3 Instabilities in Fluid Systems

This chapter discusses fluid instabilities in both a classical and superfluid setting. The goal is to motivate the study of KH instabilities in this project while fostering enough understanding about the phenomema to appreciate their importance in a more general sense. First there is a discussion on the classical definition of an instability with some brief examples given. The focus here however is on the classical KH instability which serves as the analog for the transitions to turbulence in the BEC superfluids investigated experimentally. In discussing instabilities in this classical setting, their importance in fields such as engineering, meteorology and even astrophysics is introduced. Following this overview, an extension of the classical KH instability to 2D single-component BEC superfluids is discussed. Specifically, experimental investigation of the superfluid KH instability is motivated through prior computational work by Baggaley & Parker [5]. This work predicted a transition to turbulence in BEC superfluids analogous to the classical KH instability. Finally, extension of the work by Baggaley & Parker into an experimental BEC system is also discussed abstractly, leading into Section 4 where experimental implementation is discussed in detail.

3.1 Understanding Classical Instabilities

Instabilities in classical viscous fluids govern transitions from laminar to turbulent flow [3, 5, 31]. Turbulence is a non-linear phenomenon, typically arising from a perturbation in a fluid system [32]. Under such a perturbation one observes the emergence of some quasi-periodic structure or pattern in the fluid system, which over time cascades into a more chaotic and larger structure eventually transitioning the fluid flow towards fully developed turbulence [1, 32]. The mechanism by which the structure forms and evolves under a perturbation is defined as the instability since it dictates how turbulence will emerge from seemingly stable laminar flow [32]. It is possible to classify instabilities via the phenomena that drive them, typically flow or buoyancy [32, 33]. This can be seen via a simple argument starting with a

2D classical, stratified[1] fluid. Under a perturbed Navier-Stokes equation it can be seen that the vorticity of the fluid will actually vary over time (indicating an instability) [32]. The exact evolution of vorticity ω is given according to the density of the fluid ρ, the pressure in the system P, the initial stable fluid velocity $\mathbf{U} = (U_x, U_y, U_z)$ and the perturbation characterised by a velocity $\mathbf{u} = (u_x, u_y, u_z)$ by the material derivative [32]:

$$\frac{\mathrm{D}\omega}{\mathrm{D}t} = \frac{1}{\rho^2}\nabla(\rho^2) \times \nabla P + \frac{\partial U_x}{\partial y}\frac{\partial u_x}{\partial x}. \tag{3.1}$$

The first term in Eq. (3.1) highlights that both a density or pressure gradient in a system can result in an instability. Such instabilities are buoyancy driven [32]. Alternatively, an instability can be introduced via a velocity gradient and this is referred to as a flow-driven instability [32]. In both cases however, typically one can relate these driving mechanisms to viscosity in classical systems [1, 5]. That is to say, while the introduction of an instability might not directly require viscosity, it is not the presence of an instability that drives transitions to turbulence. The true general drive towards turbulence is the cascading effect of the emergent structure arising from the vorticity introduced via an instability [5, 32].

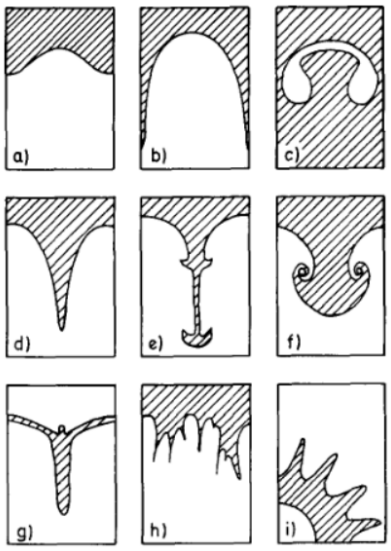

FIGURE 3.1: Schematics of different 2D flow patterns emerging under an RT instability where the system is accelerated vertically upward (a-h) or radially inward (i). Shaded regions indicate a higher density (heavy) fluid and unshaded regions represent a lower density (light) fluid. Different patterns result from different initial equilibria used. (a) Initial horizontal equilibrium between fluids. (b) Same initial horizontal equilibrium with larger upward acceleration. (c) Initial spherical equilibrium with lighter fluid in the sphere. (d-g) Falling heavy fluid (varying upward acceleration). (h) Complex flow due to mixing between fluids. (i) Spherical shell of higher density accelerated inwards radially (origin bottom left of diagram). Figure taken from Ref. [1].

[1]Stratified fluids are fluids with some density change along an a spatial axis, typically taken to be the vertical direction [34]. This density variation can be a gradient or discrete change [32, 34]. Note that constant density configurations can be considered as a special case of stratified fluids where the density change is zero. In this case, single-component systems are stratified.

This cascade is viscosity driven in classical fluids and therefore, instability induced transitions to turbulence in classical fluids require viscosity [1, 5, 32, 33].

Eq. (3.1) is derived in the context of general 3D classical fluids, but here the subsequent discussion is limited to 2D systems exclusively. These systems decrease the complexity of turbulent phenomena and are directly related to the work presented here. While 2D Buoyancy-driven instabilties are not investigated in this project, they are necessary for consideration in systems with multiple fluid densities. Possible extensions of the work described here could implement multi-component superfluids with the aim of investigating buoyancy-driven instabilities. For completeness, they are worth a brief discussion. Most buoyancy-driven instabilities can be understood from the Rayleigh-Taylor (RT) instability. This instability is classified by the motion of a denisty varying fluids via a pressure gradient [1, 32]. This occurs naturally in the atmosphere of the Earth since there are a variety of different density gases being accelerated through a gravitational potential [32], making the study of Rayleigh-Taylor instabilities vital in the fields of meteorology and aviation where an emergence of turbulence shapes the conditions for weather [12, 32]. While turbulent behaviour is generally chaotic and difficult to describe it is possible to observe some common features in RT instabilities during the transition to turbulence. Examples are shown in Fig. 3.1 as schematics of typical fluid profiles in 2D systems.

Some common features of RT instabilities include sinusoidal interface profiles between two fluids and "needles" forming due to the motion of a more dense fluid through another [1]. Additionally, features such as Fig. 3.1 (e-f) emerge due to the presence of a velocity gradient/shear and not purely from buoyancy effects [1]. Such profiles are expected in regimes where the buoyancy terms of Eq. (3.1) are larger than the flow terms but not so large as to dominate the instability [1].

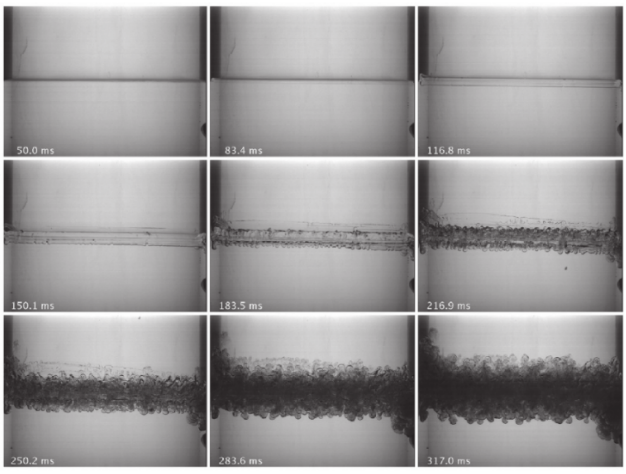

Figure 3.2: Experimental observation of turbulence induced via a RT instability between a light isopropyl alcohol fluid-flim and a heavy lithium polytungstate salt aqueous solution film. Acceleration is driven downwards stronger than gravity to accentuate features typical in RT induced turbulence in the atmosphere. Results taken from Ref. [2].

The transition to turbulence via RT instabilities have been observed experimentally in various work such as that of Roberts [2] where two fluids are held in equilibrium with a horizontal interface and small perturbations are induced via imperfect acceleration downwards greater than gravity [32]. Doing so allows for one to observe atmospheric-like turbulence phenomena only accentuated as shown in Fig. 3.2 [2]. In the figure there is a very clear emergence of both the sinusoidal and needle profiles at varying length-scales. When combined with the viscosity of the fluids resulted in a gradual transition into turbulence via the aforementioned cascading effect of the structure. Such processes occur constantly within a variety of fluid systems, particularly in fields related to atmospheric conditions, which highlights the importance of instabilities in general.

The investigation in this project is the KH instability, which falls under 2D flow-driven instabilities. Similar to how RT instabilities fundamentally explain buoyancy-driven instabilities, the KH instability is the most fundamental velocity shear-driven instability as it concerns itself only with describing the behaviour of a velocity shear layer between two parallel flowing fluid streams [3, 5]. As such a fundamental instability, the prevalence of KH instabilities in physical systems exceeds even that of the buoyancy-driven instabilities [32]. It possible to observe the dramatic effects of KH instabilities in atmospheric events [32]. However, they are also important wherever fluid flow is present. This makes KH instabilities fundamentally important not only to meteorology and aviation, but to general engineering and even astrophysics [12]. This can be made more obvious by visualising the emergence of a KH instability in a velocity shear layer via the transition to turbulence of the fluid such as in Fig. 3.3. Here there is a "rolling up" effect of the interface over time due to the difference in velocity between the two fluids. Due to viscosity, this rolling up effect occurs over a range of length scales, resulting from perturbations to the shear layer, which form coherent, large-scale structures in 2D after long times (see Section 3.3) [4, 5]. This expo-

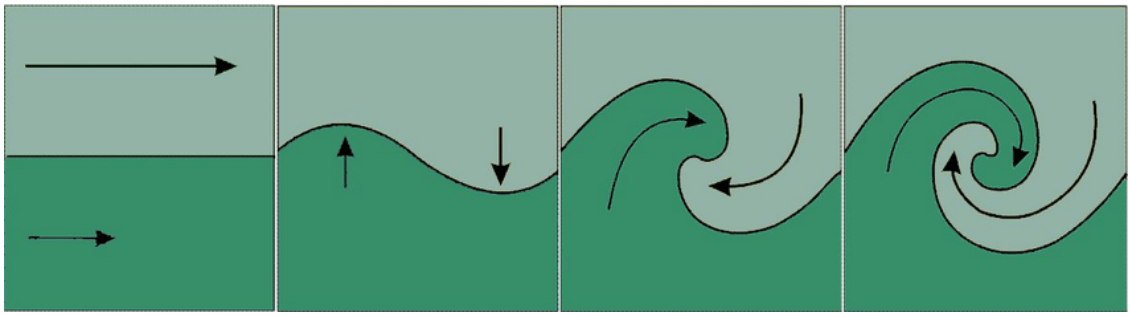

FIGURE 3.3: Illustration of a transition to turbulence driven bt a KH instability seeding perturbations in the shear layer of a 2D classical system. Here two arbitrary classical fluid streams are indicated by different shading. The interface/boundary is indicated by the horizontal black line separating the two streams. The arrows in each stream represent fluid velocity, which the lengths of the lines indicating the magnitude. Each panel illustrates how the boundary evolves over time, where time increases from left to right. Due to the relative difference in velocity between the streams, drag effects are incurred between the streams resulting in deformation of the interface/boundary in a "rolling up" motion. Figure taken from Ref. [3].

nential perturbation growth at the interface often leads to turbulence via destruction of the laminar flow in both fluids [5]. Of course, transitions to turbulence in this manner require large enough perturbations such that they are not suppressed by energy dissipation [4, 32].

The perturbations in the system are seeded into the interface via the KH instability [32]. KH instabilities can actually be simplified further into their most fundamental case; the velocity shear between two streams of the same fluid [4, 5, 33]. In this case, all relative differences in flow velocities between the streams will result in KH instability induced transitions to turbulence [5]. Due to this, it becomes clear exactly how critical studying KH instabilities becomes in understanding classical turbulence since in many regards they are the most fundamental instability inducing transitions to turbulence. This is the reason for an abundance of literature focusing on simulating and understanding KH instability induced transitions to turbulence, which is becoming a well researched phenomenon and is readily visualised computationally, such as in Fig. 3.4. These simulations are performed by computational solving coupled partial-differential equations derived from the Euler equations for fluids [4]. Viscosity is present in these simulations as well meaning that it is possible to

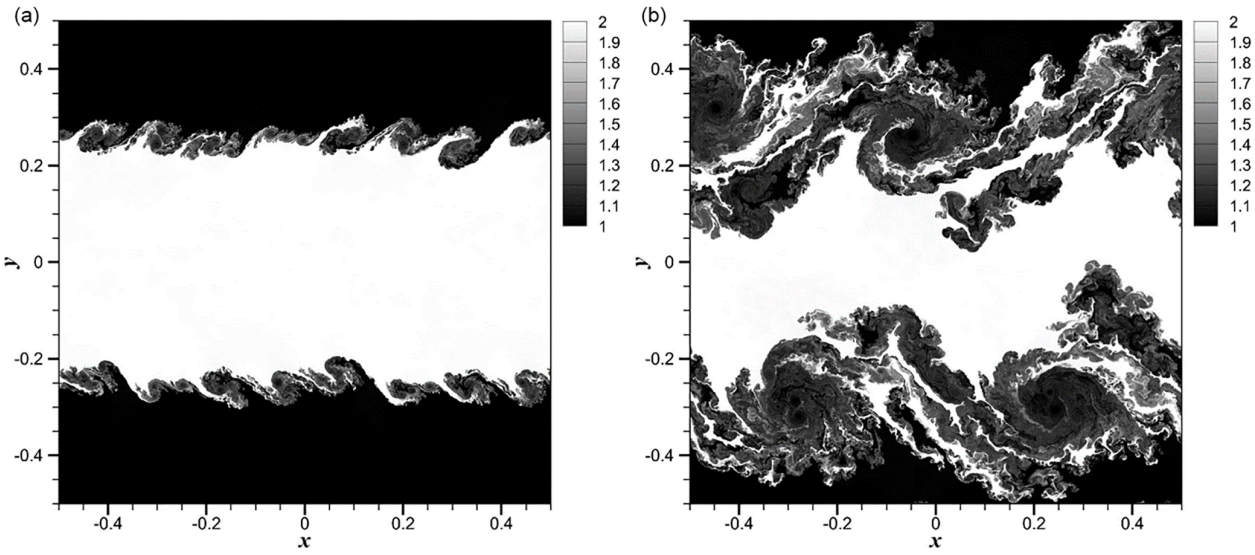

Figure 3.4: Simulation of KH instability induced turbulence in a two-fluid system (black and white) of varying density in the subsonic regime (no shockwaves present) over time. Colour indicates fluid density and the axes represnt unitless 2D space. (a) Emergence of a perturbations due to the KH instability at early time $t = 1$ (unitless). (b) Observable transition to turbulence via KH instabilities at later time $t = 5$. Results taken from Ref. [4].

observe transitions to turbulence given the presence of a KH instability [4]. Additionally, the simulations are completed in a purely 2D square area, with periodic boundary conditions around the entire area [4]. Since the focus of this investigation is on superfluid KH instabilities the work behind the simulations will not be discussed in detail except to extract a better understanding of KH instabiltities and their role in generating fluid turbulence.

From Fig. 3.4, the rolling up effect of the velocity shear on varying length-scales becomes apparent even at early times. Fig. 3.4 (a) shows a typical decaying velocity shear layer between the black and white regions due to a KH instabiltity. Comparison between earlier times, with mostly laminar flow, and later times, when the system is dominated by turbulent flow, illustrates the exponential growth in perturbations arising from the initial KH instability. Initially there emerge many small classical vortices, due to the rolling up of the shear layer, which coalesce into larger vortices. The effect then is that the total vortex number decreases over time. This suggests that the shear layer can initially be thought of as a continuum of infinitesimal classical vortices which coalesce in the inverse cascade manner such that the effect is observable as the rolling up effect [35].

Indeed, classically one often computes a shear layer as a vortex sheet (or line of vortices in 2D) comprised of point vortices (see Section 2.3), and it will be seen that this potentially has physical meaning in the context of superfluids [35]. Perturbations in the shear layer are introduced via the KH instability and gradually cause a decay of the layer to introduce turbulence. Fig. 3.4 (b) does indicate the presence of turbulence in the system via the presences of large-scale patches of vorticity and complete roll up of the two shear layers beyond recognition. Even so, there is still a well defined region of laminar flow in the high density region (white). Fig. 3.4 actually shows the subsonic regime where the shear velocity is small and no shockwave effects are present. Due to a lower velocity shear, there is a delay in the onset of turbulent features due to the KH instability [4]. This is actually a common observation in KH instability induced transitions to turbulence since similar effects are predicted in superfluid systems as discussed in Section 3.2.

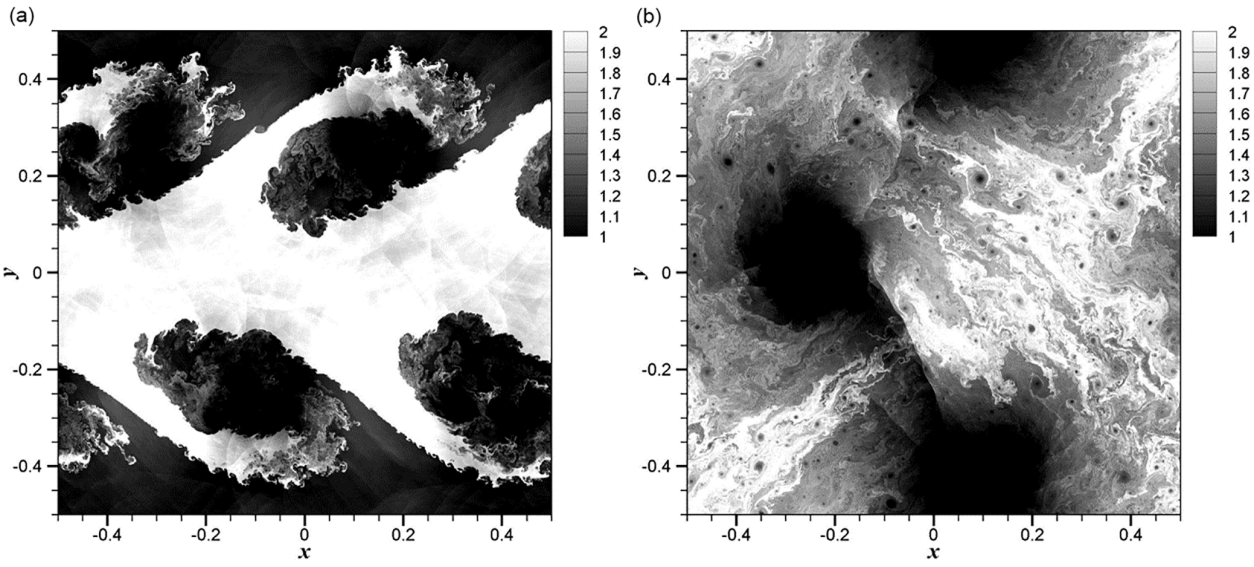

FIGURE 3.5: Same classical simulation as Fig. 3.4 only with an increase in shear velocity by a factor of 4. There exist shockwaves in this case from the extreme shear velocity. (a) Large-scale emergence perturbations due to the KH instability. (b) Complete transition to turbulence driven by the KH instability and shockwaves. Results taken from Ref. [4].

This effect made more apparent when the shear velocity is increased between the fluids such as in Fig. 3.5. Under these conditions, there is the presence of shockwaves since the system is no longer subsonic [4]. Even so, there are clear indications in Fig. 3.5 (a) of the rolling up effect on the boundary which is expected in the presence of a KH instability [4]. Even more convincingly is the final state of the fluid shown in Fig. 3.5 (b) where there has been a clear transition to turbulence over the entire 2D area [4]. Additionally, the rolling up effect at larger shear velocity values seems to be accentuated, resulting in larger vortices forming faster. This is further justified by the faster onset of turbulence in Fig. 3.5 (b) where only two large vortices dominate the space, with many smaller vortices scattered around. Clearly, coalescence of vortices arising due to a KH instability characterise transitions to turbulence in a classical fluid. This closely relates to the superfluid KH instability as is discussed in Section 3.2 where quantum vortex clustering acts as the analog for classical vortex coalescence.

To take this notion one step further, this similarity means that studying KH instabilities in superfluid systems allows one to fundamentally connect superfluid turbulence to classical turbulence by showing that the KH instability in superfluids can seed quantum turbulence. This is particularly important since, by definition, superfluids have no viscosity. So *a priori* it is not immediately evident that instability induced transitions to turbulence should even be supported in superfluid environments [5]. Yet, computational work by Baggaley & Parker strongly suggest the existence of a KH instability analog in BEC superfluids. An experimental investigation of KH instability induced transitions to turbulence in BEC superfluids is therefore well motivated, in an attempt to further understand turbulence in general and the connection between classical and superfluidity. Of course, this first requires understanding of the superfluid KH instability.

3.2 The Kelvin-Helmholtz Instability in a Superfluid

Computational work by Baggaley & Parker in 2018 predicts KH instabilities in a single-component BEC superfluid system [5]. This work served as the initial motivation for the project undertaken here. Baggaley & Parker achieved these predictions through numerical simulation of the BEC superfluid via its macroscopic wavefunction though the Madelung transformation [Eq. (2.7)] and the GPE [Eq. (2.1)] in 2D (see Section 2). The Thomas-Fermi approximation [Eq. (2.6)] was used to shape and configure the BEC superfluid as shown in Fig. 3.6 (a) and 3.6 (b). Specifically, the external potential used in the simulation was such that the atoms were trapped in two channels with equal population [5]. The potential in the channels was chosen to follow a profile that is uniform horizontally and varies vertically according to [5]:

$$V(y) = V_B\Theta\left(|y| - \frac{L}{2}\right) + V_G(t)e^{-\frac{y^2}{\sigma^2}}, \tag{3.2}$$

where Θ denotes the Heaviside step function and $L = 60$ was chosen to be the width of both channels combined. V_B is the potential barrier height outside of the channels which is chosen to be extremely large so as to simulate a hard wall potential. V_G is the barrier height

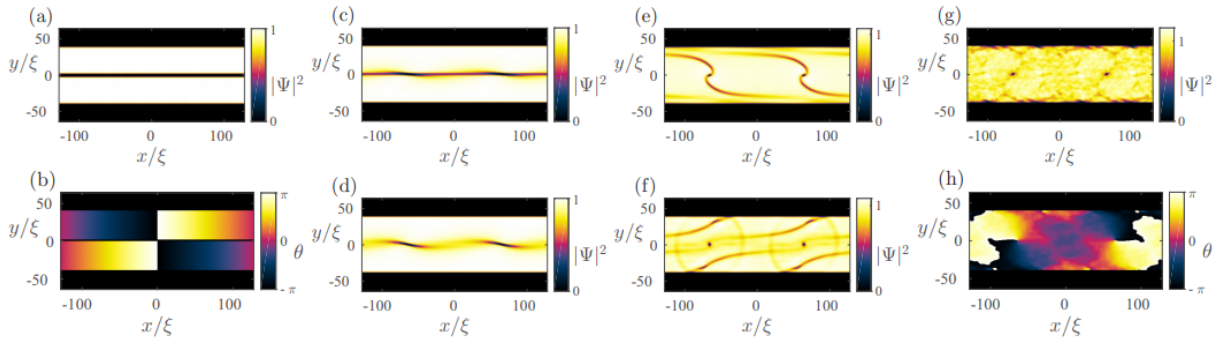

FIGURE 3.6: Example from Baggaley & Parker of a GPE simulation. Note that here spatial coordinates are normalised by the healing length $\xi = \frac{\hbar}{\sqrt{m\mu}}$. (a) Atom number density profile of the macroscopic wavefunction at $t = 0$ (unitless time). (b) Quantum phase profile at $t = 0$, indicating a velocity shear. (c-f) Density profiles at intermediate times $45 < 5 < 150$. (g) Steady-state density profile after a long holding time $t = 600$. (h) Phase profile at steady-state condition at $t = 600$. Results taken from Ref. [5].

for the separation between the two channels which is time dependent since it will eventually be removed. Finally, $\sigma = 1.28$ is just chosen for the width of the separation barrier which follows a Guassian profile [5].

Additionally, the boundary conditions at $x/\xi = \pm 100$[1] are chosen to be periodic to simulate an infinite length channel [5]. This use of periodic boundary conditions makes experimental adaptation of this work simple, since one may replicate periodic boundary conditions in a ring trapped BEC [5]. In order to imprint a current into the channels, the phase-velocity relationship [Eq (2.10)] was exploited by Baggaley & Parker through imposing a phase gradient on the initial Thomas-Fermi groundstate[2] [5]. As seen in Fig. 3.6 (b) the two channels were given the same winding number of $j = 1$, but the phase gradient was directed in opposite directions [5]. This will induce (relatively slow) flow velocity in opposite directions and so there is guaranteed to be a velocity shear of some form [5]. The barrier separating the two channels was then removed according to the function $V_G(t) = \max(0, 5 - 0.1t)$ [5]. This meant that the barrier was not removed by spatially decreasing its size to zero but by decreasing the size of the potential in the barrier region until the superfluids could freely interact after $t = 50$.

In the example simulation shown in Fig. 3.6, one can see the creation of a velocity shear [5]. Yet, instead of a continuum shear layer as discussed in Section 3.1, the superfluid system instead exhibits the emergence of two quantum vortices of the same charge. Over time it can be seen that the atom number density and velocity field of the system becomes influenced by the circulations of the two vortices (see Section 2.3) however there is no evidence of turbulent

[1] $\xi = \frac{\hbar}{\sqrt{m\mu}}$ is known as the healing length and it is a measure of the typical length scale over which the BEC density will transition from zero to the average background density of the bulk superfluid [7].

[2] A global complex phase term would not effect the probability density under this approximation.

behaviour due to the velocity shear [5]. Specifically, if a KH instability were to manifest, there would be some analog of the inverse cascading effect in the vortex boundary such that perturbations grew exponentially. Yet the vortex positions remain constant throughout the $t = 600$ simulation time. This is because there are no perturbations to the shear layer, driving transitions to turbulence, in this ideal superfluid system [5]. Thus, Fig. 3.6 shows that there does exist an analog for the classical velocity shear in a BEC superfluid but there is no indication of a KH instability in this shear layer[5].

However, it is possible to induce the required perturbations via the random noise seeded into the potential. Baggaley & Parker do so via the addition of small white noise[3] which was meant to simulate experimental conditions where thermal fluctuations in the apparatus would result in imperfect trapping of the superfluid [5]. The requirement of perturbations to drive transitions to turbulence in the BEC superfluid system is not dissimilar to classical fluid shear layers exhibiting unstable behaviour under the presence of noise. Additionally, in order to better observe the dynamics of the vortices that result, a larger winding number was induced on the initial phase of the channels. By increasing the winding in the channels, the magnitude of their flow velocity is increased and so more vortices form at the velocity shear layer [5]. Fig. 3.7 shows the outcome of the GPE simulation with the added noise and an initial 40 vortices acting as the velocity shear layer [5]. The addition of perturbations

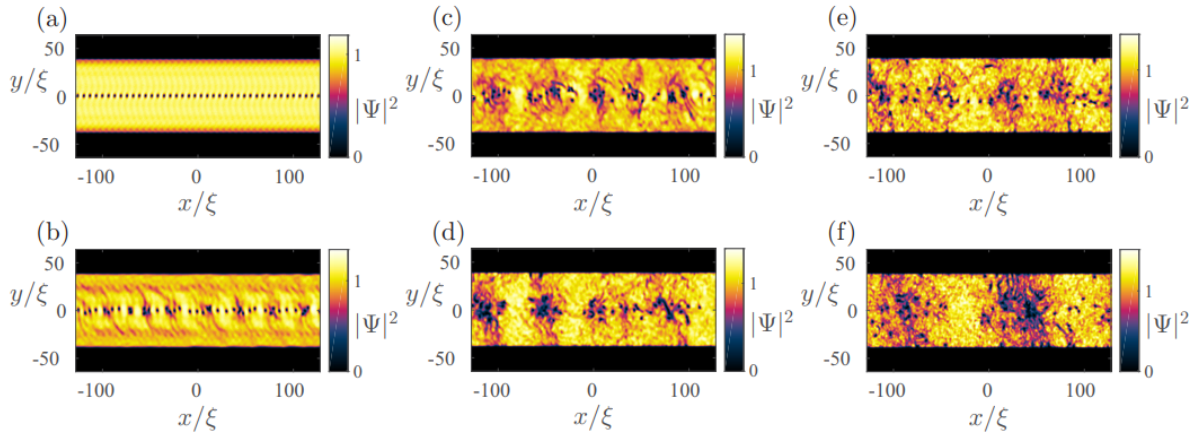

Figure 3.7: GPE simulation of KH induced transition to turbulence in a single-component BEC superfluid system. All plots show the atom number density at some instance of time. Initially, a winding number of 20 is imprinted on each channel resulting in the formation of 40 vortices. (a) Formation of the vortex shear layer at $t = 0$. (b-e) Gradual clustering observed for $200 \leq t \leq 500$ which mimics classical vortex coalescence under a KH instability. (f) Emergence of two massive clusters at $t = 700$. Results taken from Ref. [5].

through the noise result in some familiar observations about the dynamics of the shear layer. Firstly, there is a progressive clustering of the vortices throughout the simulation time-scale. Starting at equilibrium in the line where the boundary was placed, the vortices begin to

[3]Random shifts in the potential added by choosing random points in the spatial grid where the potential is slightly varied [5]

collect into clusters of 2-4 vortices [5]. These clusters combine as time goes on into larger clusters but the total number of vortex clusters must therefore decrease. Near the end of the simulation, one observes the emergence of two extremely large clusters. This is exactly the analog of the rolling up of the velocity shear layer under a classical KH instability [5]. It is actually noted by Baggaley & Parker that the clusters of vortices co-rotate and many same-charge vortices in a cluster begin to behave as classical regions of vorticity [5]. This note was somewhat vague when presented by Baggaley & Parker but it still hints at a useful observation that could be used to strengthen experimental evidence on the existence on BEC superfluid KH instability induced turbulence.

Before concluding the discussion Baggaley & Parker's work, it is important to consider the two general regimes which the vortex shear layer can fall under. In the quantum regime, there are few vortices in the boundary of the two superfluid streams and this system does not resemble a classical shear layer. The clustering of the vortices acts as an analog to the classical roll up of the shear layer under a KH instability but any further connection to a classical fluid system is difficult. In contrast, under the classical regime, where there are many vortices at the boundary, the system slowly approaches the classical limit/approximation of the shear layer as a line of infinitesimal point vortices. Thus, looking at superfluid shear systems with many vortices at the boundary is interesting from the classical point of view since it allows the KH instability instability to be considered as more than a simple analogy to classical phenomena. Indeed, similar to classical shear layers, many vortices in a superfluid system induce an effective viscosity in the superfluid through which transitions to turbulence are realised just as in classical fluids [5]. In this experiment, there is the investigation of two vortex numbers at the boundary, motivated by interest in the classical limit. Thus, this investigation is not solely interesting in observing shear layer decay into turbulence via KH instabilities, but also how this observation can further connect superfluid turbulence to its classical counterpart.

3.3 Connecting Superfluid and Classical Turbulence

It is possible to relate the decreasing cluster number and increasing vortex number per cluster in a BEC superfluid to properties of classical vortex decay in a turbulent system such as Fig. 3.5 (b) in Section 3.1. Such an analysis was undertaken by McWilliams in 1990, where a classical system of 1000 randomly placed vortices in a 2D square area with periodic boundary conditions was numerically simulated [6]. Fig. 3.8 shows contours of vorticity in such a system which indicate the presence of classical vortices [6, 36]. Simulation of the dynamics of the classical vortices was achieved via numerical solution of the barotropic vorticity equation with hyperviscous diffusion[4] [6, 36]. Fig. 3.8 indicates a clear decrease in vortex number over time. In fact it is possible to associate a power-law to the decay rate of the vortex number in a turbulent system[6, 36]. This is similar to the cluster number decay over time in the BEC superfluid indicating that the clusters of quantum vortices behave like

[4]See "The vortices of two-dimensional turbulence" by McWilliams for details on this model. This will not be discussed further here for sake of brevity and relevance.

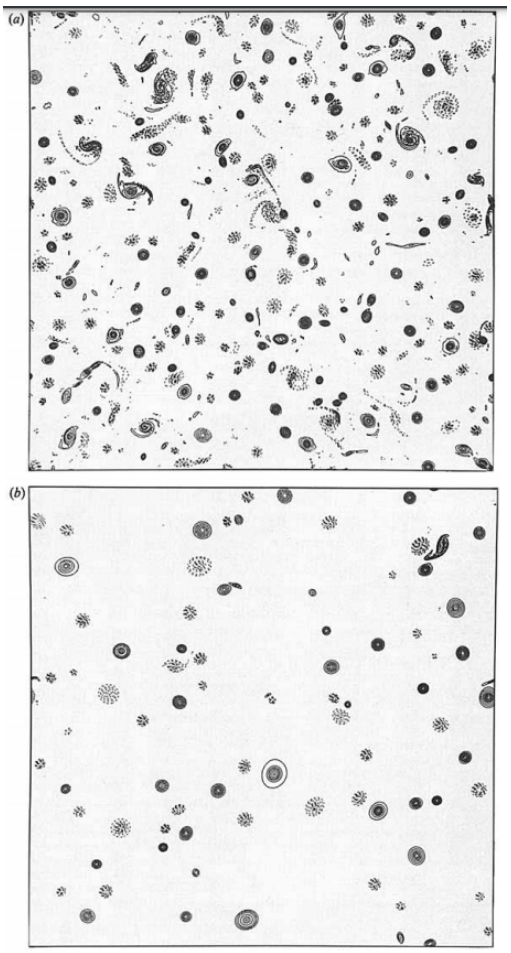

Figure 3.8: Initialised system of classical turbulence via random placement of 1000 vortices. Solid contours indicate positive vorticity and dashed contours indicate negative vorticity. Contours of zero vorticity are omitted for visualisation of vortices. (a) Configuration after $t = 5$ (unitless) time has passed. Configuration after $t = 20$. Figure taken from Ref. [6].

classical vortices in a turbulent system. In fact, one of the main experimental results in this project is the derivation of a power law for the decay rate of cluster number for comparison to the classical case.

Fig. 3.9 shows the results of numerical simulation of the vortex decay rate, indicating that the power-law scaling for a classical turbulent system lies between -0.7 and -1 [6, 36]. Looking for similar power-laws of this order will indicate that quantum vortices under a KH instability behave as classical vortices in a turbulent system which will help to connect classical fluidity/turbulence and superfluidity/turbulence. It is also possible to define a power-law for the average spatial extent of vortices over time in a classical turbulent system [6, 36]. Fig. 3.8 shows a slight indication that the vortex spatial extent will increase over time by the increased spread of contours at later times [6, 36]. Additionally, it has already been noted that the vortex number per cluster is expected to increase in a KH instability driven BEC superfluid (at least on average) [5]. Thus, in an abstract manner one can say

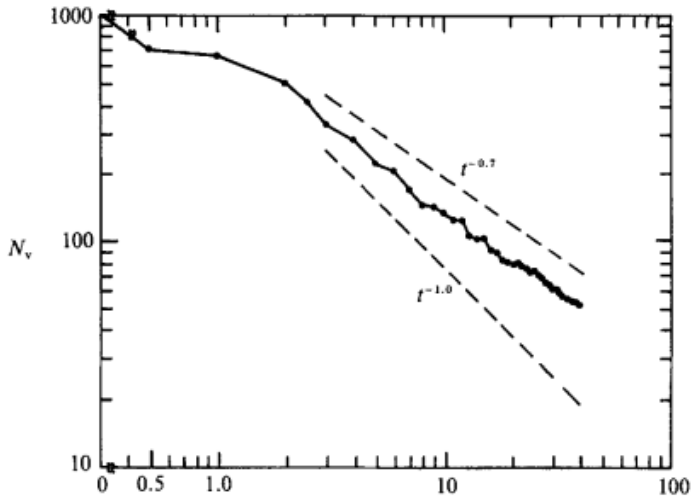

FIGURE 3.9: Log-log plot of the vortex number over time for a turbulent system described in Fig. 3.8. The dashed lines represent slopes which the log-log plot can be fitted between. The slope value represents the power-law scaling with which vortex number decays over time. Results taken from Ref. [6].

that both clusters of quantum vortices and classical vortices in a turbulent system increase their size over time. To truly make this connection would require a measure of the spatial extent of clusters in the superfluid experimentally. This would be greatly beneficial since there exists yet another power-law for the increase in vortex size over time [6, 36] which could be compared to further experimental results on superfluids. This comparison would serve to further deepen the connection between the two systems.

The methods described above all give indications of features that could experimentally suggest the presence of a superfluid KH instability and connect the experimental results to classical turbulence. Acquiring such evidence requires the use of specific experimental techniques as discussed in Section 4.

4
Experimental Methods

The focus of this chapter is the detailed explanation and justification of experimental techniques utilised to achieve the goals of the project. Sections 2 and 3 discuss the theoretical background of BEC superfluids and KH instabilities but the discussion here is on the practical applications required to achieve the desired BEC superfluid system experimentally and how data is acquired through imaging techniques. First, there is a discussion on the apparatus available at the University of Queensland Bose-Einstein condensation laboratory. Here the focus is on trapping and cooling techniques used to create BECs from ^{87}Rb atoms, including the shaping of the BEC which occurs during the final stages of condensation. Subsequent discussion is then directed towards this shaping of the BEC as well as further manipulation via a digital micromirror device (DMD). This section features specific DMD sequences used in the experiment to achieve dynamic control over the superfluid, which allowed for the generation of a velocity shear layer. These DMD sequences require optimisation of their four parameters which was experimentally achieved via supervised machine learning methods. The machine learning concept is extensively discussed in this chapter. Afterwards, there is a final shift in focus to data acquisition and analysis through imaging of the experimental system.

4.1 Experimental BEC Creation

Experimentally acquiring a BEC is a complex process, requiring a sequence of atomic trapping and cooling stages such that a cloud of atoms can be cooled below the phase transition critical temperature [7, 19]. While this experimental creation was not a key aspect of the work undertaken here, it is still worth a brief discussion into this cooling sequence so that there is no ambiguity in how the experiment was performed. Fig. 4.1 illustrates a simplified diagram of the main segment of the apparatus which is relevant to this discussion.

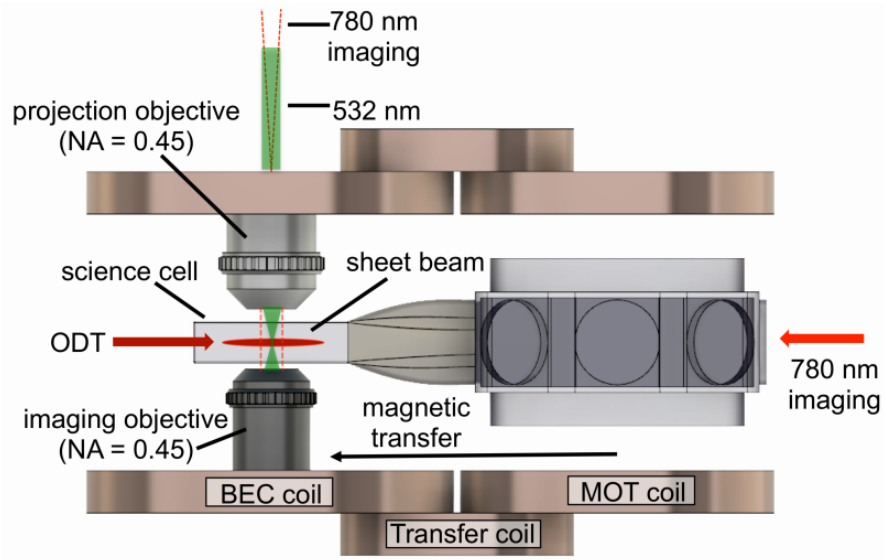

FIGURE 4.1: Highly simplified diagram of the main apparatus used to create BECs. Coils used for the magnetic fields are shown above and below the center of the apparatus. The 2D MOT used in initial cooling is located behind the 3D MOT (shown on the very right side above the lower MOT coil). The MOT coils are used for magnetic confinement in the 3D MOT. The transfer coils are use along with both the MOT and BEC coils to move atoms from the 3D MOT to the science cell region. The BEC coils are used for magnetic confinement and levitation of the BEC in the science cell. The ODT and sheet beam are optical trapping beams used in the science cell for the final cooling stage. The light from the DMD is shown by the 532 nm beam along the projection and imaging objectives. The light used for Faraday imaging is also shown by the 780 nm beam along the same direction. The horizontal imaging beam is used in absorption imaging and is not relevant for this investigation. The numerical apertures (NA) of both the projection and imaging objective are the same. Figure taken from Ref. [7].

Using this setup, the Bose-Einstein condensation laboratory at the University of Queensland is able to produce BECs in almost arbitrary configurations comprised of $\sim 3 \times 10^6$ ^{87}Rb atoms with an approximate lifetime of slightly over 30 s [7, 23]. The first step in doing so is the cooling of a large quantity of ^{87}Rb atoms via loading into a 2D magneto optical trap (2D MOT). This apparatus is not shown in Fig. 4.1 but it is located behind the main segment shown there. The atoms loaded into this 2D MOT are trapped and cooled before being transferred to the 3D MOT which is shown on the right side of Fig. 4.1. Collectively, this results in a collection of atoms with a temperature close to 100 μK scale [7]. MOTs operate via the principle of scattering combined with the Zeeman effect to achieve cooling [7, 37]. Cooling lasers detuned to be off-resonance from the D2 transition line of ^{87}Rb are used to induce the scattering events in the atoms [7]. This drives the transition $5^2S_{\frac{1}{2}}|F=2\rangle \rightarrow 5^2P_{\frac{3}{2}}|F=3\rangle$ where the hyperfine structure is induced via the Zeeman effect through a magnetic field [7]. This hyperfine structure at the D2 transition is shown in Fig. A.1 (in the Appendix).

Not all ^{87}Rb atoms will initially occupy the $5^2S_{\frac{1}{2}}|F=2\rangle$ state, as there is some population

occupying the $5^2S_{\frac{1}{2}}|F=1\rangle$ state which will not undergo the transition [7]. An on-resonance repump laser must therefore be applied to drive the transition $5^2S_{\frac{1}{2}}|F=1\rangle \rightarrow 5^2P_{\frac{3}{2}}|F=3\rangle$ in order to mitigate losses in the cooling process [7]. With atoms occupying $5^2P_{\frac{3}{2}}|F=3\rangle$ after absorption, there will be spontaneous emission into the two S states [7]. This results in a closed loop cycle of absorption and re-emission for the atoms in the MOT [7]. Thus, there a series of scattering events occurring under this closed loop which actually serve to trap and cool the atoms. This is due to the isotropy of scattering, where random emission processes result in the net momentum change on an atom being in the direction of propagation of the incident beam [7, 37]. This can be exploited by using counter-propagating beams along the spatial axes which to exert a net force on the atoms along the propagation axes thereby trapping and cooling the system [7]. Practically however, the isotropy of emission creates another problem with atoms being randomly ejected from the trap due to momentum conservation [7]. To prevent the atoms from escaping the trap before cooling can be completed, the applied magnetic field is made spatially varying so that the induced Zeeman effect is spatially dependent [7]. The outcome of such a configuration is a net restoring force towards the center of the MOT [7]. Use of all these techniques constitutes the MOT cooling stage of the experiment which results in 10^{10} atoms at around 100 μK [7].

Following cooling in 2D and 3D MOTs, there is a magnetic transfer of the atoms to a purely magnetic trap in the science cell (indicated in Fig. 4.1) [7]. Transfer of th atoms is achieved via controlled ramping of the magnetic field through three sets of coils; the 3D MOT coils, transfer coils and BEC coils [7]. Initial loading of the magnetic trap is performed via a compressed MOT (CMOT), where the 3D MOT cooling laser detuning is increased while the repump laser power in deceased [7]. The result is a decrease in scattering phenomena in the trapped atoms particularly at the CMOT center, which means that internal pressure is also decreased, resulting in an atomic density increase [7].

Only some of the states of the atoms are magnetically trappable in the experiment, thus holding the atoms in a purely magnetic trap results in a considerable population loss up to $\sim 55\%$ [7]. This population loss however actually motivates the subsequent microwave evaporative cooling stage. The atoms are then left to thermalise after the transfer. Once in the science cell, atomic transitions on the microwave energy scale are driven such that a small population of atoms is pumped out of the magnetically trappable state [7, 38, 39]. The result is a forced evaporation event where there is a net cooling effect on the remaining trapped atoms [7, 39]. This process occurs over 4 s and results in a magnetically trapped cloud of 10^8 atoms at around 15 μK [7]. This is still above the BEC transition temperature and so further evaporative cooling is required in an optical dipole trap (ODT).

Transfer to the ODT is achieved via a decrease in the magnetic field stength over 4 s while a red detuned laser beam with a 90 μm waist is activated in a region slightly below the minimum of the magnetic trap [7]. After the magnetic field strength is sufficiently small, gravity will overcome any levitation supplied by the field and the atoms will free-fall onto the ODT. The ODT operates by inducing a dipole potential in the atoms through electric field polarisation of the incident light [40]. The induced potential traps the atoms and the depth

of the potential is proportional to the power of the ODT [7, 40]. Therefore, by decreasing the power, the potential depth is decreased and more energetic atoms may escape the system. Before the BEC phase transition of the system, the atoms are transferred to a second ODT; the sheet beam [7]. Following further evaporation, the resulting atomic cloud contains a BEC of $\sim 3 \times 10^6$ atoms with a condensate fraction of $\sim 80\%$ [7]. Yet, before condensation is achieved in the sheet, the DMD is activated to shape the cloud. Operation of the DMD is yet to be discussed but in essence this device operates by painting a repulsive potential onto the sheet and the result is a quasi-2D BEC of some desired configuration. Even after condensation is achieved however, the DMD can be used to dynamically manipulate the BEC, which can be used to generate superfluid current for the purpose of creating a velocity shear layer.

4.2 Dynamic Control of a BEC Superfluid

Shaping and dynamic manipulation of the BEC superfluid, created using the apparatus of Fig. 4.1, is achieved via a DMD [23]. DMDs are examples of SLMs which are powerful, recently developed devices that offer a great degree of control over BEC systems. SLMs achieve this via manipulation of the external potential which shapes the ground state through the Thomas-Fermi approximation (see Section 2.1) [7, 23]. The DMD is simply an array of mirrors, which can be though of as a binary array where each mirror has two possible states; on and off [7, 23]. The DMD array is comprised of 1200×1920 mirrors or pixels, the states of which can be changed to paint almost arbitrary shapes onto the BEC [7, 23]. The pixels can even be varied over time to achieve desired dynamic control. Using blue-detuned (532 nm) light on the DMD will result in a repulsive potential being projected onto the sheet and so it is possible to design sequences for the pixels on a DMD which will offer dynamic control over the BEC superfluid [7]. Such sequences are prepared in MATLAB which contains a library for controlling the DMD. These sequences will be discussed in detail shortly, but their basic concept is to use basic geometric objects with an associated binary value to program regions where no repulsive light will be projected and hence where the atoms will condense into.

Due to its versatility, the DMD is an invaluable tool in this experimental investigation of superfluid KH instabilities since it allows for a procedure through which a velocity shear layer can be generated. To begin with, the computational work by Baggaley & Parker operates with two parallel but counter-flowing BEC superfluid streams in 2D channels with periodic boundary conditions on the end of the domain (see Section 3.2). This is easily translated into an experimental system with a 2D, single-component BEC superfluid in a ring trap [5]. The idea is to generate superfluid current in two concentric rings then combine the two streams in order to get the velocity shear. This of course requires exact dynamic control over the BEC through the DMD. However, utilising the DMD must be done carefully to avoid losing atoms or inducing excitations such as spurious quantum vortices. These issues can be mitigated by careful selection of the DMD sequence applied and through the use of machine learning optimisation of the sequence parameters as is discussed in Section 4.4. The focus in this section is on the DMD control sequence.

Using basic geometric objects for programming the DMD sequence is sufficient in this experiment. For example, by use of two circles it is possible to create a ring. By default, all pixels are set to the "on" state at the beginning of a DMD sequence. In this default state then, atoms in the BEC would be repelled by the potential everywhere. It is possible to instead program the initial state of the DMD pixels such that pixels within a circle of some fixed diameter centered on the DMD grid origin have their state set to "off". Now the BEC will become trapped in this circle initially. In the project, the circle diameter was taken to be either 100 μm or 125 μm as became relevant (see Section 5). This is shown in Fig. 4.2 (a) which is an image (see Section 4.3) of the BEC with the initialised DMD. Creating a

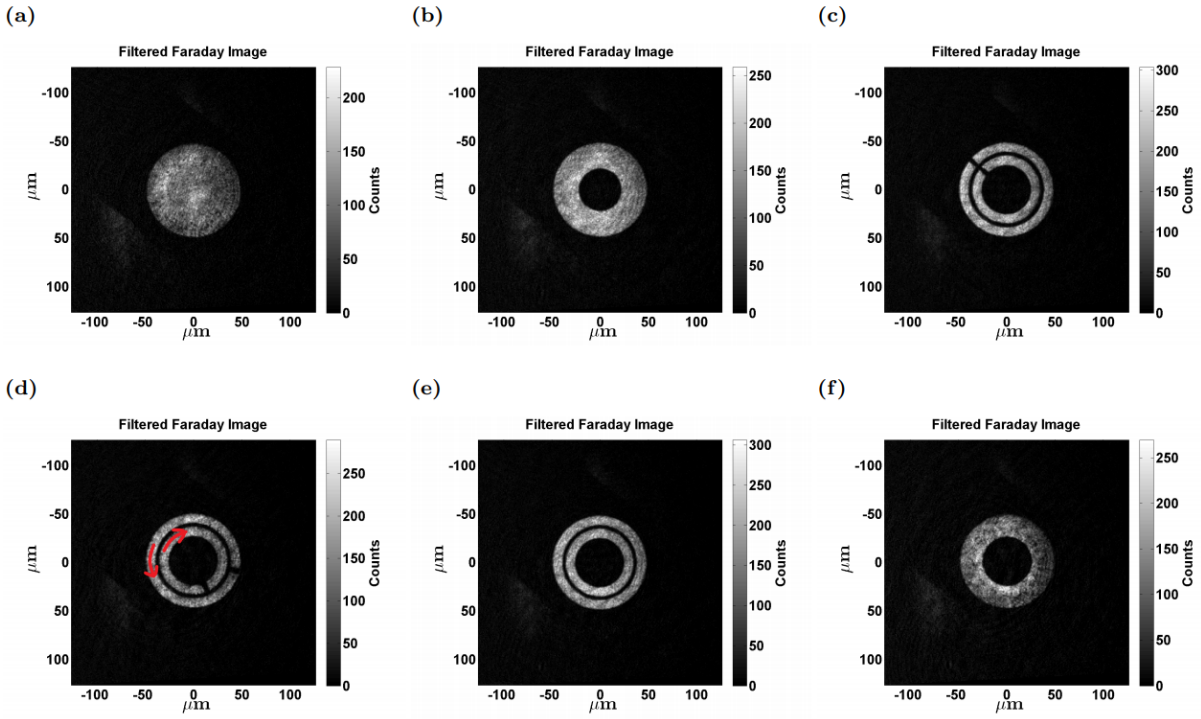

Figure 4.2: Example of a DMD sequence used to generate a velocity shear layer in the experiment. (a) Initial configuration on DMD activation. (b) Configuration after ramping in a small circle from the centre. (c) Subdivision of the BEC into two concentric rings separated by a small barrier with stirring barriers in each ring. (d) Generation of a persistent superfluid current through stirring of the channels. Red arrows indicate stirring direction. (e) Configuration after the removal of the stirring barriers (post stirring). (f) Configuration after the removal of the channel separation barrier, resulting in a velocity shear layer manifest as a line of quantum vortices.

ring is quite simple following this same procedure; simply designating a smaller circle within the original where the pixel states are switched back to "on" seems sufficient. However, it is important to be careful here, simply making this ring the starting state of the DMD will result in atom loss and potential excitations from atoms repelled by the potential of the center circle. Instead, a ring must by dynamically created. Starting from the circular configuration in Fig. 4.2 (a) it is possible to grow/ramp in the desired repulsive circle from the center over time. This is done by a linear growth of the radius over time from 0 μm to

some final value. In the experiment wo values for the final radius of 27.5 μm and 50 μm were used depending on the outer circle diameter. The resulting BEC configuration under this process is shown in Fig. 4.2 (b) where the atoms were not lost but merely pushed into the ring from the center of the condensate.

In order to progress the sequence towards generating a velocity shear layer, two channels need to be created from the ring at this stage. This is achieved in a similar fashion to the ramping in of the central barrier. Specifically, a repulsive circle can be inserted starting with a radius that is within the ring and growing only slightly such that the ring is subdivided into two channels. Practically, this is slightly more complex to achieve via programming since such a circle would immediately destroy the region where the inner channel would be located. Instead, immediately after the repulsive circle is initialised, an attractive circle is imposed over it. Immediately after this, a smaller repulsive circle is added to where the central barrier would be. These last two circles do not vary in time but now the channel separation can be ramped in without issues. Meanwhile, for sake of conserving total sequence time, two smaller barriers are ramped in which intersect the resulting channels. These small barriers are actually ellipses with large eccentricity such that they approximate flat barriers in the channels. Their insertion is performed via increasing the minor axis length over time from 0 μm to 5 μm. The result is Fig. 4.2 (c), and the BEC system is now ready for the creation of currents in the channels.

The phase-velocity relationship in Eq (2.10) gives an indication on how to generate a current in these channels. All that is required is to generate some phase gradient in the BEC [41]. Realising this phase gradient is possible through a variety of experimental techniques. For example, it is possible to employ phase imprinting, where the background potential depth is used to fix the phase over the rings [42]. with the currently presented DMD sequence it is more logical to apply stirring processes to generate the phase gradient. This is due to the simplicity of applying this method as well as the fact that machine learning methods can be applied to optimise stirring more readily in the laboratory (see Section 4.4). By moving the stirring barriers around the channels, the repulsive atom-light interactions will cause a build up of atoms. This generates differences in chemical potential which, through repulsive atomic interactions, ultimately results in the formation of superfluid flow [14]. This description can be reconciled with the phase-velocity relationship. As the barrier moves to generate velocity, the gradient of the phase of the macroscopic wavefunction must increase, which itself occurs due to the tunnelling of phase through the barrier similar to electron-pair tunnelling in a Josephson junction in a superconductor [14]. The stirring was achieved in experiment over parameters optimised by a machine learning algorithm, albeit with a fixed linear acceleration. This choice was made based on prior investigation of machine learning optimised persistent currents in BEC superfluids. The stirring is shown in Fig. 4.2 (d) where the red arrows indicate stirring direction for each channel. At this stage in the sequence, flow velocity is generated and soon the velocity shear can be created.

There is a need to remove the stirring barriers before recombining the channels to create the shear layer. This is achieved by decreasing the minor axis lengths linearly in time

over some ramp down time leaving counter-flowing superfluid currents in each channel as in Fig. 4.2 (e). Finally, the separation barrier can be removed using a similar process to its insertion. Instead of growing a repulsive circl however, an attractive circle is instead used (remembering also to impose the repulsive central barrier). The final result is shown in Fig. 4.2 (f) where there are will ideally be a line of vorties at the location of the central barrier. However, under the conditions of the image taken for Fig. 4.2 (f), the vortices are not resolvable and so cannot be easily seen. Instead certain imaging techniques are required, as is discussed in Section 4.3. By waiting a set amount of time after recombining the two stirring barriers (referred to as the hold time), the dynamics of the vortices can be observed, assuming that they are resolvable.

4.3 Imaging and Image Analysis

In the experiment, all data is acquired in the form of images of the BEC superfluid at various time. It therefore becomes important to apply appropriate imaging techniques along with methods for extracting and analysing data from images. Two imaging techniques are available with the apparatus shown in Fig. 4.1; absorption and Faraday imaging. Both these methods exploit the atom-light interaction to acquire images of the BEC system, but the parameters of interest, strengths and drawbacks of the methods vary [7]. In the work presented here, only Faraday imaging was used due to its various benefits over absorption imaging and direct relevance to observing vortex dynamics.

4.3.1 Faraday Imaging

Generally, absorption imaging is performed via looking at the attenuation of a probe laser beam through the BEC to determine local atomic density [7]. Scattering of the probe from atom-light interaction will result greater decreases of transmitted intensity past regions of higher density [7, 43]. Faraday imaging instead makes use of polarisation rotation to probe the density distribution of the BEC [7, 43]. Through the use of a probe beam, changes in the probe beam polarisation due to atomic interaction with the light can be used to determine local atom number density. The changes in polarisation arise from a refraction through the cloud [7, 43]. The BEC acts therefore as a density dependent refracting lens for the light due to interaction between the electric field of the probe beam and the atoms in the BEC [43]. The electric field thus acquires a phase shift when passing through the BEC which depends on detuning and intensity of the probe beam [7]. This results in the change of polarisation of the probe beam beyond the cloud. Due to the relationship between the polarisation and beam intensity, it becomes possible to relate the local 2D atom number density $n(x, y)$ of the BEC to the intensity of the probe beam before $I_{\mathrm{I}}(x, y)$ and after $I_{\mathrm{F}}(x, y)$ passing through the BEC via [7, 43]:

$$n(x, y) \propto \arcsin\left(\sqrt{\frac{I_{\mathrm{I}}(x, y)}{I_{\mathrm{F}}(x, y)}}\right).$$

In Fig. 4.1 the Faraday probe beam is shown superimposed over the DMD light. Due to the setup, a double shot imaging technique is actually required to determine local density.

Using the imaging objective it is possible to measure $I_{\mathrm{F}}(x, y)$ in the presence of a BEC with a single image [7]. The probe beam intensity however requires imaging via the imaging objective without the presence of a BEC [7]. Thus two images are taken in any experimental run; the first is an image with a BEC obscuring the probe and the second is taken after the removal of the BEC from the apparatus. with this procedure the atom number density of the in-sheet cloud can be determined but it is not yet obvious why Faraday imaging is preferable to absorption.

From the experimental setup in Fig. 4.1, it is clear that Faraday imaging is restricted to be along the vertical plane. Absorption imaging on the other hand is accessible along the horizontal axis and vertical direction, as indicated by Fig. 4.1. This may seem disadvantageous for Faraday imaging, but due to the optical sheet confinement the relevant vortex dynamics all occur in the horizontal plane for the quasi-2D system (see Sections 2.3 and 3.2). Thus only vertical imaging is required for this investigation. with the available apparatus, Faraday imaging is typically chosen over absorption imaging for these vertical images due to the higher resolution provided and the higher sensitivity to density fluctuations for modest system densities [7]. Absorption imaging is instead used in checking the total atom number in the cloud prior to each experimental run [7].

Being able to image the atom number density is not sufficient for the data required to investigate KH instabilities in the BEC system. The main investigation is concerned with the dynamics of vortices created at a superfluid shear layer via the process described in Section 4.2. Hence a method for detecting vortex positions from Faraday imaged BECs is required. Yet before such a method can even be prescribed imaging of the vortices themselves presents an issue. Specifically, it is difficult to resolve the vortex cores at the shear layer due to their small size. This is evident in Fig. 4.2 (f) which does contain a line of quantised vortices acting as the shear layer, but resolving them is troublesome. To circumvent this issue, time-of-flight (TOF) can be employed along with the Faraday imaging technique. TOF imaging is performed by completely removing the trapping potential and allowing the BEC to expand freely [7].

As a result of the expansion, the vortex core sizes increase and become readily resolvable. Naively one might expect free expansion to obscure the in-plane dynamics, however practically this is not the case. Due to the tight confinement vertically in the optical sheet relative to horizontal confinement, expansion mostly occurs vertically [7]. The result is that the shape and structure of the quasi-2D system is largely preserved after short TOF expansion.

It should be noted that using TOF imaging is destructive to the system, and so dynamics of vortices can only be observed using a statistical measure over many experimental runs. That is to say, it is not possible to image different hold times for a single experimental run. Instead, multiple TOF images are taken for each hold time with which quantities such as vortex number and position could be used to statistically investigate average cluster numbers and vortex numbers per cluster for each hold time. The use of TOF imaging is necessary for vortex detection but does complicate analysis of the results. In the experiment, 5 ms TOF

Faraday images are taken. This choice was made via brief investigation, where images were taken over a range of $0 - 8$ ms TOF. It was found that vortex detection (described below in Section 4.3.2) was most effective at 5 ms.

4.3.2 Vortex Detection

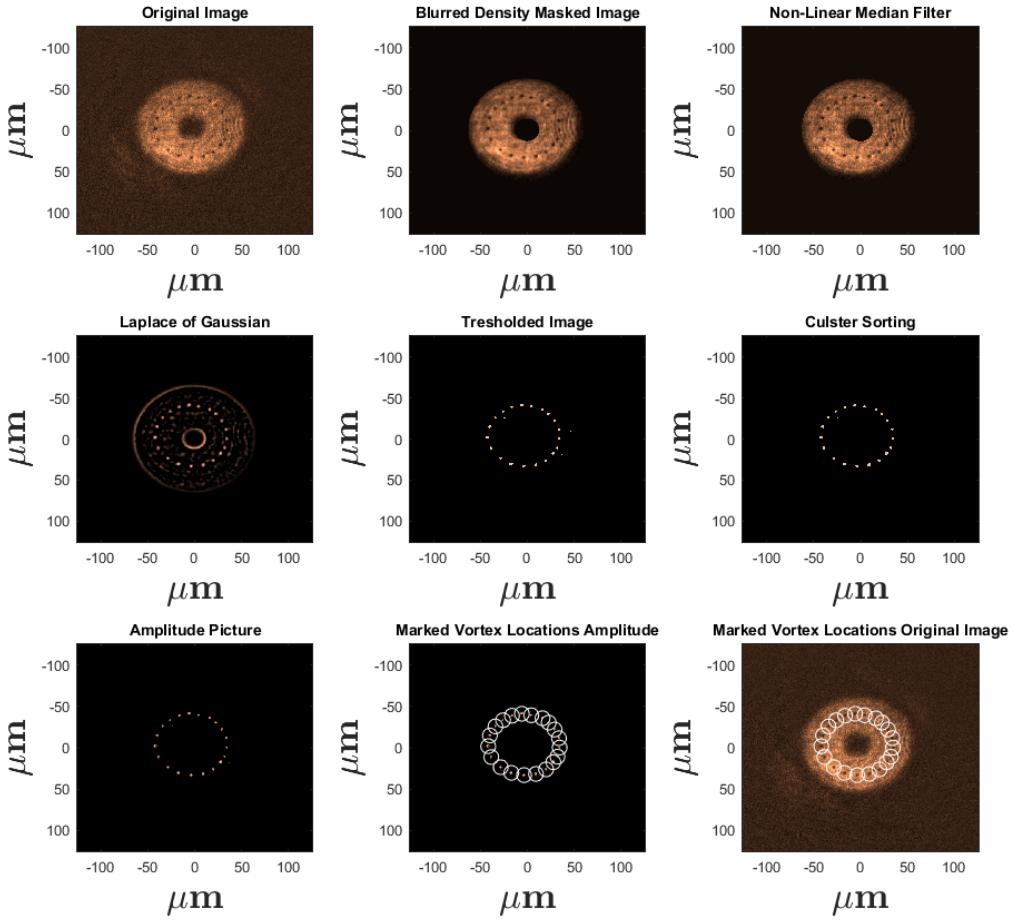

Figure 4.3: Processing of a Faraday image via the Gaussian blob algorithm [8]. The algorithm takes the original image (top left) and applies a Gaussian filter (top middle and right) which blurs regions of higher density but accentuates low density points. Afterwards, the Laplacian of the Gaussian filtered image is taken (middle left) and thresholded to isolate the vortex pixel clusted (middle). The clusters are then grouped together via a sorting algorithm (middle right) from which it is possible to determine the number of vortices and their positions via an amplitude measurement (bottom left and middle). The final result is superimposed on the original image for comparison (bottom right). This result is shown in Fig. 4.4 in more detail.

In an attempt to remove error in human analysis of counting vortices in an image and determining their position, the Gaussian blob algorithm [8] for clustering was employed in MATLAB to automate vortex detection. This pixel sorting method is useful since vortex cores appear as collections of dark pixels in the Faraday images as is clear in Fig. 4.4. It should be noted that the vortex shear produced in this image results from an optimised stirring process, used to consistently place 20 vortices in a line, found with the machine learning methods described in Section 4.4. Regardless, the image serves as an excellent example of vortex resolution and detection. The detection algorithm is shown sequentially in Fig. 4.3 and it works by first applying a Gaussian filter to the Faraday image. Applying the filter results in a blurring of regions of high density but an accentuation of low density regions such as the vortex cores. Afterwards the Laplacian of the Gaussian filtered image is taken at each point in the image, which makes the regions of transition from low-to-high density more readily observable. From Fig. 4.3 is it clear however that many such regions exist beyond just vortices however the magnitude of the Laplacian at the vortex points is significantly larger. This means that removing all points below a certain threshold in the Laplacian image should allow for only the vortices to be observable.

The choice of threshold depends on the image and has no general trend. Instead a universal threshold is typically chosen, subject to performance of the detection algorithm on a small set of images. In this experiment the threshold was set to 0.4 by using such an investigation. Once the thresholded image is acquired, cluster sorting algorithms can group collections of pixels together and construct an estimate on the number of vortices and their positions. The outcome of an example detection is given in Fig. 4.4. Here the performance

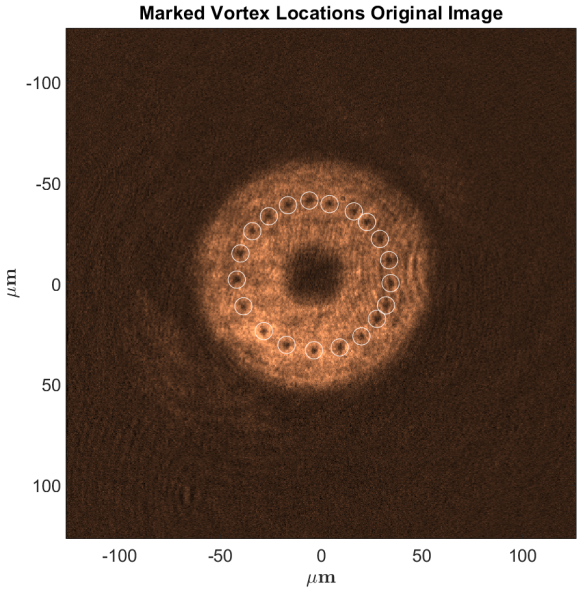

FIGURE 4.4: Faraday image of shear layer for 5 ms TOF with the outcome of the vortex detection algorithm superimposed. White circles represent points where the detection algorithm found a vortex whereas the dark pixel spots in the image represent resolved vortices.

of the vortex detection algorithm is completely accurate, but generally this is not the case. It is common for the algorithm to not detect vortices with slightly smaller cores due to the thresholding. Additionally, if collections of vortices are close together, the algorithm likely detects the collection as a single vortex. To account for the error introduced via the detection algorithm, there is a need apply the detection algorithm to multiple images taken over different experimental runs of the same system configuration. This will allow for a statistical representation of the detection, complete with error. In the machine learning optimisation data, three images of each parameter set were taken for such statistics whereas in the vortex clustering investigation five images were used for increased precision and accuracy of the results. These choices were made with a balance in accuracy and data acquisition time in mind. As machine learning is not the main focus of the investigation, less time was allocated towards the optimisation procedures. In the vortex clustering data acquisition more time was allocated and so more images could be taken which would increase the accuracy of the results. However, the application of the vortex detection algorithm can be extended beyond simply cluster analysis.

4.3.3 Flow field from Vortex Detection

Once the positions of the vortices are given through the Gaussian blob algorithm, it is possible to approximate the streamlines and velocity flow field of the superfluid. This is achieved through the *Electrostatics(es) module* in COMSOL [44, 45]. This module uses electrostatics equations to derive the electric field and potential of arbitrary charge configurations [44, 45]. It is possible to model the quantum vortices as point sources in an electric field [44]. Under this approximation, the electric potential is analogous to the streamfunction of the superfluid containing the vortices and so the velocity flow field and streamlines can be approximated from the electric potential in the model[1] [44, 45]. One caveat of the application COMSOL in this thesis is that any background persistent current remaining after the combination of the two rings is assumed to be zero. Checking whether this is the case with the experiment was not done, as the KH instability and resulting turbulence should behave similarly in a rotating system. Checking for this background flow will be the subject of future work. Regardless, use of the stream profile of an image is quite useful for qualitative results about transitions to superfluid turbulence as well as vortex clustering.

4.3.4 Vortex Clustering

On the topic of clustering analysis, it becomes relevant to discuss the clustering algorithm used to detect whether clusters of quantum vortices were present at various hold times. The clustering algorithm employed was that of the "density-based spatial clustering of applications with noise" (DBSCAN) [9, 10]. This algorithm operates by arbitrarily taking any point p in a data set D then considering a ball $B_\varepsilon(p)$ of radius ε around p [9, 10]. This ball is defined by a distance function/metric, typically taken to be the Euclidean distance (as is the

[1]For more information on the use of COMSOL in superfluid stream simulations, the reader is referred to the superfluid optomechanics website by Christopher G. Baker: `https://christophergbaker.com/superfluid-optomechanics/`. This website coincides with Ref. [45]

case here) [9, 10]. If there are $N_\varepsilon(p)$ data points (including p) within distance ε of p there is the potential for a cluster to be present. One defines a minimum number of points M such that the condition for a cluster is that $N_\varepsilon(p) \geq M$ [9, 10]. If this is the case, all points in the ball are said to be directly density-reachable and are added to the cluster [9]. All directly density-reachable points to p are then individually considered in a similar manner. Specifically, for a point q that is directly density-reachable from p, one again considers an ε-ball $B_\varepsilon(q)$ and finds other points within the ball [9]. It is not necessary for the number new points

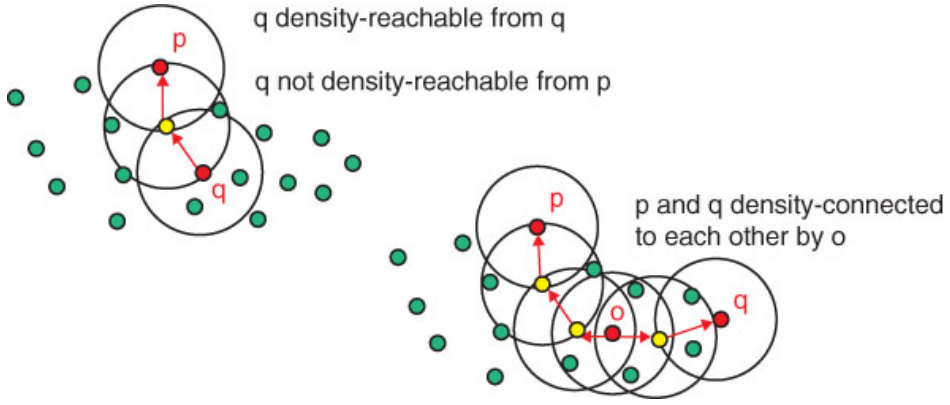

FIGURE 4.5: Example illustrating DBSCAN cluster sorting via density-reachable and density-connected points in a data set. Clusters are constucted from all density-reachable points. Figure taken from Ref. [9].

$N_\varepsilon(q)$ to satisfy $N_\varepsilon(p) \geq M$ [9]. Any new points which are directly density-connected to q but outside of $B_\varepsilon(p)$ are said to be density-connected to p. Points that satisfy $N_\varepsilon(p) \geq M$ are called core points whereas points which are simply density-connected are called border points. If p cannot find at least $M-1$ points in $B_\varepsilon(p)$ then it is classified as a noise point not associated to any cluster. The concept of density reach-ability for clustering is shown in Fig. 4.5. DBSCAN associates clusters to finding the maximal set of density-connected points from some arbitrarily selected initial core point [9]. This process of selecting core points and adding border points is repeated until all points in D are classified as being in some cluster or as noise points [9, 10]. In the worst case where the algorithm performs one ε-ball inquiry for each n points in D, DBSCAN has computational complexity varying from $\mathcal{O}(n\log(n))$ to $\mathcal{O}(n^2)$ depending on how efficiently indexing of the data points is performed (usually problematic for higher dimensional data sets) [9]. The choice of M and ε are crucial to the success of DBSCAN as they define the cluster parameters.

M is typically chosen based on how sparse the data set is [10]. For the experiment here, there are only at most 30 data points (vortices) to sort into clusters which is a relatively sparse data set, and so $M = 2$ is chosen. This will ensure that clusters are only considered when at least two vortices are close to one another. Any vortices classified as a noise point will be treated as clusters of single vortices for the purposes of the analysis. The choice of ε is more complex to define and is discussed in detail in Section 5. Generally however, ε is chosen via some statistical measure of the nearest-neighbour distances between vortices. There are many issues which can arise from a poor choice of ε which are illustrated in Fig. 4.6. If ε is

not sufficiently large, then DBSCAN will fail to detect certain clusters which are more spread [10]. In the worst case, no clusters will be detected. In contrast, choosing ε that is excessively

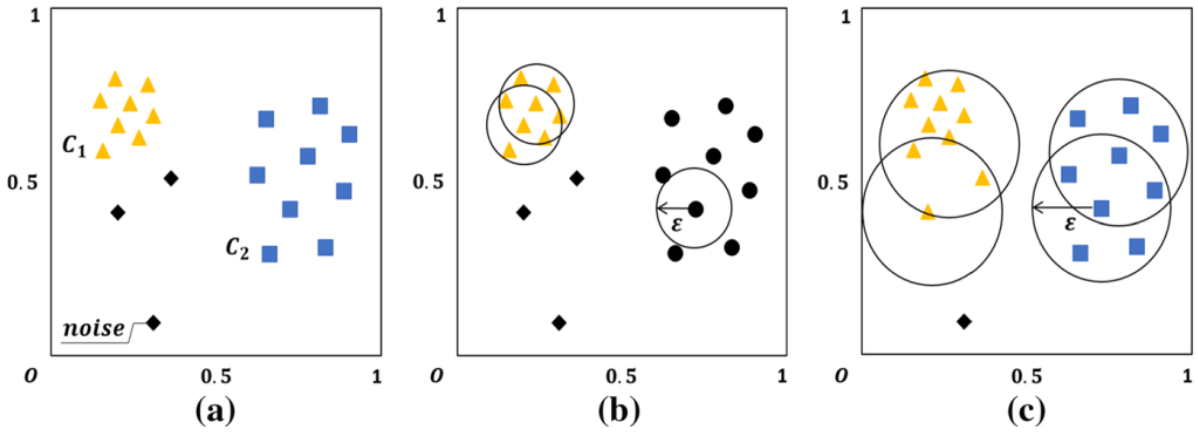

Figure 4.6: Illustration of problems with DBSCAN having global variables on an example data set. (a) Shows true clustering of the data points known beforehand. (b) Choosing ε that is too small results in failure to detect cluster C_2. (c) Choosing ε that is too large results in the inclusion of noise points which are not actually part of C_1. Figure taken from Ref. [10].

large results in the addition of points to clusters which should not be included [10]. In the worst case here, all points in a data set will be placed in one large cluster. These issues arise from the fact that ε and M are global variables when they should vary between clusters [10]. Alterations to the DBSCAN algorithm are possible which somewhat aid in removing the global variables such as grid based density clustering [10]. Such algorithms however increase computational complexity substantially [10] and are impractical to implement within the time-frame of the project. Thus, DBSCAN suffices for vortex cluster detection in the experiment given careful attention to the choices of ε and M. MATLAB is employed to implement DBSCAN in the experiment. Specifically, within the *Statistics and Machine Learning Toolbox* is the function dbscan(X, Eps, MinPt) which takes in a data set of positions X, the ε value as Eps and the minimum points M as MinPt outputs a vector of integers. The integers represent the cluster labels, with noise points classified as -1 and clusters with positive integers. The index of the output vector corresponds to a vortex with the same position index in X. Using the output vector it is possible to find the cluster number of an image as well as the mean, median and maximum vortex number per cluster. This is outlined in the pseudo-code in Appendix A.2 which was used to perform clustering analysis in Section 4.

Combining the imaging and image analysis techniques discussed in this section with machine learning optimised velocity shear layers allows for the observation of evidence for KH instability induced transitions to turbulence in experimental BEC superfluids.

4.4 Machine Learning Optimisation Concept

Before the experiment on KH instabilities in BEC superfluids could be completed, there was the need to find some methods for optimising the stirring process discussed in Section 4.2. Optimisation is required in order to efficiently and consistently realise different shear velocity values via stirring of the BEC superfluid channels. Optimisation increases the replicability of the experiment which is especially important when considering multiple images over different experimental runs are required to construct a statistical measure of vortex dynamics. Additionally, a higher level of control over the velocity shear layer can be achieved via optimising the stirring to produce fixed vortex numbers at the superfluid boundary. The ability to realise different shear velocities is important for testing vortex dynamics over a range of initial conditions. Optimisation also minimises noise/excitations produced via stirring which allow for the study of KH instabilities in a more ideal system where the focus can be purely on vortex dynamics. Overall, the motivation behind optimising the creation of the velocity shear layer is evident but some issues arise in practically achieving this optimisation.

One of the issues is that the parameter space of the stirring can be quite large and, even when the parameters are simplified, the relationships between the parameters and an ideal, controlled shear layer are not known in the experiment. This meant that brute-force optimisation as well as any human optimised methods were inefficient and impractical. Instead, a fast and accurate machine learning method would be required to optimise stirring. There are four parameters which classify a stirring process in the experiment; 1) the ramp in times for all repulsive barriers, 2) the ramp out times for the stirring and separation barriers, 3) the total stirring time over which the stirring barriers are moved around the channels and 4) an acceleration coefficient/scaling which multiplies the acceleration profile for the stirring barriers. The acceleration profile itself was fixed to be linear for simplicity. Due to the complexity of the parameter space, it becomes inefficient to use human optimised methods in the experiment. Instead machine learner controlled optimisation is more appropriate due not only to efficiency but a lack of preconceptions about these experimental parameters.

4.4.1 Machine Learning Algorithm

The machine learning algorithm employed in the experiment was that of a Gaussian process (GP) regression. This is a supervised machine learning method, meaning that there is an external measure of the error produced by the parameter model used by the learner [46, 47]. This error is quantified via a loss or cost function which is minimised when the parameter set is optimum [47–49]. Supervised learning methods typically feature a data set $\mathcal{D}(\mathbf{X}, \mathbf{y})$ comprised of the set of independent variables $\mathbf{X} = \{\mathbf{x}_1, \mathbf{x}_2, \ldots, \mathbf{x}_N\}; N \in \mathbb{N}, x_i \in \mathbb{R}^m, i \in \{1, 2, \ldots, N\}, m \in \mathbb{N}$ and dependent variables $\mathbf{y} = \{y_1, y_2, \ldots, y_N\}$ associated to the outcome of each independent data point [46, 47]. In the experiment, the set $\mathbf{X}$ is given by the parameters which control stirring and the dependent variables $\mathbf{y}$ are given by the vortex number at the shear layer for each stirring parameter set. The learner has its own parameterisation θ of a mathematical model which maps any dependent variable $\mathbf{x}$ to it associated output y via a function of the learner parameters $f(\mathbf{x}; \theta)$ [46, 47]. The cost function $\mathcal{C}(\mathbf{y}, f(\mathbf{X}, \theta))$ is then defined as the error in using the learning model parameters

θ to fit the complete independent set $\mathbf{X}$ to the outcomes $\mathbf{y}$ [46, 47]. In the experiment, two cost functions were used, defined as:

$$\mathcal{C} = (\text{Target Vortex Number} - \text{Measured Vortex Number})^2 , \tag{4.1}$$

$$\mathcal{C} = |\text{Target Vortex Number} - \text{Measured Vortex Number}| , \tag{4.2}$$

where the target vortex number was fixed and the measured number was determined via vortex detection (see Section 4.3). These choices of cost ensured that the vortex number at the shear layer would reach some target number. For the first set of optimisations, Eq. (4.1) was used. The squared term punishes large deviations from the target vortex number. Small deviations of one vortex from the target would not have large costs but, because of the squaring of the error in $\mathcal{C}$, a system have two or more vortices away from the target was severely punished. This would ensure that the optimised parameters not only have the target vortex number but also did so consistently. However, for the final optimisation performed in the experiment (to a targe of 30 vortices), the cost function in Eq. (4.2) was exclusively used. The reason for this change was the observation that variation in vortex number was unavoidable for large target vortex numbers, and so the punishment of slight variations in the squared cost would become problematic.

Other choices of cost do exist and having increased cost complexity might have aided in slightly increased accuracy but, as is discussed in Section 5.1. Ideally, one would measure this cost constrained to the separation barrier region and then increase cost according to any excitations produced by stirring. This was attempted but the outcome was only a decrease in the accuracy of the optimised parameters to truly generate a controlled shear layer. These basic costs presented here are more than sufficient for the purposes of generating controlled velocity shear layers using GP regression machine learning.

GP regression is performed on the basic principle of finding θ by minimising $\mathcal{C}$ subject to some training data set[2]. The model developed by the learner through GP regression can then used to find the optimum stirring parameters by inference.

4.4.2 M-LOOP

To apply the GP regression in experiment, M-LOOP was applied. M-LOOP is a machine learning controller developed at ANU by Wigley *et al.* with the specific intention of controlling parameters in ultracold atom experiments [50, 51]. M-LOOP had been shown to be successful at quickly and accurately finding optimum parameters in such experiments and was already in application in the University of Queensland Bose-Einstein condensation laboratory before this project began. Using M-LOOP requires the input of the learner type since many are available to this controller besides the desired GP regression (such as neural-networks) [51]. The choice of a GP regression therefore is based on prior experience in the

[2]GP regression actually features statistical modelling via Bayesian inference [47, 48], where the prior distribution is taken to be a Gaussian distribution of functions which are slowly reduced to a smaller set of functions that are able to accurately model a training data set. For sake of brevity this is not discussed here but the reader is indead referred to Ref. [47] for details on GP regression.

laboratory using this learning method and also due to the lack of functionality of the neural-network learner under the installed package of M-LOOP.

Operating M-LOOP in practice meant integration of the software with MATLAB which controls the DMD sequences. This was achieved via running M-LOOP in a Unix environment on a separate device to that which controlled the experiment, and allowing file transfers between the two through a shared folder. Following integration of the software, M-LOOP was able to feed the four stirring parameters (listed at the beginning of this section) into the DMD allowing vortex detection to be performed in order to measure the cost $\mathcal{C}$ [Eqns. (4.1) & (4.2)]. The cost was then fed back into M-LOOP so that the learner could associate how well the experiment ran compared to the desired outcome. In practice, the experiment was run three times using each parameter set, and the cost of was taken to be the mean of the three independent cost values. Error was also estimated using the three trials via the standard error measure of the costs. The learner would then be able to find the optimum stirring parameters by finding the minimum cost, which ideally would be zero according to Eqns. (4.1) & (4.2).

In order to train the learner to achieve optimisation, 10 training runs were used where the learner generated and fed random stirring parameters to the experiment. The statistical measure of cost was performed using these parameters and returned to the learner. After these 10 training runs, convergence to optimum stirring was observed. This optimisation was performed for two choices of target vortex numbers; 20 and 30. The outcomes of all machine learning based experiments are discussed in Section 5.1.

5

Transitions to Turbulence in Experimental Bose-Einstein Condensates via Kelvin-Helmholtz Instabilities

This chapter presents and analyses the results from the experiment using methods as described in Section 4. Despite the main focus of the investigation being on quantum vortex dynamics, a large portion of the experimental work was dedicated to machine learning optimisation of the superfluid velocity shear layer. The first section of this chapter discusses this work. Here, all experimental work performed to test and apply the machine learner M-LOOP is analysed and the outcomes of the learner optimised stirring processes are discussed in detail. The second section focuses on the dynamics of vortices at the optimised shear layer and how these qualitatively and quantitatively supports the transition to turbulence via KH instabilities in the experimental BEC system. The relevant quantities and trends of vortex cluster dynamics discussed in Section 3.2 are shown to persist in the experimental system, including power-law scaling of the cluster number over time which is comparable to classical vortex systems. The outlook and future work leading on from the results presented are discussed in the subsequent chapter.

5.1 Configuring and Applying Machine Learning

Application of M-LOOP to produce consistent and controlled shear velocities (manifest as vortices at the superfluid boundary) was a key aspect of the experiment. The investigation of multiple shear layer conditions is necessary for diversity in the data as well as building further connections between a classical and superfluid shear layer. This is because a discrete vortex shear layer will approach the classical continuum of point vortices at the shear layer in the limit of large vortex number. Thus having data sets with low vortex numbers and

large vortex numbers will enable a comparison between the behaviours of the "quantised" shear layer case an the "classical" limit, thereby establishing a connection between the two regimes, while also exploring phenomena unique to the quantum regime. M-LOOP was tasked with optimising a set of four parameters such that the cost in Eqns. (4.1) & (4.2) was minimised to zero. The results from machine learning controlled optimisation are presented in this section and their influence on the experiment is discussed.

5.1.1 Preparing for Machine Learning

Before optimisation via machine learning was undertaken, some foundational work was first required in preparation. The first of which was a validation test as to whether a vortex shear layer could be produced in experiment. To this end, arbitrary stirring parameters were chosen and standard Faraday images were taken in TOF just to inquire into whether such a shear layer would be achievable and resolvable. The parameters chosen were 500 ms total stirring time, 200 ms ramp-in time, 200 ms ramp-out time and an acceleration scaling of 20 (see Section 4.4). This first experiment made use of a ring trapped BEC with an outer diameter of 100 μm and inner diameter of 50 μm. Finally, there was no hold time imposed on the system since vortex dynamics were not of interest at this point. Resolvability of the vortices was tested simultaneously by taking images over different TOF values of 0 ms, 3 ms, 5 ms and 8 ms.

These images are shown below in Fig. 5.1. In all instances there is a clear emergence of a ring of vortices where the separation barrier was located. This result was promising from an experimental standpoint since it suggested that a velocity shear layer could indeed be generated in the experimental BEC. As expected however, the arbitrary parameter choice also resulted in many spurious vortices away from the shear layer indicating that optimisation methods were needed to only generate the vortex shear layer. Furthermore, the different TOF images show the growth of the vortex cores with increased TOF. In Fig. 5.1 (a) where there is no TOF, the vortices are barely resolvable and the vortex detection algorithm scarcely detected any vortices in this image. A similar effect is seen in Fig. 5.1 (d) with 8 ms TOF where the expansion has occurred for slightly longer than required. Thus, while it is easier to resolve the larger vortex cores, many vortices seem to overlap and even show signs of moving out of focus for the imaging objective.

Fig. 5.1 (b) and (c) on the other hand represent ideal cases, where the vortex cores are easily resolvable but the system remains intact with 3 ms and 5 ms TOF respectively. While both TOF choices are excellent candidates for the remainder of the experiment, the vortex detection algorithm more accurately detected 5 ms TOF vortices than that of the 3 ms instance. It is however worth mentioning that only one set of images was used to determine this result when ideally multiple images at these TOF values should have been taken to develop a statistical measure of the performance of the vortex detection algorithm for each instance. Fortunately, the choice of 5 ms was sufficient at allowing for accurate vortex detection throughout the remainder of the experiment.

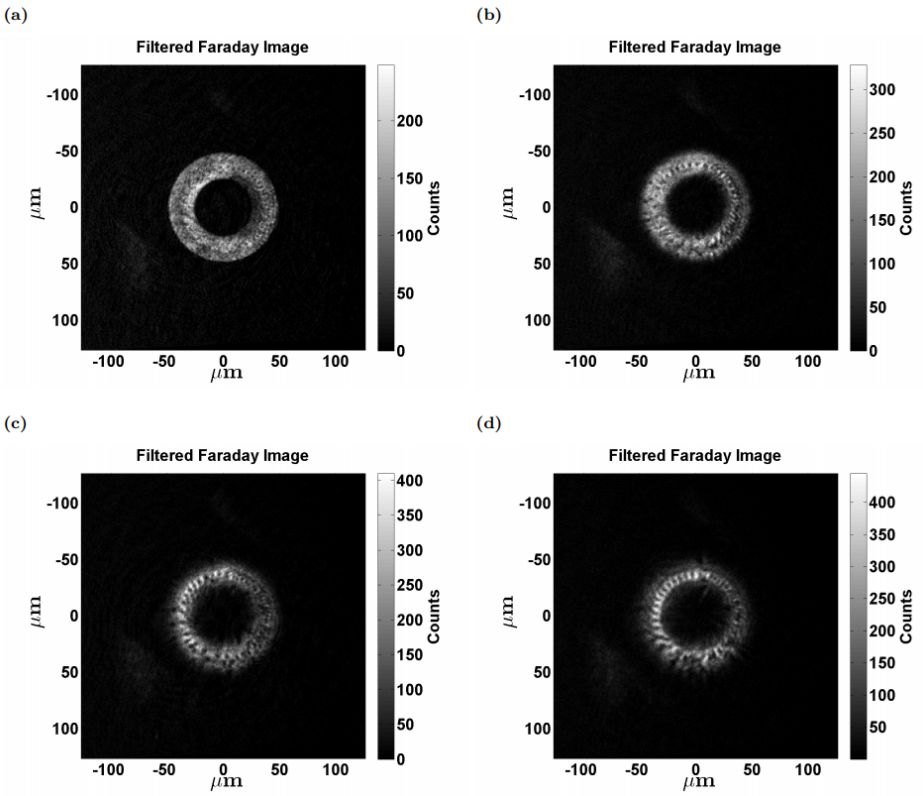

Figure 5.1: Varying TOF images with the initial (arbitrary) stirring parameters. (a) 0 ms TOF. (b) 3 ms TOF. (c) 5 ms TOF. (d) 8 ms TOF.

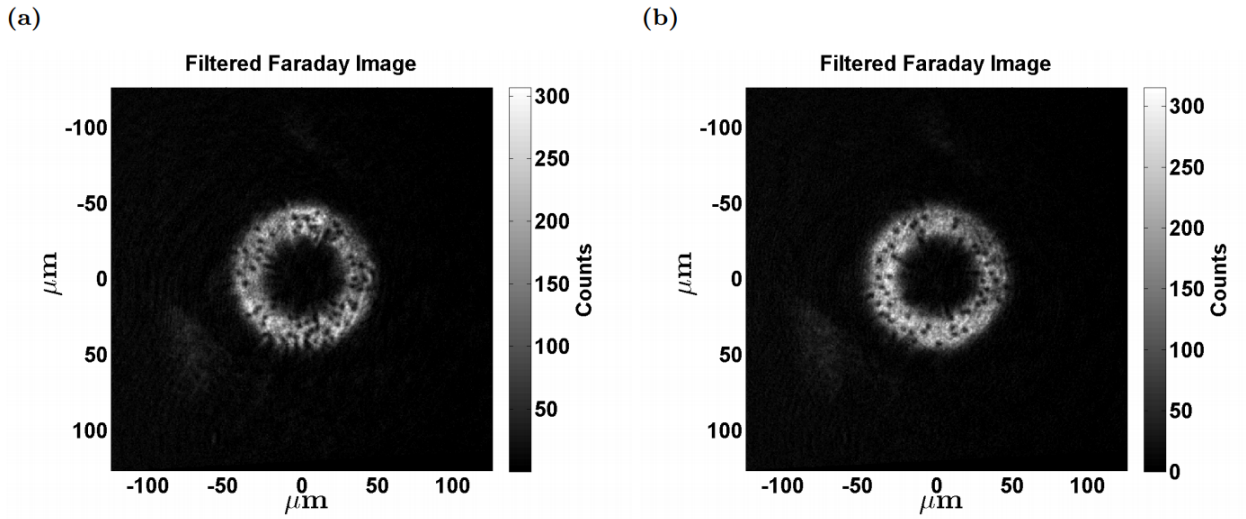

Figure 5.2: 5 ms TOF with arbitrary stiring parameters with some hold time was imposed before taking the image. (a) 100 ms hold time. (b) 250 ms hold time.

The outcomes from this trial are clear; shear layer creation is possible and vortices will be imaged under 5 ms TOF. At this point however, it is only speculated that the KH instability is present, as to truly verify this claim it becomes necessary to observe a transition to turbulence via roll-up and clustering of the shear vortices. If the KH instability is present, the initial shear layer will rapidly decay via the emergence of turbulence, arising from the small perturbations seeded into the shear layer (see Section 3.2).

The next preliminary test conducted was to see if clustering could be observed at different hold times. The same stirring parameters and ring dimensions were used for this trial only now the system was held for 100 ms and 250 ms. The idea with this was not only to attempt to observe clustering but also to gauge the timescales under which potential clustering occurs. Fig. 5.2 shows the Faraday images under these hold times.

These preliminary tests were performed as qualitative measures to understand whether there was a possibility for success in the investigation and several initial conclusions can be made. There is a clear shift of the vortices from the initial ring configuration is observed indicated a clear movement from equilibrium which is already suggestive of some instability in the system. Furthermore, there seems to be clustering in the images, which is indicated by regions of large concentrations of vortices followed by regions of no vortex observations. Of course, precise clustering measurement would require quantitative analysis of the images to make this observation exact. Additionally, if clustering is present, it is clear that 250 ms hold time is not sufficient to see a progression of the vortices into only two large clusters as was the limit in Baggaley & Parkers computational work on a similar system (see Section 3.2) and so subsequent experiments were performed up to considerably longer timescales.

Furthermore, there is an obvious loss of vortex number between the two times. This suggested that main dynamics experiments should be performed with more finely spaced hold times. The spacing of hold times for the clustering experiments was 10 ms due to this observation and since this small time step allowed for more data to be acquired. The loss of vortices also further suggested that the dimensions of the ring were inefficient for observing dynamics and so alterations would have to be made. Eventually, subsequent trials would be performed with a ring with an outer diameter of 125 μm and inner diameter of 27.5 μm. Before the main data was taken in the thicker ring, the preliminary system was used to test the success of the machine learning algorithm. These results are discussed in the next section.

5.1.2 Thin Ring Optimisation

The use of arbitrary stirring parameters in the preliminary experiments proved to result in considerable numbers of undesirable excitations in the ring. Optimising the stirring process via M-LOOP as discussed in Section 4.4 resulted in quickly and accurately removing these undesirable excitations and generating controlled shear layers. The importance of such machine learning optimised initial conditions cannot be overstated. The isolation of a shear layer ensures that all conclusions made about vortex dynamics would be the result of effects

originating from the shear layer. Additionally, the added control from the machine learner over the initial vortex number would allow for multiple initial conditions to be investigated and thus compared to evaluate the strength of any conclusions made. The first complete optimisation was in the thin ring configuration to a target number of 50 vortices.

This large number was chosen in order to verify the limits of the optimisation as human optimised stirring processes had yet to reach this many vortices without inducing undesirable excitations. M-LOOP supplied an initial 10 parameter sets with randomly generated parameters for training. For each parameter set, three images were taken and the average cost and standard error were returned into M-LOOP as the total cost and uncertainty of the parameters. Following training, the learner would make an attempt at inferring the optimum parameter set. The cost for this could be returned to M-LOOP and compared to an estimate for said cost. Depending on the accuracy of this result, M-LOOP could provide

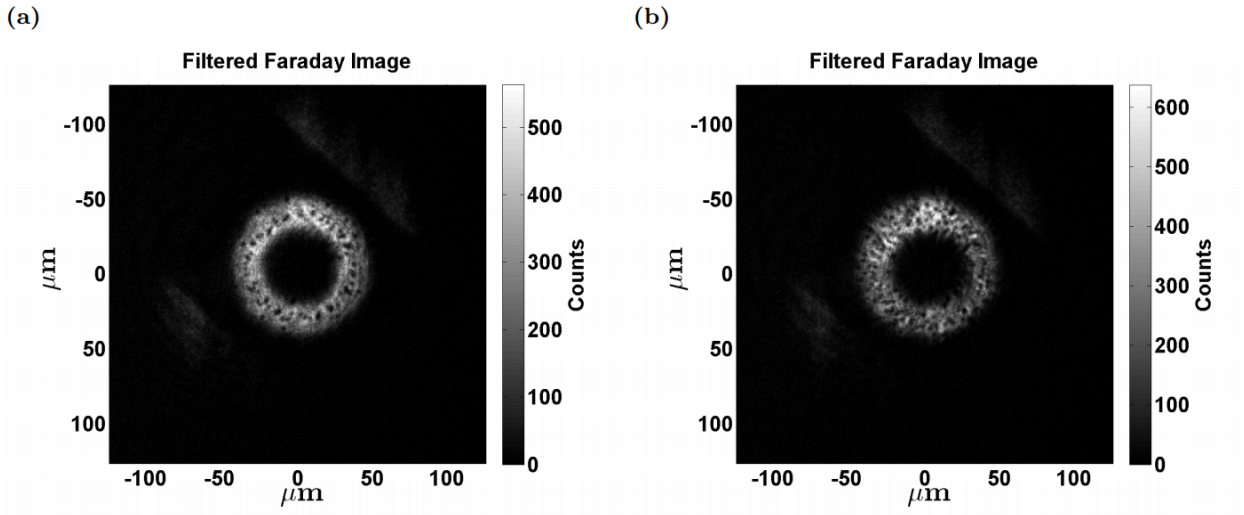

Figure 5.3: Examples of good and poor runs as classified by the cost function. (a) Good run but not ideal due to the lack of target vortex number. Low, non-zero cost. (b) Poor run due to excessive vortices (from stirring in the super-sonic regime). Very high cost.

further inferences. After four machine learning inferences, M-LOOP would present a new random parameter set simply to break up the process of inference with new data.

For this optimisation, 30 trials in total were performed simply to observe convergence of the process. Yet before looking at accuracy and convergence, it was important first to verify that the cost function chosen in Eq. (4.1) gave the desired classifications for "good" and "poor" parameter sets. Examples of good and poor runs under this cost function are shown in Fig. 5.3. The low cost example in Fig. 5.3 (a) shows a trial where the vortex shear layer is clear but the total number of vortices is not at the target number. In such a case the cost was found to be relatively low but non-zero as expected. Images with similar cost presented stirring parameters that were subsonic as suggested by the lowered number of undesirable excitations. Optimisation of said parameters was still not achieved at these points however.

In contrast, when stirring was super-sonic, excessive numbers of spurious vortices were observed, which obscured the shear layer and even greatly effected the bulk density of the BEC. An example of such an outcome is shown in Fig. 5.3 (b), which is also a typical image for considerably high cost parameters. These two images are only examples of costs associated to parameter sets as displaying all 90 images for the 30 trials is uninstructive. The general trends discussed here are sufficient to summarise the trends in the entire data set. Fig. 5.4 shows the evolution of cost over time for this optimisation procedure. The first 10 runs

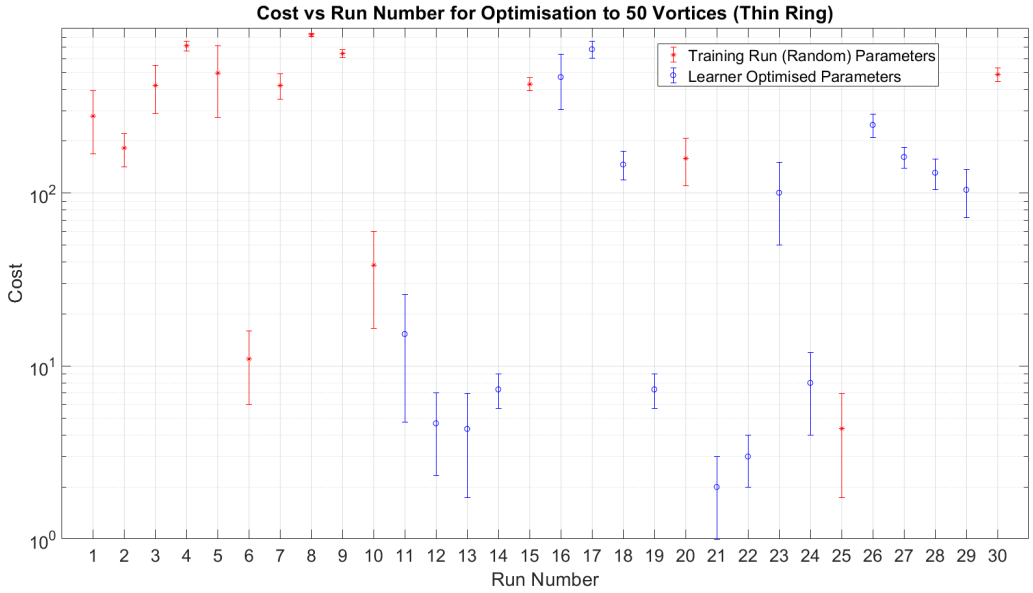

Figure 5.4: Plot of the cost over different runs (parameter sets) in optimising the thin ring shear layer to 50 vortices. Red asterisk points represent randomly generated parameters used for training while blue circles represent inferred parameter sets from the GP regression. Error bars are estimated via the standard error in the cost using three images under each parameter set.

shown are the randomly generated training parameter sets, explaining why the costs and associated errors for these sets vary considerably. Interestingly, error varies depending on the run number and not on the cost of the parameter set. This is most clear by looking at the data point for run 5, which does not have the highest cost for the training set but certainly has the largest error. In contrast, run 8 has the highest cost but one of the lowest error values. Naively, one might conclude that the cost function is not actually classifying parameter sets as desired. This is not the case as the true explanation has to do with the number of vortices generated at each run. Typically, high error runs were associated to images similar to Fig. 5.3 (b) with excessive numbers of random undesirable excitations. These random excitations would result in an extreme variation in the vortex number between the three images taken for the statistical measure of cost. This resulted in large errors associated to the cost.

In contrast, high cost points with low uncertainty were associated to images with very few

vortices. The chosen cost function [Eq. (4.1)] severely punished the large difference between such data sets and the target number of 50 vortices. However, due to the lack of undesirable excitations under such parameters, the images taken were consistent in producing the same vortex numbers at the shear layer. This might have reflected a poor choice of cost were it not for the success of the machine learner optimisation. Regardless, the variation in cost and uncertainty for the initial training set is well understood.

Immediately after the 10 training runs, the learner predicts an optimum parameter set. In Fig. 5.4, there is a clear decrease in the cost under the optimised parameters shown as the blue circles between runs 11-14. The optimised parameters have the lowest cost values (within error) observed in the entire data set. The optimised parameters are given below in Table. 5.1: Between runs $11 - 14$, the predicted best parameters did not vary greatly

Total Stirring Time (ms)	Ramp-In Time (ms)	Ramp-Out Time (ms)	Acceleration Scaling (Dimensionless)	Measured Cost
680.111	109.485	84.284	149.316	20±10

Table 5.1: Table summarising best predicted parameters from M-LOOP where optimisation was performed to a target of 50 vortices using the thin ring configuration. The cost predicted by the learner for this parameter set is also presented along with the true measured cost for comparison.

from those presented in the table. The cost and its associated uncertainty for the optimum parameter set may seem large, but one must recall that Eq. (4.1) defines cost as the square of the error in vortex number. Thus, this optimisation was able to give the vortex shear number of 50 with at most a variation of 7 vortices ($\sim 14\%$ error) as indicated by the cost in Table 5.1. The size of this error can be attributed to the choice of target vortex number and the limitation of the linear acceleration profile for stirring. That is to say, optimising to a target of 50 vortices using linear acceleration stirring might not be achievable experimentally without some excitations. To this end, the machine learning optimisation is considered successful given the constraints placed on the learner.

Subsequent predictions of optimised parameter sets actually began with large costs as is shown in Fig. 5.4 for runs 15-30. The machine learning predicted parameters quickly converge back to the low cost optimum set given in Table. 5.1 after each intermediate training set at runs 15, 20 and 25. There is an emergent pattern in the cost over run number of a spike in cost due to random training followed by a quick decay back to the optimum parameter set with low cost. During the last 5 runs of Fig. 5.4 however, convergence is not observed. This simply suggests that over-training of the learner with runs 15, 20 and 25 begins to adversely influence the inferred parameters. The final optimised parameters were used to produce the image in Fig. 5.5. This image contains the desired 50 vortices and the shear layer is clearly observable. However, some of the 50 total vortices were clearly undesirable excitations and not part of the shear layer. The reason for this has already been discussed as an effect of target number choice and constraints on the learner. Therefore, the learner was actually operating as intended, but the optimisation target was unrealistic.

Such an observation proved useful for subsequent optimisations where lower target numbers of 20 and 30 were instead chosen which removed almost all undesirable excitations from

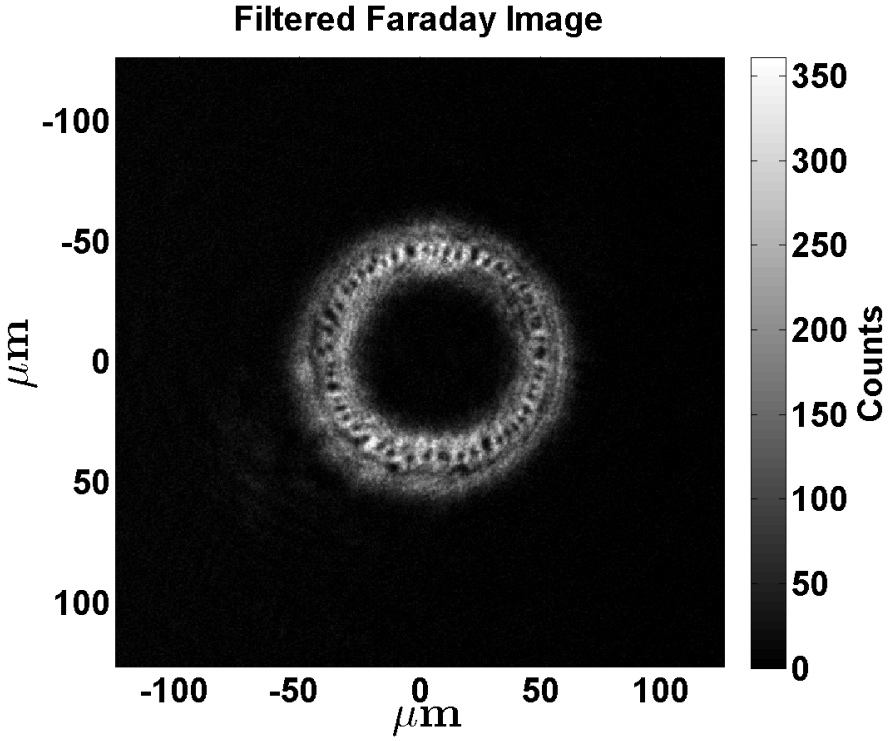

Figure 5.5: 5 ms TOF image taken with no holding time under the predicted best parameters in Table. 5.1. There are a total of exactly 50 vortices in the image but some of these are attributed to excitation which were not completely removed in the optimisation.

the optimisation. Further insight was given into this system by observing vortex dynamics qualitatively as in Fig. 5.6. The images in this figure are taken at various hold times in order to observe the dynamics of the shear layer generated by optimistaion. Here, there is a clear progressive clustering where initially pairs or triplets of vortices are observed at 10 ms but by 100 ms considerably larger clusters have formed through the combination of smaller clusters. This is precisely what is expected qualitatively under a superfluid KH instability induced decay to turbulence. Of course, experimental rigor is required to definitively conclude this with quantitative analysis, but the results under the 50 vortex optimisation are already promising. However, Fig. 5.6 also highlights some issues in the experimental configuration.

Firstly, there is a clear loss of vortices at long timescales. Subsequent experiments were constrained to a maximum of around 500 ms hold time to avoid these losses. This will avoid observing a decrease in cluster number which is actually attributed to vortex losses. Additionally, the vortex detection algorithm has difficulties in detecting vortices when they are as tightly clusters as in Fig. 5.6 (c). In such instances, at most one vortex will be detected when realistically many more are simply in close vicinity. This can be mitigated via the expansion of the ring to allow the clusters to redistribute in more spread patterns allowing for more accurate detection. However, making all these corrections to the configuration required re-optimisation under a larger ring geometry (with dimensions as described in Section 5.1.1).

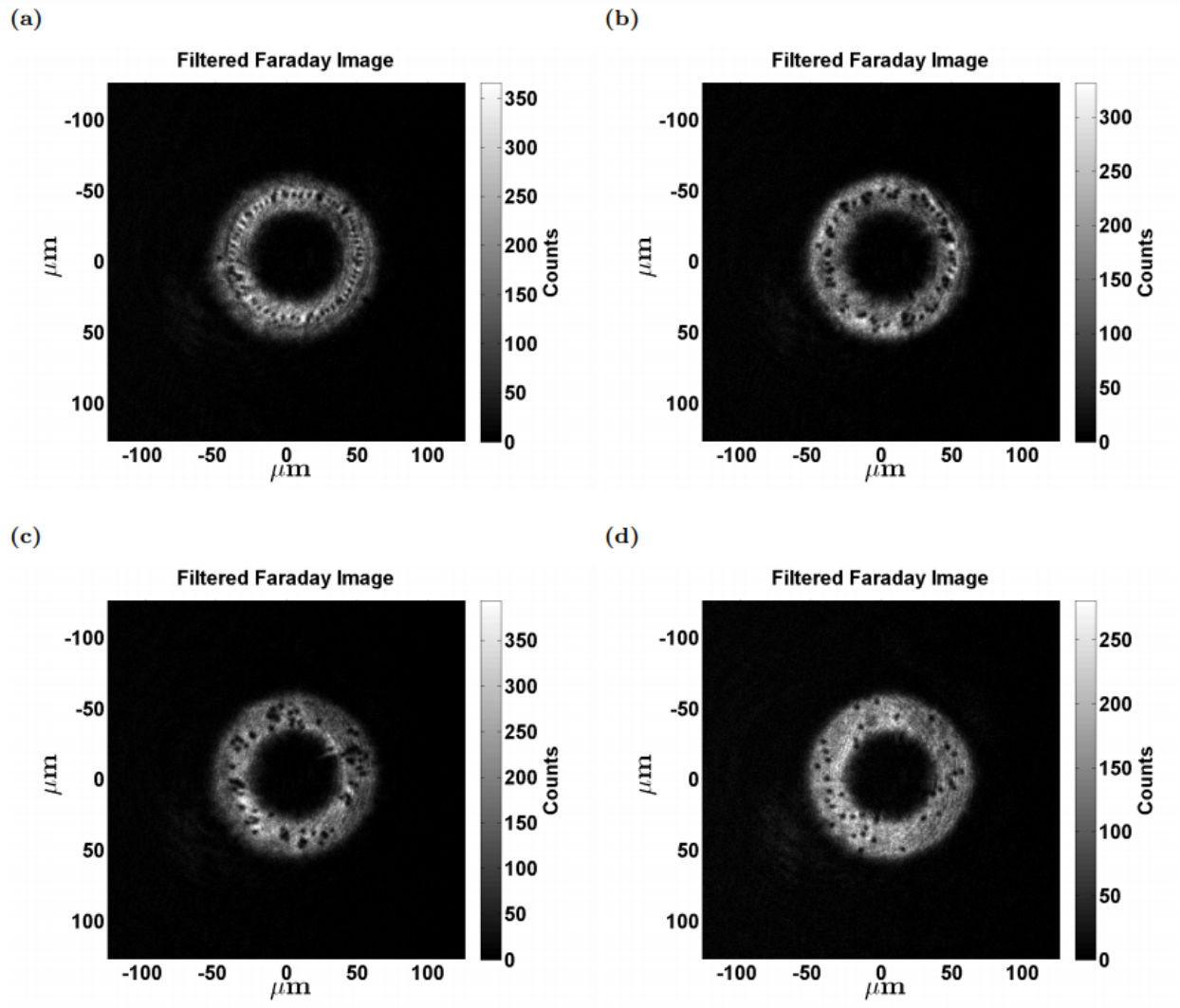

Figure 5.6: Qualitative analysis of vortex dynamics under the optimised parameters of Table. 5.1. (a) 0 ms hold time. (b) 10 ms hold time. (c) 100 ms hold time. (d) 2 s hold time

5.1.3 Large Ring Optimisation

Analysis of the machine learner optimised configurations had provided insight into how machine learning methods should be applied to generate a vortex shear layer. Use of a larger ring meant that dynamics would be more readily observable. This is because not only would vortex loss be reduced for timescales relevant to the experiment but the added space in the larger ring would mean vortex clustering is likely to occur at larger length-scales, which is beneficial for vortex detection accuracy (likelihood of multiple vortex cores overlapping is reduced). Using the larger ring configureation however also required optimisation of the shear layer. Since 50 vortices at the boundary were deemed excessive (optimisation was not possible under linear acceleration), optimisation was instead performed for 20 and 30 target vortices. This choice allowed for the velocity shear generated to be large while giving a

smaller range of initial conditions with which general trends could be discerned. Additionally, comparison between the two cases would allow for analysis about the behaviour of the shear layer as it nears the classical limit of a continuum of point vortices (see Section 3). Due to time constraints only these two vortex shear numbers were chosen but future work would include more initial conditions in order to reinforce general claims about the connections between the quantum and classical regime of turbulence. Re-optimisation to these vortex shear numbers was highly successful solely due to the machine learner.

For the 20 vortex case, the same algorithm as employed in Section 5.1.2 was applied to great effectiveness. Again the cost functions chosen was of the form in Eq. (4.1) here. Fig. 5.7 shows the cost over 10 training runs with the machine learner predicted parameter cost at the 11^{th} run. Again the initial 10 training runs used randomly generated parameters

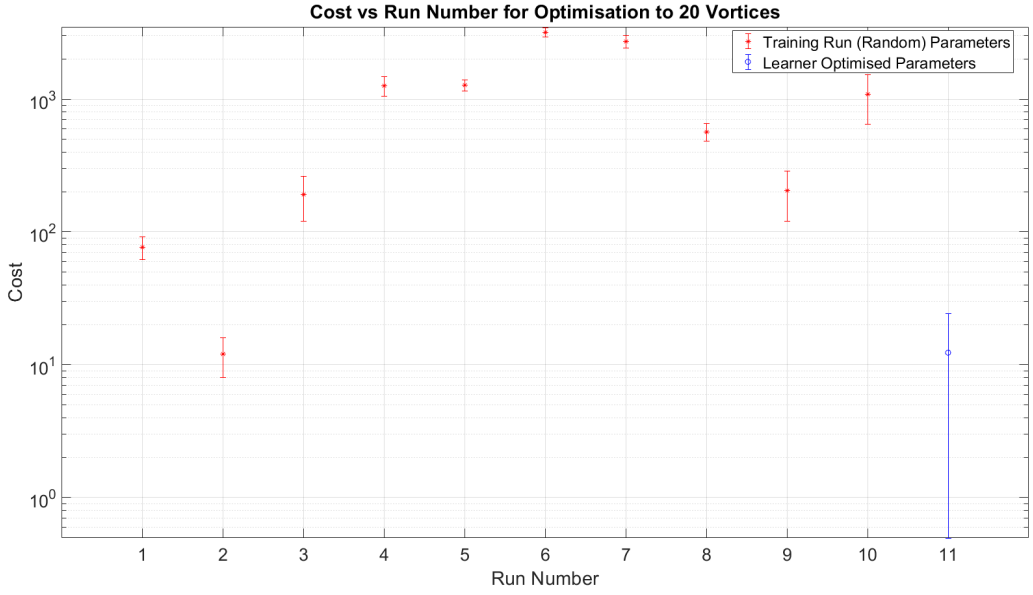

Figure 5.7: Plot of the cost over different runs used in optimising the large ring shear layer to 20 vortices. Red asterisk points represent randomly generated parameters used for training while blue circles represent inferred parameter sets from the GP regression. Error bars as the standard error of cost in three images.

explaining the scattered cost for the first 10 data points in this plot. There is again indication that the cost and error are not directly related since high cost runs do not necessarily have the largest errors. The reasoning for this is as previously discussed; high cost with low uncertainty points typically represent vortex numbers considerably different from the target number but with low excitation numbers while lower costs with large uncertainties represent an excess of undesirable excitations. There is a clear convergence of the data to an optimum parameter set after the 10 training runs which contained the lowest cost (within error). The specific parameters are given in Table. 5.2 below: Comparing these values to the 50 vortex shear number parameters, one sees that the changes to the stirring parameters are difficult to understand intuitively. There is a longer stirring time albeit with a considerably

Total Stirring Time (ms)	Ramp-In Time (ms)	Ramp-Out Time (ms)	Acceleration Scaling (Dimensionless)	Measured Cost
698.210	140.439	164.674	41.906	4±2

Table 5.2: Table summarising best predicted parameters from M-LOOP where optimisation was performed to a target of 20 vortices using the large ring configuration.

smaller acceleration scaling. Thus, the learner predicts that stirring for longer times with slower acceleration is preferred under the choice of cost function. The changes in the ramp times are likely be due to the changes in the geometry of the trap such that a larger ring requires longer ramp times to prevent undesirable excitations. In addition to the changes in parameters, there is a clear decrease in the cost under this optimisation.

At most, the error in the vortex number is 3 under this cost. Thus relative error between the 20 vortex optimisation, $\sim 15\%$, is similar to that of the 50 vortex optimisation $\sim 14\%$. However, absolute error is considerably lower meaning that the vortex shear layer can be consistently created as desired. An image highlighting optimised shear layer containing 20 vortices is shown in Fig. 5.8. Here there are exactly 20 vortices at the shear layer. Unlike

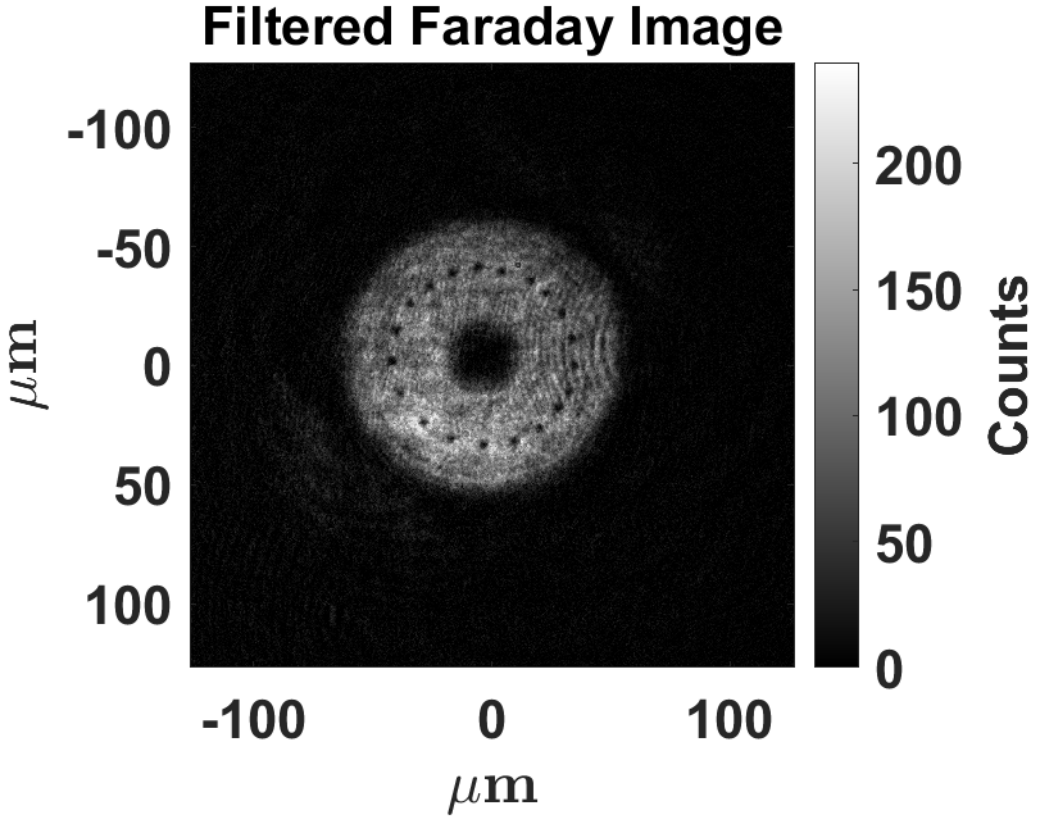

Figure 5.8: 5 ms TOF image of a 20 vortex shear layer produced using stirring parameters optimised by the machine learner. There is a clear lack of undesirable excitations in such systems, so variation in vortex number occurs at the shear layer.

the thin ring optimisation however, the parameter set here did not produce any undesirable

excitations over the 9 images taken at zero holding time meaning that the variation was in the shear vortices. Due to this, this optimisation was deemed successful with potential improvements discussed above for future adaptations. In order to investigate the classical regime of the vortex shear layer, one final optimisation was required to a target of 30 vortices at the superfluid boundary. For the final optimisation, Eq. (4.2) was used for the cost in order to remove the harsh penalty for deviations of few vortices.

The results for the 30 target vortex optimisation are much the same as that of the 20 target number but are still worth discussing for some observations that can be used to critique the methods here and provide further improvements for future work. To begin with, a similar cost over run plot is observed under this final optimisation, which is shown in Fig. 5.9. Note

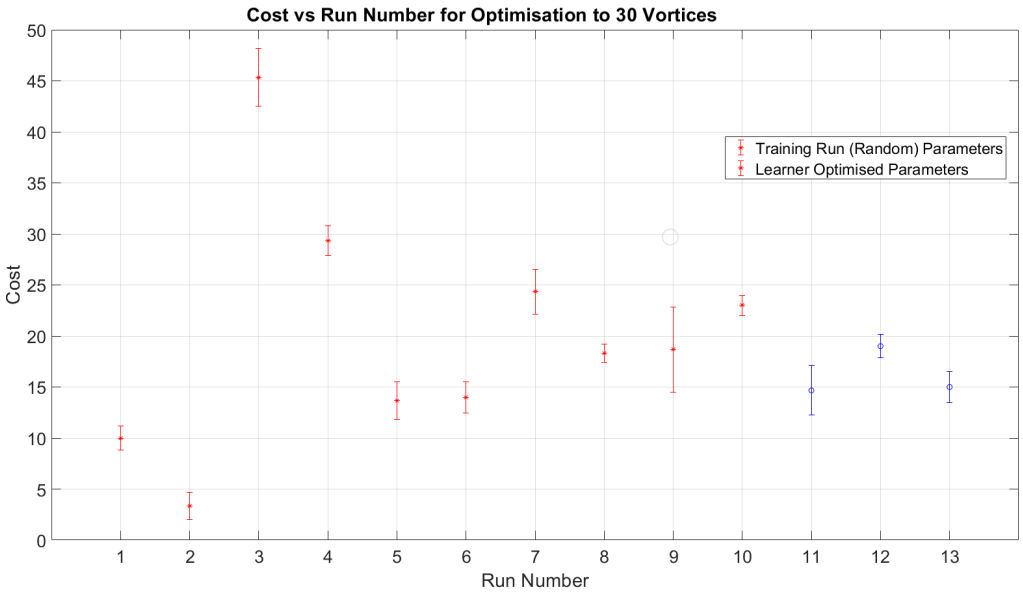

Figure 5.9: Plot of the cost over different runs used in optimising the large ring shear layer to 30 vortices. Red asterisk points represent randomly generated parameters used for training while blue circles represent inferred parameter sets from the GP regression. Error bars as the standard error of cost in three images.

the decreased scale on the cost axis due to the new choice in cost function [Eq. (4.2)]. Here the learner was also run for longer than a single predictive parameter set since convergence to an optimum parameter set (with low cost) was not observed. This is evident in Fig. 5.9 where the learner optimised parameter runs actually have higher cost than that of some random training runs. In this case, the learner simply predicted that the best parameters were those acquired from the brute-force (random) training runs with the lowest cost. This lack of convergence could have arisen from a variety of factors, most likely of which is the choice of parameters. Achieving a specific vortex number at the shear is a complex task and this complexity is made more difficult by restraining the learner to linear acceleration only. The simplistic stirring model had so far served sufficiently in generating the shear layer but optimising to 30 vortices via learning under the set conditions may have proven impossible

for the GP regression.

The use of more complex stirring profiles in future work could greatly improve accuracy and convergence of the learner. One potential improvement would be to fix stirring sequence times but segment the stirring profile into various linear functions. The initial and final values of each segment could be set as the parameters to generate unique stirring profiles allowing the learner to more freely optimise to specific numbers. A similar technique has already been applied by Nakamura *et al.* [52] to generate unique evaporative cooling ramp profiles via GP regression. It is important however to highlight yet again that the success of machine learning in creating a velocity shear in this investigation only requires some manner of optimisation of stirring. It is not relevant whether brute-force or GP regression is used since the focus of the investigation is not on the machine learning methods.

The optimised parameters for the 30 vortex shear number is as given in Table. 5.3: Compared to the 20 vortex optimisation, the stirring time is decreased while the acceleration scaling is increased. Interestingly, the cost of this optimisation is the similar to the 20 vortex optimisation performed in the investigation. At most, the 30 vortex shear layer will vary by just 4 vortices, resulting in a relative error of $\sim 13\%$ making this optimisation the most consistent at generating the desired shear layer. This is suggestive of the applicability use of brute-force methods for shear layer optimisation in general. Under the premise of this investigation, finding some optimised parameter set is considered a success. The optimised parameters yield images as shown in Fig. 5.10, which shows a complete lack of undesirable excitations which was a trend followed by other instances of the same parameter set.

Total Stirring Time (ms)	Ramp-In Time (ms)	Ramp-Out Time (ms)	Acceleration Scaling (Dimensionless)	Measured Cost
562.426	157.207	123.271	46.436	3±1

Table 5.3: Table summarising best predicted parameters from M-LOOP where optimisation was performed to a target of 20 vortices using the large ring configuration.

Therefore, despite some potential for improvement of the machine learning methods applied, optimisation to 20 and 30 vortex shear numbers was achieved. Throughout this discussion, the experimental methods and results were thoroughly critiqued and alternatives for future extensions of this work were considered. There is clear error in the optimisation to a specific target number of vortices but this is to be expected within the experimental framework of the project. The use of machine learning algorithms resulted in a minimisation of this error so that the subsequent experimental results concerning vortex dynamics could be performed in a more controlled environment. In fact, the variation of the vortex number was smaller than predicted by the optimisations here and therefore had little-to-no influence of the dynamics results as is discussed in the next section. Overall, the use of machine learning optimisation was greatly beneficial to the project.

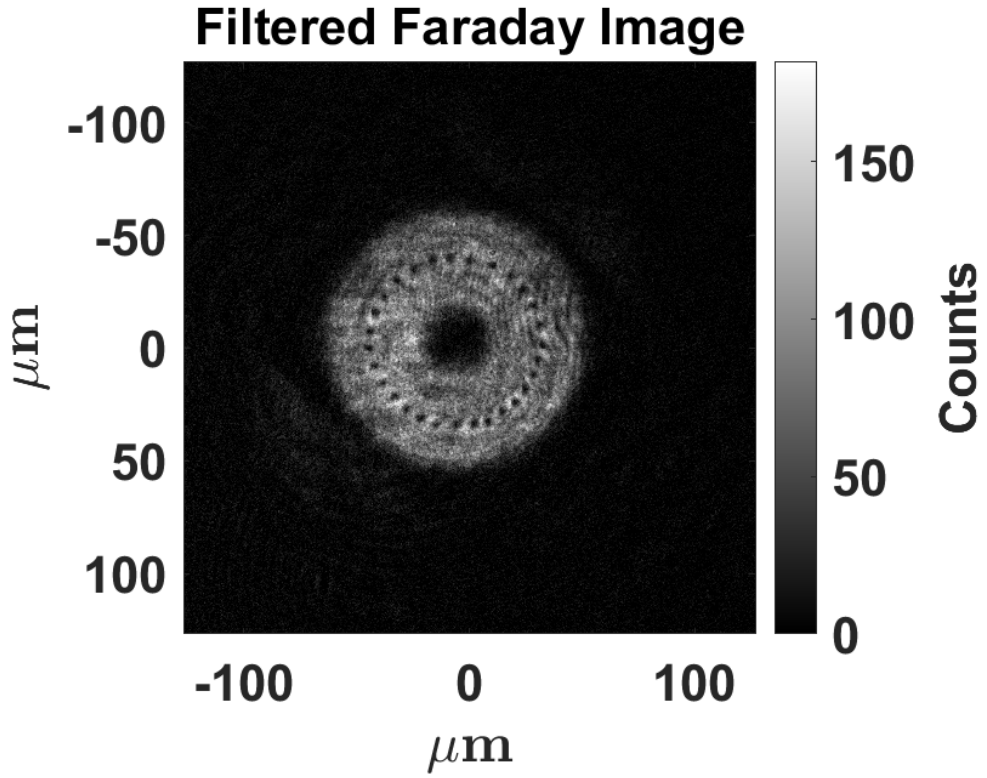

Figure 5.10: 5 ms TOF image of a 30 vortex shear layer produced using stirring parameters optimised by the machine learner. There is a lack of undesirable excitations in the optimised results.

5.2 Observing Shear Layer Decay

With the ability to efficiently and consistently create vortex shear layers in the experiment, it was possible to investigate evidence for the superfluid KH instability induced turbulence in the BEC superfluid systems. The main observations required are as predicted by Baggaley & Parker: initial instability of the vortex sheet, followed by a decay/"roll-up" effect and progressive clustering of the vortices, where the resulting clusters behave as classical patches of vorticity in a turbulent system [5, 6]. Using the optimised shear layers containing 20 and 30 vortices, both qualitative and quantitative evidence was found in the experiment, documenting the first experimental observation of a KH instability in a BEC superfluid. This evidence is shown and analysed here, and suggestions for improvements and further work are made so as to enhance the results found in this investigation. Additionally, the multiple shear layer conditions can also further the analogy between classical and superfluid turbulence induced by the KH instability.

The idea here is that a classical shear layer behaves as a continuum of point vortices, and so the superfluid case can be made to approach the classical limit with more vortices at the shear boundary (see Sections 3.2 & 3.3). Qualitative results for using this concept provided interesting insights into the classical analogs of the clustering behaviour observed. However,

due to some experimental faults in the experimental data, the 30 vortex shear layer quantitative analysis could not be completed and so information about timescales of shear layer decay and further connecting of the classical analogs could not be performed. Additional data collection was not able to be completed due to a failure of the experimental apparatus near the end of the project. Regardless, this section features the most substantial evidence for the observations of a KH instability in the experiment and for comments about the decay to turbulence induced by this instability.

5.2.1 Qualitative Analysis of Vortex Dynamics

The simplest evidence found for KH instability induced turbulence in the experimental BEC superfluids considered here was the qualitative observation of the breakdown of the shear and progressive clustering over time. It is important to quantify this clustering as is discussed in Section 5.2.2, but qualitative results are equally as important for constructing intuition and understanding about a system.

20 Vortex Case

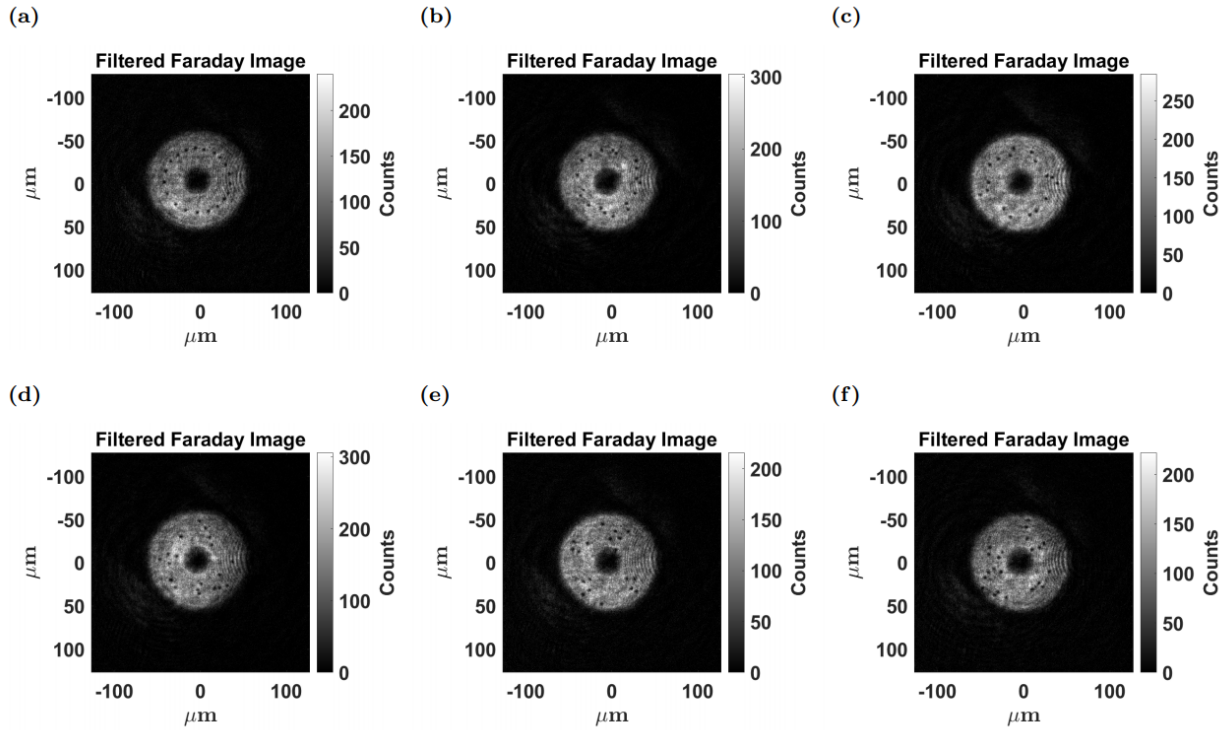

Figure 5.11: Qualitative results for clustering of an initial 20 vortices in the shear layer. Each image shows the vortex positions at various hold time. Note that each image is a different instance of an experimental run and each subfigure here is independent of all others. (a) 0 ms hold time. (b) 90 ms hold time. (c) 190 ms hold time. (d) 320 ms hold time. (e) 400 ms hold time. (f) 460 ms hold time.

Starting with the initial condition of 20 vortices, the clustering is observed over 460 ms of hold times (in 10 ms intervals between different hold times). Fig. 5.11 shows some images from a subset of these hold times which highlight the general trends observed in the vortex dynamics. In this analysis there were 235 images taken (5 images per hold time) and showing all would be impossible. Instead the general behaviour of the vortices over time can be discussed. Initially, the velocity shear layer manifests as the line of vortices. Due to the machine learning optimised stirring parameters, this shear layer consistently contains 20 ± 1 vortices despite the optimisation predicting a larger error in the vortex creation. Regradless, the replicability of the initial vortex shear is highly beneficial to the observation of vortex dynamics. From this initial condition, the shear layer becomes unstable and the vortices are observed to move away from this equilibrium.

The observation of motion away from the shear layer is indicative some instability inherent in the creation of the shear layer. By observing the transition to turbulence under this instability, it can be shown that the system exhibits a KH instability. Specifically, by observing the vortex cluster motion over time, it becomes clear that the analog of the rolling up of the shear layer in BEC superfluids is present. This motion becomes apparent at approximately 90 ms when some vortices seem to pair together in small clusters. This is shown in Fig. 5.11 (b), where the clustering is most obvious on the right side of the superfluid ring which contains multiple pairs of vortices. In this image, the left side of the ring seems to still be at equilibrium despite the hold time. This is simply an artifact of choosing this particular image, since other images at the same hold time showed clustering in different regions of the ring with other sections remaining at equilibrium.

Suggestive of the turbulence introduced through an instability were small deviations of the initial conditions between images results in different outcomes at the same hold times. Despite this chaotic behaviour, each image at or near 90 ms hold time displays the emergence of several two-vortex clusters. After some more holding time has passed, all vortices seem to shift from their initial positions and the emergence of larger clusters of vortices is clear as shown in Fig. 5.11 (c). This image is taken at 190 ms hold time and exhibits not only pairs of vortices near the bottom of the image, but clusters of three vortices on the left and right sides of the ring. It becomes difficult to discern where the equilibrium ring of vortices was initially located due to how much the vortices cluster at long hold times.

It is important to note that qualitative analysis of clustering becomes complicated at this point due to the bias inherent in human classification of clusters. In Fig. 5.11 (c) the top of the image contains a line of vortices which could either be classified as a cluster of four or two clusters of two and such extended cluster objects were observed commonly in the experiment. This simply highlights the need for a quantitative measure of clustering so that there is some standard measure of classifying clusters. Nonetheless, this qualitative analysis has so far been instructive on general trends of the vortex dynamics. Continuing with the discussion, at later times in the experiment, images indicate the expected progressive clustering; lower cluster numbers with increased vortex numbers per cluster. Fig. 5.11 (d-f) show considerable changes in the clusters from all previous hold times. Here there is clear

evidence of the smaller clusters merging as would be expected in freely decaying 2D turbulence within a BEC superfluid.

Over this set of images, the emergence of progressively larger clusters is an important feature, but it is important to again note the bias in human qualitative analysis which complicates commenting on the actual cluster number or size. Even so, starting from 320 ms hold time in Fig. 5.11 (d) one sees multiple instances of clusters comprised of three vortices and even a potential cluster of four vortices on the left side of the ring. Subsequently, at 400 ms hold time there seem to be four clusters in total comprised of up to five vortices, distributed along the axial direction in an almost equally spaced fashion. This is reminiscent of a similar ring trapped BEC GPE simulation by Baggaley & Parker in which the vortex clusters were similarly distributed (see Ref. [5]).

In this experimental system however, imperfections in the trap go beyond simple noise introduced to the system; there are imbalances and shot-to-shot variations which make generalisations difficult. Indeed, the distributions of the clusters only resembled this equally spaced configuration in this single image at 400 ms, suggesting that such a distribution is coincidence rather than a property of the instability. However, the level of variation is again suggestive of turbulent/chaotic behaviour emerging from slightly varying initial conditions. The final set of images were taken at 460 ms, one of which is shown in Fig. 5.11 (f). Here a range of clusters are observable, from pairs to considerably larger vortex numbers. Using vortex detection on this set of images allows for the reconstruction of the approximate stream profile of the superfluid via COMSOL (see Section 4.3).

The outcomes of the COSMOL simulation [44, 45] are shown in Fig. 5.12, which highlights the velocity flow field as arrows and streamlines as contours of the flow field[1]. Additionally, the velocity of the fluid at the positions of the vortices diverges, and so an upper limit is imposed to remove the vortex cores. As a side effect, this upper limit ensures that the vortices are more visible in Fig. 5.12. The colour scale indicates flow speed in the superfluid. Thus, using the tools available in the simulation it becomes possible to observe the decay of the shear layer into turbulence more directly. Under the initial condition of 20 vortices at the shear layer, the flow is clearly laminar as indicated by Fig. 5.12 (a). Here, the line of vortices is at equilibrium and the streamlines are just concentric circles in space. The streamlines near the shear layer do exhibit slightly complex behaviour such as a wrapping effect around the vortex cores as is expected but otherwise the streamlines indicate laminar flow. Aside from the flow velocity near the central repulsive barrier and at the shear layer, the flow velocity magnitude is somewhat uniform or with very gradual variation over space. Between vortices at the shear layer the flow is zero which indicates that all vortices are of

[1]Note that the COMSOL simulation only computes the fluid flow resulting from the presence of vortices. Hence, the background superfluid flow is not present in Fig. 5.12. However, given that the areas of the two channels used in the experiment are approximately equal and that the acceleration of the stirring in each channel is equal in magnitude but opposite in direction, conservation of angular momentum requires no residual rotation of the fluid due to stirring. Under this argument Fig. 5.12 accurately approximates the total flow field of the experimental system. Otherwise, future work from this project will investigate any overall rotation inherent from the stirring.

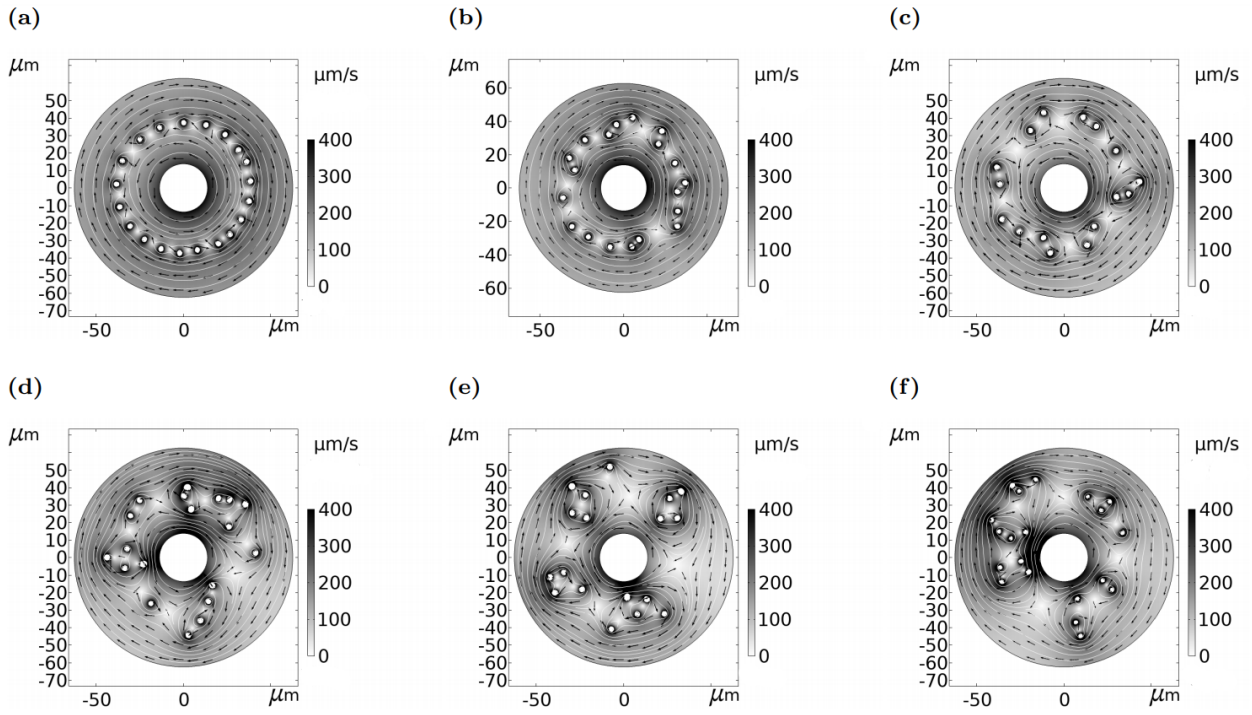

Figure 5.12: Streamlines (white contours) and flow velocities (black arrows) for the experimental images shown in Fig. 5.11. Streamlines were generated in COMSOL, treating the vortices (white points) as point sources of an electric field where the resulting potential approximates the streamfunction of the superfluid. Colour-scale indicates fluid flow speed in μm/s, with darker shaded regions representing faster flow. An upper limit is imposed on the flow velocity scale in order to visualise vortices, where the velocity diverges. (a) 0 ms hold time. (b) 90 ms hold time. (c) 190 ms hold time. (d) 320 ms hold time. (e) 400 ms hold time. (f) 460 ms hold time.

the same charge and hence the induced flow fields at these points cancels.

After 90 ms hold time, in Fig. 5.12 (b), there is a destabilisation of the shear layer which causes the streamlines to exhibit a growth in complex behaviour. Specifically, there are now streamlines surrounding two or more vortices, which constitute a cluster. The decay of the shear layer is evident in the new streamlines, but away from the shear layer there is mostly uniform streamline behaviour indicating laminar flow. Hence, the transition to turbulence has begun but the growth of the perturbations seeded into the shear layer by the KH instability is not sufficient to cause a complete decay into turbulence. Yet, as hold time is increased, there are clear indications of the emergence of turbulence. At 190 ms, in Fig. 5.12 (c), there is a visible clustering effect with streamlines surrounding pairs (and even up to triplets) of vortices. Noticeably, the flow speed is no longer uniform around the ring geometry and instead exhibits patches of higher and lower velocity to the previous hold times. Yet, the flow away from the clusters remains seemingly laminar as indicated by the field arrows maintaining their directionality. Overall, there is a slow transition to turbulence visible which becomes apparent in the subsequent hold times of Fig. 5.12 (d-f).

In these images, there are obvious streamlines surrounding clusters containing four or more vortices and the uniformity of the flow field is all but destroyed. Patches of high/low velocity are seemingly randomly occurring around the system. The flow field arrows no longer indicate two separate, counterflowing streams and now exhibit a highly complex profile. This effect is most obvious at the latest hold time in Fig. 5.12 (f), where the cluster on the left contains a high number of vortices bound by streamlines. In this flow field, there is clear turbulent behaviour near the clusters indicated by the rapidly varying velocity field arrows and streamline contours. Although nearly vanishing, there is however still some laminar flow at the edges of the system indicating that not enough time has passed for a complete decay into turbulence. Despite this insufficient hold time length, the COMSOL simulations show a seemingly classical fluid system as the vortex clusters appear as patches of classical vorticity. The streamline contours around the clusters are typical of classical vortices, similar to the work by McWilliams (see Section 3.3). Thus, the qualitative results not only indicate a decay of the shear layer due to a KH instability but also that the turbulence in the system manifest as vortex clusters begins to exhibit classical behaviour. This is an exciting result as it builds a deeper connection between a classical turbulent fluid system and superfluid turbulence in 2D.

Overall, there lies considerable evidence of the KH instability induced turbulence manifesting in this experimental BEC superfluid. The expected trends predicted by Baggaley & Parker are observable and there is even evidence for the clusters exhibiting turbulent behaviour due to the variation at each hold time. Thus, the qualitative results are clearly indicative of not only a KH instability inherent in the shear layer, but a transition to turbulence in the quantum system via progressive clustering of vortices which behaves analogously to classical vorticity.

30 Vortex Case

These arguments are only further strengthened by identical observations under a 30 vortex shear layer. It becomes important to consider the 30 vortex shear layer case not only for comparison of observations about the shear layer decay but also as an attempt to approach the continuum limit so as to better connect observations in this quantum system to a classical shear layer. The observation of the dynamics of this 30 vortex shear layer was performed over a shorter timescale than the previous results. This was due to the fact that (at least qualtiatively) the clustering effects in this system seemed to occur faster. Overall, 180 images were acquired, with 5 images for each hold time from 0 to 340 ms (spaced apart by 10 ms intervals as before). Select images are shown in Fig. 5.13 which highlight the general trends of the data set. The initial conditions showed slightly more variation in the vortex number over the five images as 30 ± 3 vortices were detected. There was occasionally the presence of a single excitation in these images which highlights the influence of improperly optimised on the shear layer. After only 30 ms holding time, the pairing up effect of the shear layer vortices was observable as in Fig. 5.13 (b). Subsequent holding times actually illustrate the progressive clustering much clearer in this 30 vortex system. After only 110 ms hold time, the vortex clusters were clear and comprised of over 3 vortices on average. The final three images in Fig. 5.13 show the progressive emergence of what seems to be a mega-cluster at 340 ms which was consistently observed over the set of 5 images at this hold time. This

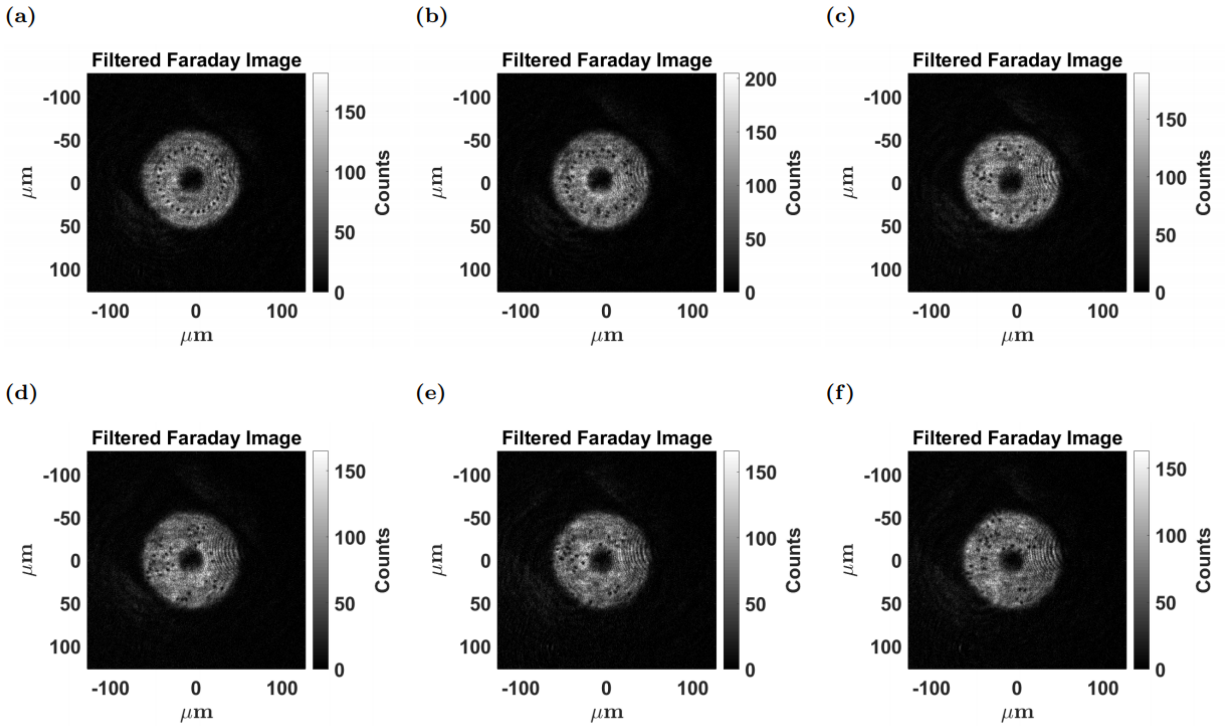

Figure 5.13: Qualitative results for clustering of an initial 30 vortices in the shear layer. Each image shows the vortex positions at various hold time. Note that each image is a different instance of an experimental run and each subfigure here is independent of all others. (a) 0 ms hold time. (b) 30 ms hold time. (c) 110 ms hold time. (d) 240 ms hold time. (e) 310 ms hold time. (f) 340 ms hold time.

mega-cluster is comprised of a large number of vortices and its spatial extent seems to be about a quarter of the ring area visually.

Collectively with the 20 vortex system, these qualitative results are highly suggestive of the KH instability analog being the mechanism through which turbulence is introduced experimentally in this work. Not only do the images of the experimental system exhibit evidence of progressive clustering, but the behaviour of the clusters is reminiscent of classical vortices in turbulent systems due to the combination of shot-to-shot variation and consistent decreasing in cluster number with increasing cluster spatial extent. As discussed in Section 3.2, turbulent systems with vortices exhibit a decay in vortex number and increase in vortex size which is analogous to the cluster number decay and cluster spatial extent observed qualitatively here.

Thus, the 30 vortex shear layer also exhibits a KH instability which causes decay in the layer leading to the emergence of turbulence in the system. Unlike the 20 vortex shear layer case however, the timescale of the shear layer decay is considerably faster in the higher vortex initial condition. Specifically, the emergence of pairs of vortices is observable at around 30 ms in the 30 vortex shear layer results which is considerably faster than pairing observation

at 90 ms in the 20 vortex shear layer. Similar effects are qualitatively observed for various cluster structures and the general trend is that clustering (and therefore the decay to turbulence) occurs considerably faster with a larger velocity shear layer. This is in fact analogous to how slower shear velocities in a classical system lead to the offset of the manifestation of turbulence throughout the system (see Section 3.1). This analogy strengthens the connection between a superfluid system and classical system undergoing a transition to turbulence via a KH instability.

Unfortunately, experimental faults lead to the images for the 30 vortex shear layer to contain considerable noise. This meant that vortex detection was not possible due to low accuracy of the Gaussian blob algorithm in these conditions. Hence, producing a COMSOL simulation of the stream profile for the 30 vortex shear layer was not possible and neither was any quantitative analysis of this system. As mentioned above, additional data collection was not possible due to experimental apparatus failure. Regardless, the 30 vortex shear layer provided excellent support for the claims made about the results of the 20 vortex shear layer above.

However, in order to investigate whether the different vortex shear layers begin to exhibit classical behaviour, quantitative results about the clustering and timescales of shear layer decay are required. At this stage, there is clear evidence of the presence of a KH instability. There is also considerable qualitative evidence for the superfluid KH instability driven turbulence in this experiment, but for better understanding of the mechanisms behind KH instabilities (in both classical and superfluids), a rigorous quantitative analysis is required.

5.2.2 Quantitative Analysis of Vortex Dynamics

Quantitative analysis of vortex cluster dynamics is possible through the DBSCAN sorting algorithm as prescribed in Section 4.3 and through similar methods as highlighted in the pseudo-code in Section A.2. The issue with using DBSCAN and its associate global variables is that clusters of varying density are difficult to sort/detect. The choice of the minimum points for the core of a cluster (see Section 4.3) is fixed to $M = 2$ simply due to the fact that a cluster cannot exist without at least two vortices. The choice for the density scan radius ε is more difficult to discern. Attempts at automating this choice per image were made via a nearest neighbour distance calculation. If vortices were found to be within the mean nearest neighbour distance, they were treated as density-connected points and in this manner the DBSCAN could construct clusters.

This choice of the density might seem logical but in practice this density lead to the divergence between quantitative outcomes with the qualitative observations highlighted in the previous section. Specifically, under this choice of ε, the cluster number over time was seen to begin with one large cluster of vortices since all vortices in the initial ring configuration were treated as being in one large cluster. Due to this, the first data points illustrated a system where the cluster number increased in time. In response to this, the vortex number per cluster started quite large and decreased over time. Even omitting these early hold time

data points, both these aforementioned quantities were observed to plateau despite obvious qualitative evidence of progressive clustering. To remedy this, a simplistic approach was attempted; the choice of ε was fixed for all images. In such a system, the first data points would show incorrect classifications of cluster number and vortex number per cluster, but the goal was to observe improvements in the trends of later hold times.

Fixed ε Cluster Sorting

For the initial condition of 20 vortices, the results of the fixed $\varepsilon = 16$ μm DBSCAN are shown in Fig. 5.14 and Fig. 5.15 which show the cluster number over time and the mean vortex number per cluster respectively. It should be noted that each data point is the mean measure of the 5 images taken at the associated hold time. The uncertainty is estimated via the standard error measurement between the 5 images. The choice of ε was made via basic observation of cluster spatial extent being on the order 16 μm for late hold times. As expected, the earlier data points are treated as containing very few but large clusters due to the vortices near uniform spatial distribution. After 150 ms, the trends in cluster number and vortex number per cluster begin to align with that of the qualitative results. The fact that this general trend arises is promising. It is important to note also that this trend is not manufactured via fixing ε. There is substantial evidence for the decreasing cluster number over time in a qualitative sense and therefore this correction to the clustering algorithm only aims to fix errors in DBSCAN and not impose bias on the data set.

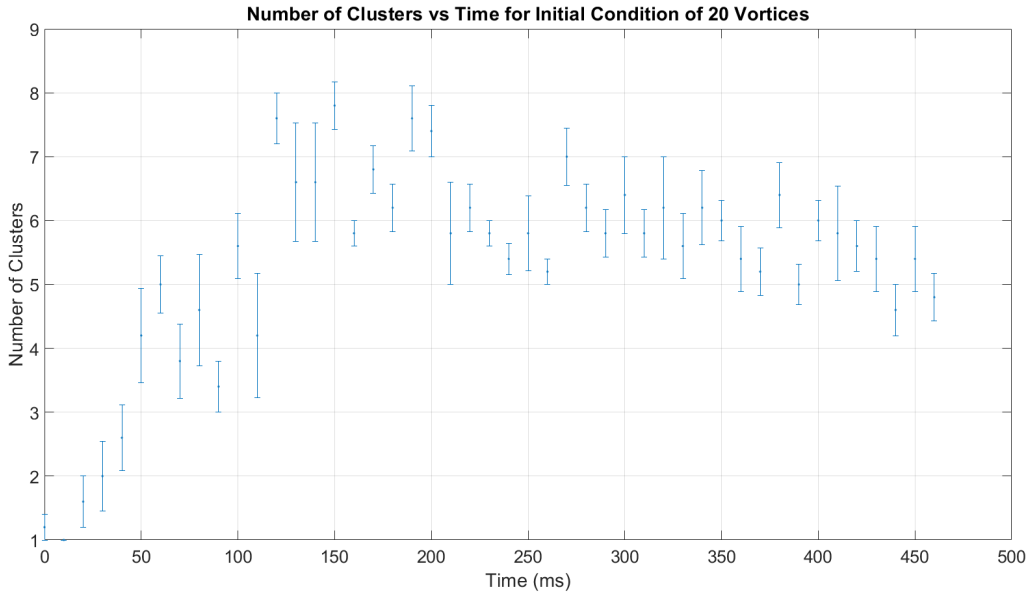

Figure 5.14: Plot illustrating the decay of cluster numbers over time with an initial vortex shear number of 20, according to fixed $\varepsilon = 16$ μm clustering.

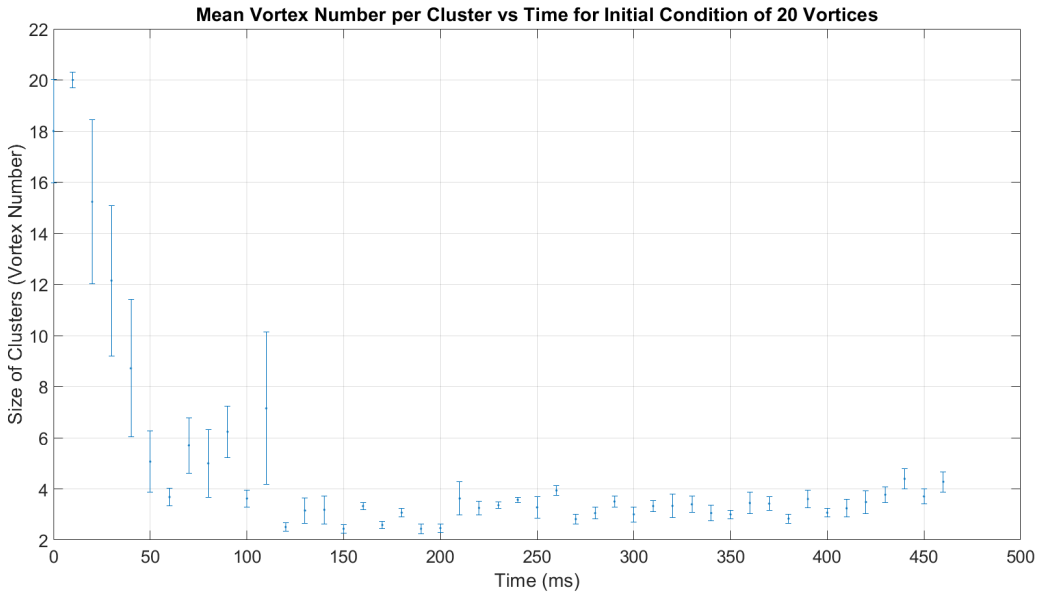

Figure 5.15: Mean vortex number per cluster over time with an initial vortex shear number of 20, according to fixed $\varepsilon = 16$ μm clustering.

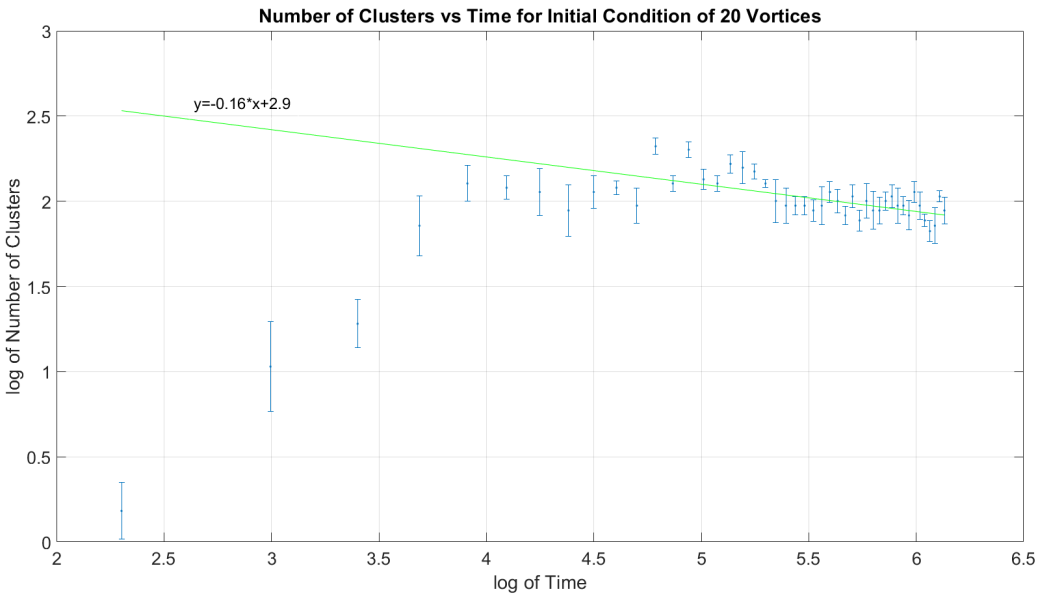

Figure 5.16: Log-log plot of cluster number over time with an initial vortex shear number of 20, according to fixed $\varepsilon = 16$ μm clustering. The line of best fit is performed using data points after the approximate turning point at 150 ms. The linear fit is presented where the slope represents the power-law scaling for comparison to the classical system of vortices. For the fit, y represents the logarithm of the cluster number and x represents the logarithm of the time.

Similar comments can be made on Fig. 5.15 which still exhibits the initial decay of mean vortex number per cluster up to a turning point after which a monotone increase over time is observed. Further evidence of vortex number per cluster increasing over time are provided by the maximum and median vortex number per cluster shown in Fig. A.2 and Fig. A.3 in Appendix A.3. A promising feature of all these fixed ε clustering plots is that the error bars for the early hold times are particularly large in comparison to late hold times when the ε choice is better suited. This illustrates that error in the ε has manifest in the results.

Overall, after 150 ms the expected trends for progressive clustering are evident in these results. One note to make about this however is that the rate of decay of cluster number or growth of vortex number per cluster is quite small. That is to say, the power-law scaling of time for these trends is close to zero. This is most evident in the slope of the log-log plot of the cluster number over time, shown in Fig. 5.16. The slope of this data (considering only points after 150 ms) is seen to be negative (as expected due to the decay) but with magnitude 0.16. This is considerably outside the range of -0.7 to -1 as predicted by McWilliams for classical vortices (which the clusters should mimic in a turbulent system). This divergence is yet another effect of the fixed ε choice made, indicating that alternative cluster analysis was necessary. Unfortunately, due to the lack of prior knowledge about how many clusters any particular image contained, use of algorithms alternative to DBSCAN was not possible given the time-frame of the experiment. Methods such as Gaussian mixture models [53] and simpler k-means methods [54] were attempted to no success.

Manual Cluster Sorting

Reluctantly, manual choice of the ε value for each image had to instead be employed. This was understood to introduce bias into the quantitative results where human preconceptions about the classification of clusters could introduce error in the analysis. In an abstract sense, such a bias is inherent in any cluster sorting algorithm, where a given definition of a cluster is enforced through some mathematical model. Therefore, the use of DBSCAN with manual human input of ε is not problematic. The algorithm simply acts to remove some bias or error in the qualitative analysis via mathematical rigor and image recognition.

Given more time however, the investigation would have applied enhanced DBSCAN algorithms such as AA-DBSCAN which automates the choice for ε for each cluster based on cluster density through the use of grid based cluster sorting [10]. Yet even without the implementation of these enhanced algorithms, the manual clustering method reveals promising trends in the detection of transitions to turbulence via KH instabilties. Fig. 5.17 and Fig. 5.18 show the cluster number and mean vortex number per cluster over time with the manual clustering method. Here, the results are exactly as one might expect but whether this is the artifact of bias and preconceptions about the system or truly reflective of the clustering effects in the experiment cannot be determined. Fig. 5.17 shows an asymptotically, monotone decreasing trend in the cluster number over time. This result shows a clear decay of the vortex shear layer over resulting in the introduction of turbulence to the system. Also as expected, Fig. 5.18 shows the mean vortex number per cluster exhibiting a similar monotone increasing trend.

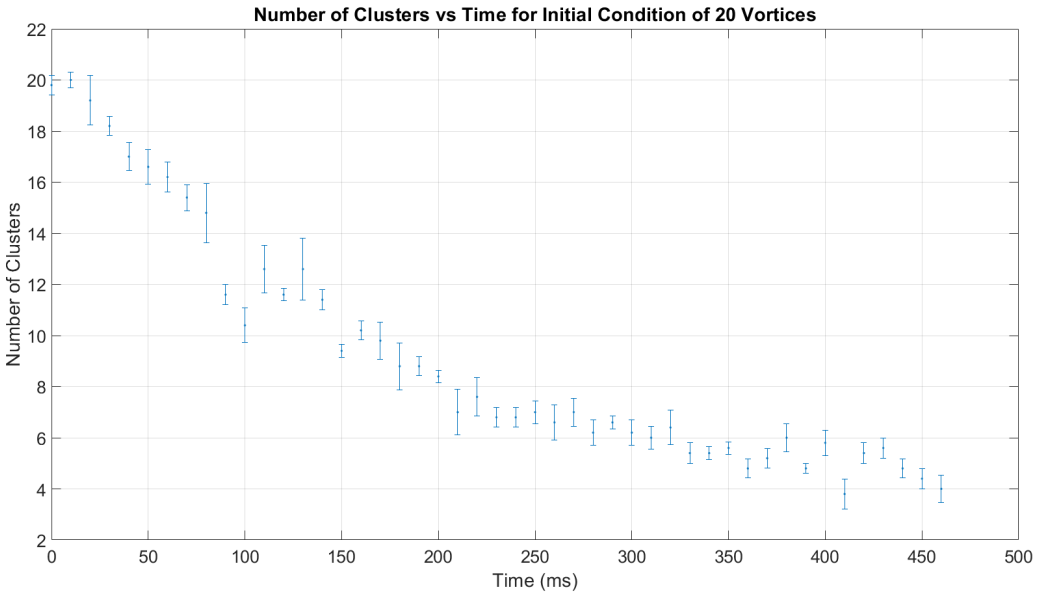

Figure 5.17: Plot illustrating the decay of cluster numbers over time with an initial vortex shear number of 20, according to manual ε clustering.

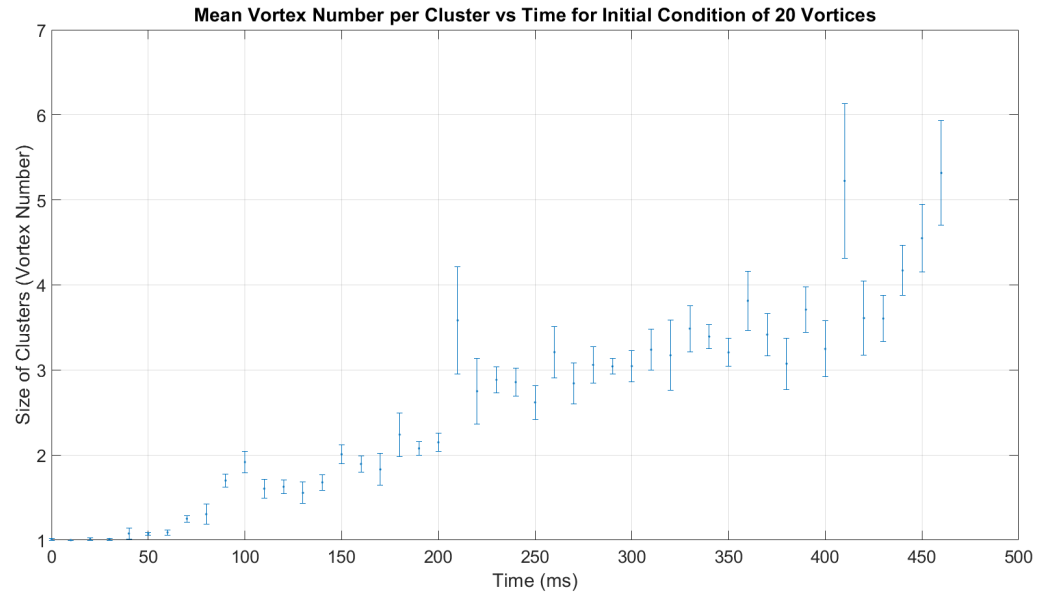

Figure 5.18: Mean vortex number per cluster over time with an initial vortex shear number of 20, according to manual ε clustering.

Further results for the maximum and median vortex number per cluster are shown in Fig. A.4 and Fig. A.5 in Section A.3. The trend in the mean vortex number per cluster however seems to follow steps instead of a strictly increasing function of time. This result is similar to the cluster size growth predicted in Baggaley & Parker which also exhibited step behaviour [5]. That is to say, there are segments of the decay to turbulence where the structure of the vortices seems to remain fixed before further decay occurs. Small clusters of two vortices form on the order of 100 ms, and these pairs of vortices dominate the cluster structure until a sudden step up is observed at just over 200 ms. At this point three vortex clusters are dominant until a large step is observed near the end of the data. seemingly the clustering rate is fast for smaller vortex numbers per cluster. This suggests that longer timescales are needed to observe the full decay of the shear layer. In addition, this step like behaviour mimics the progressive coalescence of classical vortices as discussed in Section 3.1. Thus, beyond just providing evidence for the existence of a KH instability in the system, the quantitative analysis here also illustrates some key connections between clusters of quantum vortices and classical patches of vorticity in turbulent systems.

Some interesting notes can also be made about the uncertainties in all these plots. Firstly, the uncertainties on the cluster number over time do not vary greatly between data points and are of low magnitude. This suggests that the number of clusters observed in each set of 5 images for different hold times were quite consistent. On the other hand, the error in the mean vortex number per cluster grows continuously throughout the different hold times. This reflects a trend in the data where the cluster numbers overall remain consistent but there is a great divergence in the constitution of the clusters as time passes. Overall, this means macroscopic structure of the clusters is preserved while the microscopic structure is strongly dependent on initial conditions seeded by the KH instability. This decay into varying microscopic structure is actually suggestive of turbulence in the system. Thus, there is a further evidence for the superfluid KH instability induced turbulence in the experiment.

Connection to Classical Turbulence

Further support for the claim that the clusters of vortices behave as classical patches of vorticity can be found from the quantitative analysis of the 20 vortex shear layer, via the derivation of a power-law for cluster number decay. Attempting to derive this power-law scaling under the manual clustering method proves more successful here and is shown in Fig 5.19.

Firstly, the fit is not restricted to a subset of the data, and so it is a stronger representation of the entire data set. Additionally, the slope of fit which represents the power-law scaling is comparable to the classical turbulent system of vortices by McWilliams. This shows evidence for the fact that clusters of quantum vortices whose dynamics are driven by a KH instability behave as classical vortices in a turbulent system. This evidence acts to enhance the claims of the qualitative results and shows a deeper connection between the superfluid KH instability and its classical counterpart. It would be ideal to further the support found here by considering the 30 initial vortices. Unfortunately, the vortex detection algorithm cannot to accurately detect vortices and their positions in the data set for the 30 vortex instance. This outcome is unfortunate but the analysis for the 20 vortex data set

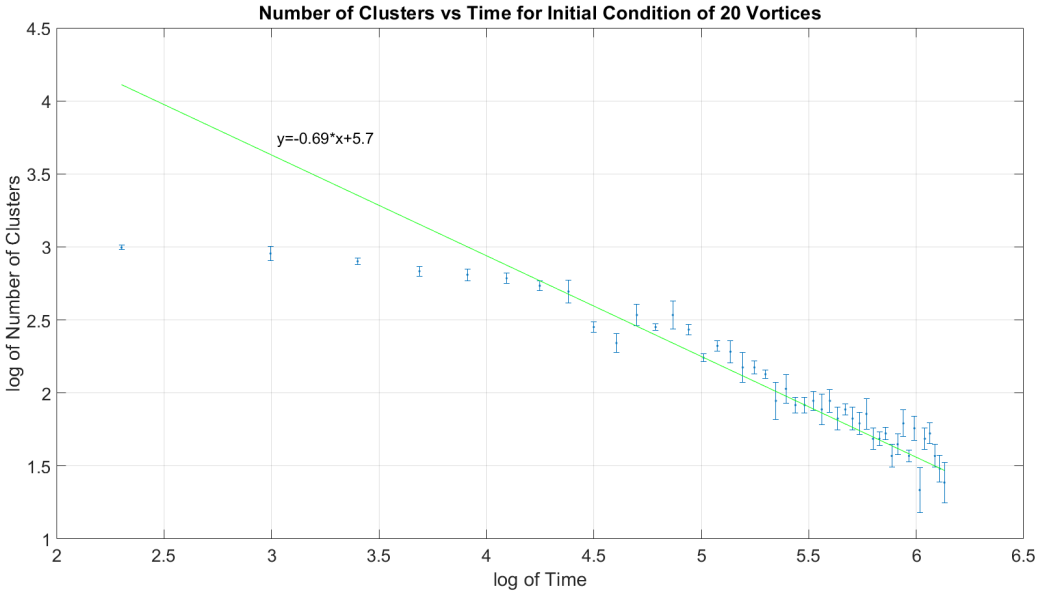

Figure 5.19: Log-log plot of cluster number over time with an initial vortex shear number of 20, according to manual ε clustering. The line of best fit is performed using all data points. The linear fit is presented where the slope represents the power-law scaling for comparison to the classical system of vortices. For the fit, y represents the logarithm of the cluster number and x represents the logarithm of the time.

already illustrates promising evidence for the observation of transitions to turbulence in the BEC superfluid approaching the classical shear layer limit.

Already, this section of the results has discussed on improvements which could be made so that the analysis here can be enhanced in future work. Another addition would be the retaking of the 30 vortex data set along with other initial conditions. These additional results would allow for that claims made in quantitative analysis to be strongly supported with more data (or disputed by potential inconsistencies in data). Multiple data sets would also allow for the determination of whether power-laws are dependent on the initial vortex number which itself is directly related to the shear velocity values. This would allow for more comparisons between transitions to turbulence in superfluid systems and classical fluids.

5.2.3 Final Remarks on the Vortex Dynamics Results

In summary, quantitative analysis of cluster dynamics was only possible for the 20 vortex initial conditions. Successful cluster sorting was observed under the DBSCAN but careful choices of ε were required to observe quantitative evidence for transitions to turbulence driven via the KH instability. Some issues which arose in the experimental results were discussed and suggestions for improvements made but overall the combination of qualitative and quantitative results indicate clearly a transition to turbulence in the BEC superfluid which is seeded by the KH instability from the velocity shear layer. The significance of such

a conclusion is profound since it marks the first experimental observation of a pure BEC superfluid undergoing transitions to turbulence via the KH instability. The outcomes of the investigation may be simple but they lay the groundwork for extensions and future work on superfluid instabilities in BEC systems.

One aspect of the results that is of particular interest for future work based on this project are the stream profiles generated via COMSOL. Since these simulations allow for the generation of a continuous flow field, it is possible to repeat the contour analysis from McWilliams about the decay rate of classical vortices (clusters of quantum vortices) and the growth rate of the classical vortex sizes. By repeating COMSOL simulations for a range of initial conditions it would be possible to track the emergence and dynamics of vortex clusters and their surrounding streamlines to see how the results quantitatively compare to the classical results from McWilliams. This analysis would greatly strengthen claims made about the connections between quantum and classical turbulence. Unfortunately, this combination of experimental and computational techniques could not be implemented under the time frame of the project presented in this thesis but it presents an opportunity and motivated interest for future work based on this project.

6

Outlook and Conclusion

Overall, this project aimed to investigate the existence of KH instabilities and the properties of the subsequent transitions to turbulence in a single-component, experimental BEC superfluid. The phenomena of instabilities and turbulence are key aspects of deriving connections between superfluids and their classical counterparts. The prior literature discussed in earlier sections of the thesis provided promising background for the success of this endeavour and even methods through which stronger connections between classical and superfluid turbulence could be made. The resulting analysis certainly supports the claim that KH instabilities were observed in the experiment via the conditions predicted by Baggaley & Parker, marking the first experimental observation of such instabilities in a pure BEC system (to our best knowledge). Additionally, computational techniques were employed to reconstruct the flow fields of the experimental BEC systems. The outcomes of these simulations was that evidence of progressive clustering was more clearly evident and more importantly that the decay to turbulence in the experiment mimicked closely a classical turbulence system, where the clusters of quantum vortices behaved as patches of classical vorticity. Thus the project succeeded not only in observing experimental transitions to turbulence induced by KH instabilities, but was also able to deepen the connection between classical and quantum turbulence through its results.

Despite this success, some of the results and analysis could be improved. The first of which is the retaking of cluster dynamics data for 30 vortices along with new dynamics data at various other initial conditions. This new data combined with alternative cluster sorting methods such as the aforementioned AA-DBSCAN would significantly improve the claims made in the investigation. The new results would also allow investigation of the decay of the shear layer as the classical limit (continuum of vortices in the layer) is approached. Removal of human bias in the cluster sorting is necessary to perform a standardised classification of

turbulent phenomena in the BEC system. Additionally, a precise measure of vortex cluster spatial extent would allow for further analogies to be drawn between the experimental results and prior work in both superfluids (Baggaley & Parker) and classical vortex systems (McWilliams). Another minor improvement would be a more focused machine learning optimisation protocol for future work, including larger amounts of training runs, use of multiple machine learning algorithms (i.e. neural-networks for comparison to GP regression) and implementation of more complex parameters to allow for better machine control over the experiment. Finally, the implementation of the COMSOL stream profile simulations as quantitative comparisons of superfluid behaviour to classical behaviour would serve to build understanding between quantum vortex clusters and classical vortices in turbulent systems. These improvements should be thought of not as failures of the project but as an opportunity for improvement in future work.

Future work based on the investigation here could go beyond an improvement of the results. Some potential areas of significance are investigations into multi-component BEC superfluid instabilities. Using more species of superfluids would allow for the verification of results found here and potential extension into other instabilities where density variations can drive transitions to turbulence (i.e. buoyancy-driven instabilities). Other potential future work could include a focused study on machine learning optimisation of the velocity shear layer. Another suggestion for future work include extensions into 3D system instabilities, which would be ambitious but could hold interesting results that furthers understanding of turbulence in general. Thus, this project establishes the groundwork for exciting future work that would greatly enhance understanding of superfluidity, turbulence and manifestations of classical fluid phenomena in quantum systems.

A

Appendix

A.1 Rubidium 87 Hyperfine Structure

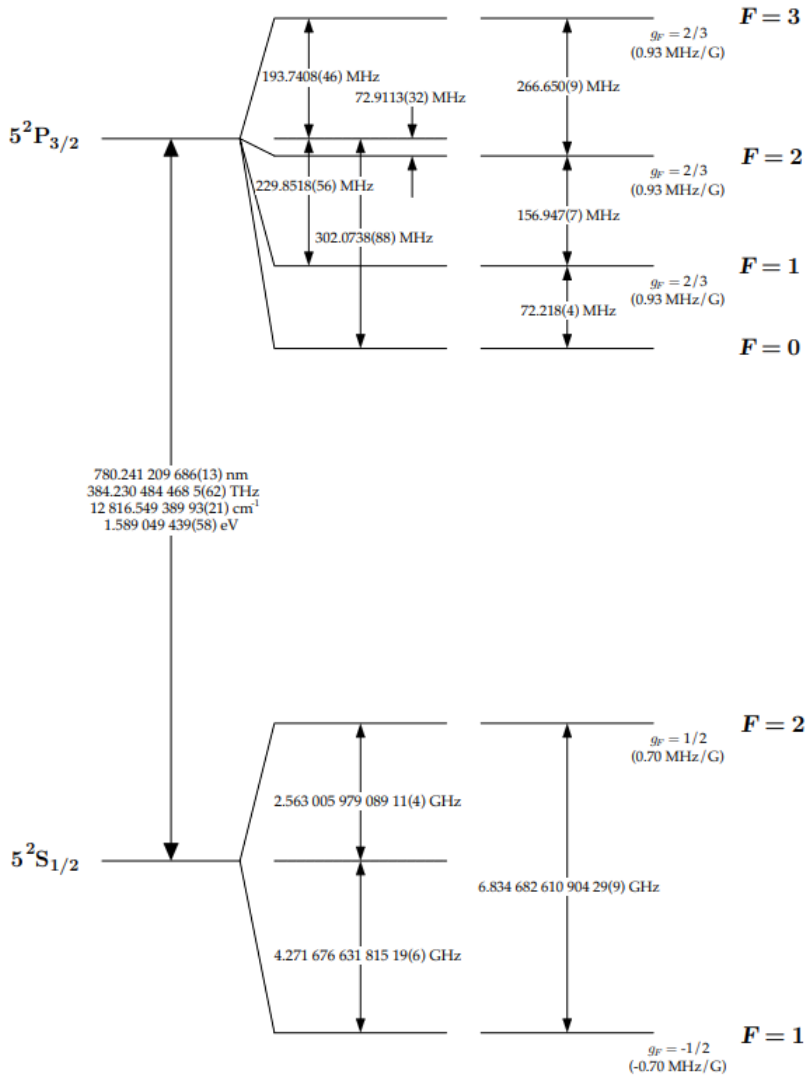

FIGURE A.1: ^{87}Rb Hyperfine structure at the D2 transition level. Left hand lines represent the energy structure without the Zeeman effect while the right hand show the hyperfine splitting under a magnetic field. The middle structure shows further frequency splitting in the hyperfine structure which is not relevant for this experiment. Figure taken from Ref. [11].

A.2 MATLAB Cluster Analysis Pseudo-Code

```
%Use the vortex detection algorithm to find vortex positions
%as a matrix whose columns are the (x,y) components
[positions,...]=VortexDetection(...)

%Extract (x,y) coordinates as vectors from the positions
x=positions(:,1);
y=positions(:,2);


%collect (x,y) positions into single z=x+iy
z=x+sqrt(-1)*y;

%Find the difference is vortex positions
for i=1:length(z)
    for j=1:length(z)
            R(i,j)=abs(z(i)-z(j));
    end
end


%compute nearest neighbour distances for each vortex
for i=1:length(z)
     nearestNeighbour(i)=min(setdiff(R(i,:),R(i,i)));
end


%Define epsilon as a function of the nearest neighbour distances
epsilon=f(nearestNeighbour);


%apply the DBSCAN algorithm for epsilon as defined above and M=2
clusterClassification=dbscan(positions,epsilon,2);


%Count the number of clusters and number of vortices in each
%cluster treating noise points as clusters of single vortices
if max(clusterClassification)~=-1
    %cluster number
    clusterNum=max(clusterClassification)+...
               sum(clusterClassification==-1);
    %vortex number per cluster
    for i=1:max(clusterClassification)
```

```
43          sizeClust(i)=sum(clusterClassification==i);
44      end
45      if ismember(-1,clusterClassification)
46          for ii=1:sum(clusterClassification==-1)
47              sizeClust(i+ii)=1;
48          end
49      end
50  else
51      clusterNum=sum(clusterClassification==-1);
52      sizeClust=1;
53  end
54
55  %mean, median and maximum vortex number per cluster
56  meanClustSize=mean(sizeClust(sizeClust~=0));
57  medianClustSize=median(sizeClust(sizeClust~=0));
58  maxClustSize=max(sizeClust(sizeClust~=0));
```

A.3 Quantitative Data for Clustering of 20 Vortices at the Shear Layer

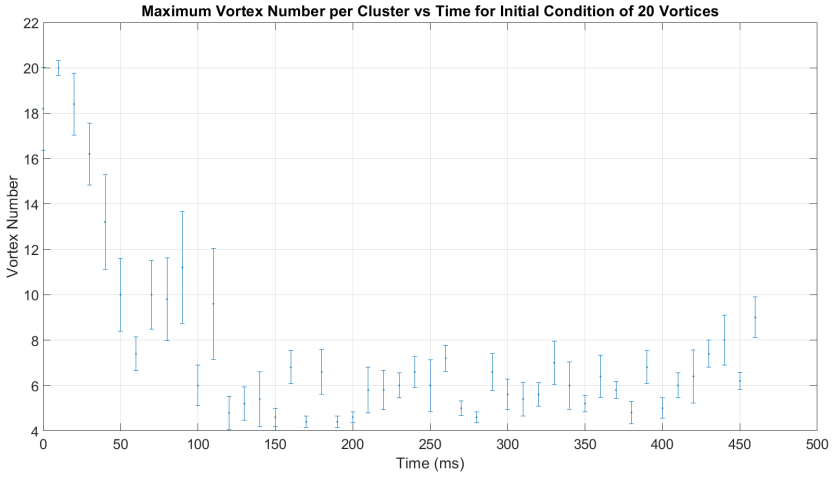

Figure A.2: Maximum vortex number per cluster over time with an initial vortex shear number of 20, according to fixed $\varepsilon = 16$ clustering.

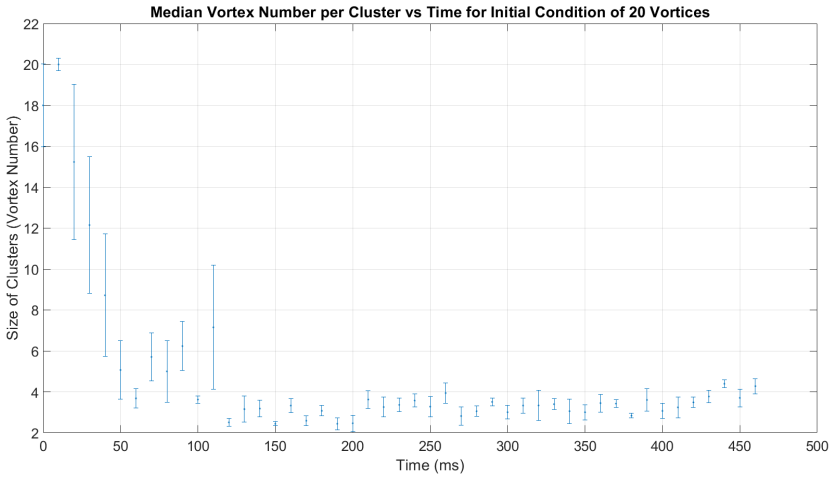

Figure A.3: Median vortex number per cluster over time with an initial vortex shear number of 20, according to fixed $\varepsilon = 16$ clustering.

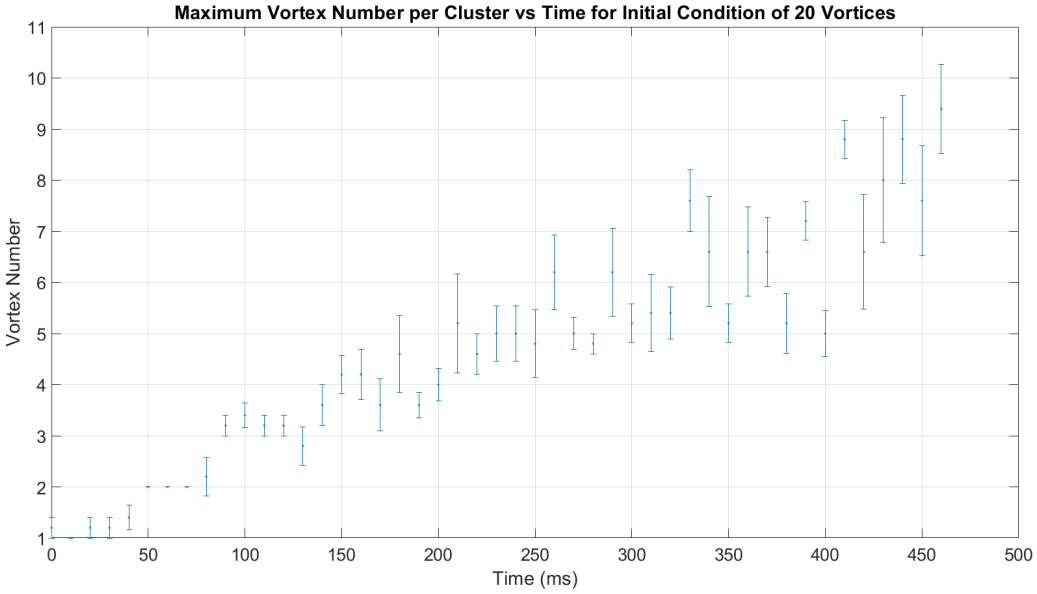

FIGURE A.4: Maximum vortex number per cluster over time with an initial vortex shear number of 20, according to manual ε clustering.

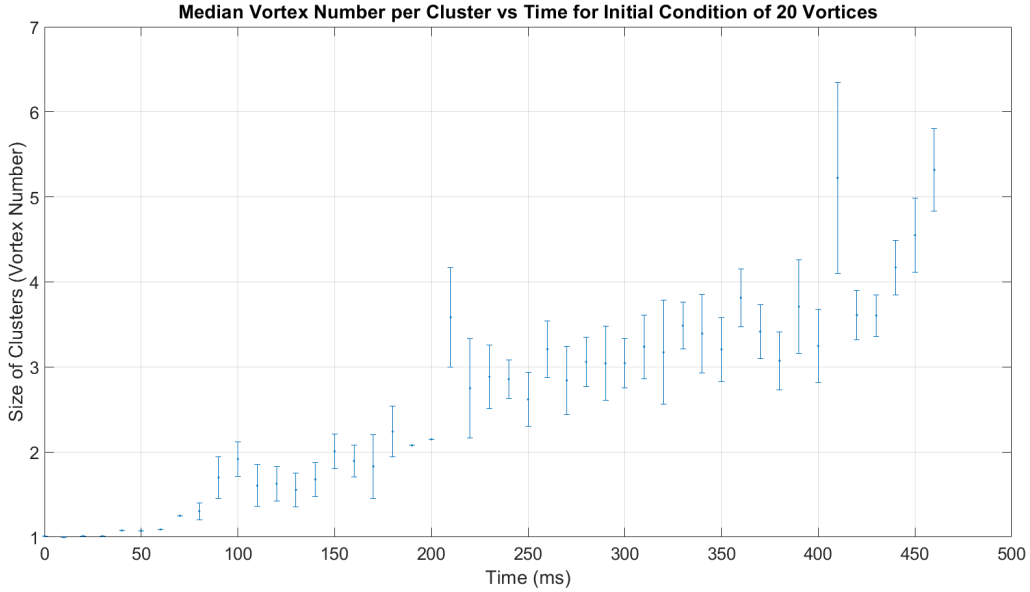

FIGURE A.5: Median vortex number per cluster over time with an initial vortex shear number of 20, according to manual ε clustering.

References

[1] H. Kull. *Theory of the Rayleigh-Taylor instability.* Physics Reports **206**(5), 197 (1991).

[2] M. S. Roberts. *Experiments and Simulations on the Incompressible, Rayleigh-Taylor Instability with Small Wavelength Initial Perturbations* (2012).

[3] P. Philippi, K. Mattila, L. Hegele, and D. Siebert. *Kinetic Projection and Stability in Lattice - Boltzmann Schemes* (2015).

[4] O. San and R. Maulik. *Stratified Kelvin-Helmholtz turbulence of compressible shear flows.* Nonlinear Processes in Geophysics **25**(2), 457 (2018).

[5] A. W. Baggaley and N. G. Parker. *Kelvin-Helmholtz instability in a single-component atomic superfluid.* Physical Review A **97**(5) (2018).

[6] J. C. Mcwilliams. *The vortices of two-dimensional turbulence.* Journal of fluid mechanics **219**(1), 361 (1990).

[7] G. Gauthier. *Transport and turbulence in quasi-uniform and versatile Bose-Einstein condensates.* Ph.D. thesis, School of Mathematics and Physics (2019).

[8] C. Bauckhage and R. Sifa. *k-Maxoids Clustering.* In *LWA*, pp. 133–144 (2015).

[9] M. Ester. *Density-based Clustering*, pp. 795–799 (Springer US, Boston, MA, 2009).

[10] J.-H. Kim, J.-H. Choi, K.-H. Yoo, and A. Nasridinov. *AA-DBSCAN: an approximate adaptive DBSCAN for finding clusters with varying densities.* The Journal of Supercomputing **75**(1), 142 (2019).

[11] D. Steck. *Rubidium 87 D Line Data* (2003).

[12] C. Barenghi. *Introduction to Superfluid Vortices and Turbulence.* Lecture Notes in Physics **571** (2001).

[13] C. Barenghi, V. L'Vov, and P.-E. Roche. *Experimental, numerical and analytical velocity spectra in turbulent quantum fluid.* Proceedings of the National Academy of Sciences of the United States of America **111**(Suppl. 1), 4683 (2014).

[14] C. Ryu, P. W. Blackburn, A. A. Blinova, and M. G. Boshier. *Experimental Realization of Josephson Junctions for an atom SQUID.* Physical Review Letters **111**(20) (2013).

[15] A. Rakonjac, A. L. Marchant, T. P. Billam, J. L. Helm, M. M. H. Yu, S. A. Gardiner, and S. L. Cornish. *Measuring the disorder of vortex lattices in a Bose-Einstein condensate.* Physical Review A **93**(1) (2016).

[16] P. Mason and N. G. Berloff. *Dynamics of quantum vortices in a toroidal trap.* Physical Review A **79**(4) (2009).

[17] S. Kling and A. Pelster. *Thermodynamical Properties of a Rotating Ideal Bose Gas.* Physical Review A **76**, 23609 (2006).

[18] C. W. Gardiner, J. R. Anglin, and T. I. A. Fudge. *The stochastic Gross-Pitaevskii equation.* Journal of Physics B: Atomic, Molecular and Optical Physics **35**(6), 1555 (2002).

[19] C. J. Pethick and H. Smith. *Bose–Einstein Condensation in Dilute Gases* (Cambridge University Press, 2008), 2 ed.

[20] R. Srinivasan. *Vortices in Bose-Einstein condensates: A review of the experimental results.* Pramana **66**, 3 (2006).

[21] S. McArdle, T. Jones, S. Endo, Y. Li, S. C. Benjamin, and X. Yuan. *Variational ansatz-based quantum simulation of imaginary time evolution.* npj Quantum Information **5**(1) (2019).

[22] N. March. *The Thomas-Fermi approximation in quantum mechanics.* Advances in Physics **6**(21), 1 (1957).

[23] G. Gauthier, I. Lenton, N. M. Parry, M. Baker, M. J. Davis, H. Rubinsztein-Dunlop, and T. W. Neely. *Direct imaging of a digital-micromirror device for configurable microscopic optical potentials.* Optica **3**(10), 1136 (2016).

[24] M. Kleman and O. D. Lavrentovich, eds. *The Order Parameter: Amplitude and Phase*, pp. 76–104 (Springer New York, New York, NY, 2003).

[25] N. W. Tschoegl. *8 - Thermodynamic Potentials.* In N. W. Tschoegl, ed., *Fundamentals of Equilibrium and Steady-State Thermodynamics*, pp. 49–61 (Elsevier Science, Amsterdam, 2000).

[26] M. Abid, C. Huepe, S. Metens, C. Nore, C. Pham, L. Tuckerman, and M. Brachet. *Gross–Pitaevskii dynamics of Bose–Einstein condensates and superfluid turbulence.* Fluid dynamics research **33**(5), 509 (2003).

[27] P.-H. Chavanis. *Dissipative self-gravitating Bose-Einstein condensates with arbitrary nonlinearity as a model of dark matter halos* (2016). `1611.09610`.

[28] J. Bak and D. J. Newman. *Simply Connected Domains*, pp. 107–116 (Springer New York, New York, NY, 2010).

[29] R. N. Valani, A. J. Groszek, and T. P. Simula. *Einstein–Bose condensation of Onsager vortices.* New Journal of Physics **20**(5), 053038 (2018).

[30] R. J. Creswick and H. L. Morrison. *On the dynamics of quantum vortices.* Physics Letters A **76**(3), 267 (1980).

[31] H. Takeuchi, N. Suzuki, K. Kasamatsu, H. Saito, and M. Tsubota. *Quantum Kelvin-Helmholtz instability in phase-separated two-component Bose-Einstein condensates.* Physical Review B **81**(9) (2010).

[32] M. Roberts. *Fluid Instabilities and Transition to Turbulence* (2020).

[33] C. Foullon, E. Verwichte, V. M. Nakariakov, K. Nykyri, and C. J. Farrugia. *Magnetic Kelvin-Helmholtz Instability at the Sun.* The Astrophysical Journal **729**(1), L8 (2011).

[34] R. Long. *Some Aspects of the Flow of Stratified Fluids.* Tellus **7**, 341 (2010).

[35] R. Krasny. *Vortex sheet computations: roll-up, wakes, separation.* Lectures in Applied Mathematics **28**(1), 385 (1991).

[36] P. Tabeling. *Two-dimensional turbulence: a physicist approach.* Physics Reports **362**(1), 1 (2002).

[37] A. M. Steane, M. Chowdhury, and C. J. Foot. *Radiation force in the magneto-optical trap.* Journal of the Optical Society of America. B, Optical physics **9**(12), 2142 (1992).

[38] K. Davis, M. Mewes, M. Joffe, M. Andrews, and W. Ketterle. *Evaporative cooling of sodium atoms.* Physical review letters **74**(26), 5202 (1995).

[39] D. Xiong, P. Wang, H. Chen, and J. Zhang. *Evaporative cooling rubidium atoms with microwave radiation.* Chin. Opt. Lett. **8**(4), 351 (2010).

[40] S. J. M. Kuppens, K. L. Corwin, K. W. Miller, T. E. Chupp, and C. E. Wieman. *Loading an optical dipole trap.* Phys. Rev. A **62**, 013406 (2000).

[41] J. Brand and W. P. Reinhardt. *Generating ring currents, solitons and vortices by stirring a Bose-Einstein condensate in a toroidal trap.* Journal of Physics B: Atomic, Molecular and Optical Physics **34**(4), L113–L119 (2001).

[42] A. Kumar, R. Dubessy, T. Badr, C. De Rossi, M. d. G. de Herve, L. Longchambon, and H. Perrin. *Producing superfluid circulation states using phase imprinting.* Physical Review A **97**(4), 043615 (2018).

[43] W. Ketterle, D. S. Durfee, and D. M. Stamper-Kurn. *Making, probing and understanding bose-einstein condensates* (1999).

[44] S. Forstner, Y. Sachkou, M. Woolley, G. I. Harris, X. He, W. P. Bowen, and C. G. Baker. *Modelling of vorticity, sound and their interaction in two-dimensional superfluids.* New Journal of Physics **21**(5), 053029 (2019).

[45] C. G. Baker. *Superfluid optomechanics* (2020).

[46] G. Bonaccorso. *Mastering Machine Learning Algorithms* (Packt Publishing, 2018), 1 ed.

[47] P. Mehta, M. Bukov, C.-H. Wang, A. G. Day, C. Richardson, C. K. Fisher, and D. J. Schwab. *A high-bias, low-variance introduction to Machine Learning for physicists.* Physics Reports **810**, 1 (2019).

[48] D. Jones, M. Schonlau, and W. Welch. *Efficient global optimization of expensive black-box functions.* Journal of Global Optimization **13**, 455 (1998).

[49] G. Carleo, I. Cirac, K. Cranmer, L. Daudet, M. Schuld, N. Tishby, L. Vogt-Maranto, and L. Zdeborová. *Machine learning and the physical sciences.* Rev. Mod. Phys. **91**, 045002 (2019).

[50] P. B. Wigley. *Generating and observing soliton dynamics in Bose-Einstein Condensates.* Ph.D. thesis, Department of Quantum Science, Research School of Physics and Engineering, The Australian National University (2017).

[51] P. B. Wigley, P. J. Everitt, A. van den Hengel, J. W. Bastian, M. A. Sooriyabandara, G. D. McDonald, K. S. Hardman, C. D. Quinlivan, P. Manju, C. C. N. Kuhn, and et al. *Fast machine-learning online optimization of ultra-cold-atom experiments.* Scientific Reports **6**(1) (2016).

[52] I. Nakamura, A. Kanemura, T. Nakaso, R. Yamamoto, and T. Fukuhara. *Non-standard trajectories found by machine learning for evaporative cooling of ^{87}Rb atoms.* Opt. Express **27**(15), 20435 (2019).

[53] D. A. Reynolds. *Gaussian Mixture Models.* Encyclopedia of biometrics **741**, 659 (2009).

[54] Y. Li and H. Wu. *A Clustering Method Based on K-Means Algorithm.* Physics Procedia **25**, 1104 (2012).